

**A New Spectral Framework for Crystal Plasticity Modeling of Cubic and Hexagonal
Polycrystalline Metals**

A Thesis

Submitted to the Faculty

of

Drexel University

by

Marko Knezevic

in partial fulfillment of the

requirements for the degree

of

Doctor of Philosophy

April 2009

© Copyright 2009

Marko Knezevic. All Rights Reserved.

Dedications

I dedicate my research work to my parents Milorad and Slavica and my wife Ana. I thank them for their support, understanding, patience, and most of all love.

Acknowledgements

It is a pleasure to convey my sincere gratefulness to everyone who encouraged and supported me during my Ph.D. studies at Drexel University.

In the first place I would like to express my gratitude to my advisor, Dr. Surya R. Kalidindi for his guidance and support throughout my doctoral work. In addition to receiving high quality education, I enjoyed working with him. His high standards of professional excellence along with the passion and commitment for any work that he takes up will be a great source of inspiration in my future career.

I would like to thank my committee members: Dr. Roger D. Doherty, Dr. Antonios Zavaliangos, Dr. Alan C.W. Lau, and Dr. Franco Capaldi from Drexel University, and Dr. Raja K. Mishra from General Motors Research and Development Center for their time and suggestions on this work.

I am grateful to Dr. David T. Fullwood and Dr. Brent L. Adams from Brigham Young University for numerous discussions and collaborative work.

I would like to express my deepest appreciation to Dr. Leposava Sidjanin, my mentor from the University of Novi Sad, Serbia, for her support and encouragement to continue my education in the USA.

I am thankful to Mrs. Judith Trachtman, Mrs. Dorilona Rose and Ms. Keiko Nakazawa for their time and effort on all administrative matters.

Sincere thanks to my countrymen Dr. Dejan Stojakovic and Dr. Milan Ivosevic for significant help upon my arrival to the USA and overcoming the cultural shock.

I am thankful to my fellow research group members for their friendly support: Mr. Joshua Shaffer (for help in programming), Ms. Amanda Levinson (for help in performing some of the experiments), Mr. Christopher Hovanec (for teaching me some of the experimental techniques), Mr. Stephen Niezgoda, Mr. Tony Fast, Mr. Giacomo Landi, Mr. Hamad F. Al-Harbi, Ms. Shraddha Vachhani, Mr. David Turner, Mr. Siddhartha Pathak, Ms. Naomi Barth, Mr. Daniel Satko, and special thanks to Mr. Brendan Donohue (for teaching me the English language and American slang).

I would like to acknowledge students who graduated from our department during my studies for their help and advices on my academic and personal life: Dr. Hari Duvvuru, Dr. Massimiliano Binci, Dr. Xianping Wu, Dr. Gwenaelle Proust, Dr. Joshua Houskamp, and Dr. Brandon McWilliams.

Last, but not the least, I would like to express my deepest sense of gratitude to my family for their continuous support: my lovely wife Mrs. Ana Mihajlovic Knezevic, my mother Mrs. Slavica Knezevic, my father Mr. Milorad Knezevic, my dear sister Mrs. Vanja Knezevic and her little son Milos, and my cousin Mr. Zdravko Knezevic who constantly encouraged me to go for advanced studies.

For those countless people whom I have failed to mention here, many thanks.

Table of Contents

LIST OF TABLES	viii
LIST OF FIGURES	ix
ABSTRACT	xiv
1. INTRODUCTION	1
1.1. Crystal Plasticity	1
1.2. Materials Design	3
1.2.1. Property Closures.....	6
1.2.2. Process Design	8
1.3. Material Systems for Modeling	9
1.4. Plastic Deformation Mechanisms in Mg alloy.....	9
1.5. Objective	12
2. BACKGROUND	14
2.1. Crystallographic Texture	14
2.2. Orientation Imaging Microscopy	19
2.3. Crystal Plasticity Theories	22
2.4. Property Bounds.....	27
2.5. Spectral Representation of ODF Using GSH.....	28
2.6. First Order Homogenization Using GSH.....	31
3. IMPROVED SPECTRAL METHODS FOR CRYSTAL PLASTICITY	35
3.1. Discrete Representation of ODF and Homogenization Using DFTs.....	35
3.2. Spectral Crystal Plasticity of FCC metals.....	38
3.3. Spectral Crystal Plasticity of HCP metals	48
3.4. Selected Spectral Crystal Plasticity Case Studies	51
3.4.1. Plane Strain Compression in FCC Metals	52

3.4.2. Simple Shear in FCC Metals.....	54
3.4.3. Plane Strain Compression Followed by Simple Shear in FCC Metals.....	55
3.4.4. Equi-Channel Angular Extrusion in FCC Metals	56
3.4.5. Plane Strain Compression in HCP Metals	57
3.5. Delineation of Yield Surfaces Using DFTs	59
3.6. Property Closures and Microstructure Design.....	63
3.6.1. Atlases of Elastic-Plastic Property Closures.....	63
3.6.2. Performance Optimization Case Study: Compliant Mechanism	69
3.6.3. Closures of Plastic Properties Requiring Explicit Consideration of Strain Hardening and Crystallographic Texture Evolution	74
3.7. Texture Evolution Networks for Deformation Processing	82
3.7.1. Maximizing R_1	83
3.7.2. Maximizing R_1 and R_2	85
4. DEFORMATION TWINNING IN AZ31 Mg ALLOY	87
4.1. Mechanical Testing and Metallography.....	87
4.2. Results.....	90
4.3. Discussion	100
5. CONCLUSIONS AND FUTURE WORK	110
5.1. Conclusions.....	110
5.2. Suggestions for Future Work	114
LIST OF REFERENCES.....	116
APPENDIX A: DEFINITIONS OF SELECTED MACROSCALE MATERIAL PROPERTIES USED IN THIS WORK	126
APPENDIX B: PROCEDURE FOR DELINEATION OF CLOSURES FOR PROPERTIES THAT DO NOT REQUIRE CONSIDERATION OF STRAIN HARDENING AND CRYSTALLOGRAPHIC TEXTURE EVOLUTION.....	129

APPENDIX C: PROCEDURE FOR DELINEATION OF CLOSURES FOR PLASTIC PROPERTIES REQUIRING EXPLICIT CONSIDERATION OF STRAIN HARDENING AND CRYSTALLOGRAPHIC TEXTURE EVOLUTION.....	132
APPENDIX D: SPECTRAL CRYSTAL PLASTICITY CODE FOR FCC METALS .	134
APPENDIX E: ELASTIC PROPERTY CLOSURE CALCULATOR FOR FCC CRYSTALS WITH TRICLINIC SAMPLE SYMMETRY USING FFT METHODS ..	139
VITA.....	145

List of Tables

1. Summary of estimated hardening parameters for selected FCC metals	24
2. Summary of estimated hardening parameters for α -Ti	26
3. Comparison of predicted driving forces for various deformation mechanisms in a contraction twin-matrix composite based on the crystal plasticity finite element models and the highly simplified (uniform stress) Schmid model	108
4. Comparison of predicted driving force for the various deformation mechanisms in an extension twin-matrix composite based on the crystal plasticity finite element models and the highly simplified (uniform stress) Schmid model	109

List of Figures

1. Plastic deformation mechanisms in Mg.....	11
2. Bunge-Euler space containing (a) fundamental zone of cubic crystals (FZ), (b) three-times fundamental zone for cubic crystals (FZ3), and (c) fundamental zone for hexagonal crystals (FZ).....	18
3. Schematic representation of the components of an EBSD system in an SEM	20
4. Schematic of the sample inside the SEM chamber and an EBSD pattern	21
5. Some common ways of visualizing crystal orientations: a) an orientation imaging map of a polycrystalline sample b) a pole figure c) an inverse pole figure and d) a series of sections through Euler space	22
6. Texture hull for cubic-orthorhombic materials in the first three dimensions of the Fourier space.....	30
7. Magnitudes of dominant transforms (not including the zero transform) for (a) $\sigma'_{11}(g^p, \theta)$, (b) $W_{12}(g^p, \theta)$, and (c) $\sum_{\alpha} \dot{\gamma}(g^p, \theta)$. Note that the transforms were sorted by the magnitude before being plotted here.....	43
8. An example demonstrating the DFT interpolation scheme described in this thesis, and its validation by direct comparison with the corresponding predictions from the Taylor-type model used in this study.....	45
9. Average percentage error between the spectral predictions and direct computations for 100,000 randomly selected orientations subjected to randomly selected deformation modes as a function of the number of the dominant DFTs used in the spectral databases: (a) $\sigma'_{11}(g^p, \theta)$, (b) $W_{12}(g^p, \theta)$, and (c) $\sum_{\alpha} \dot{\gamma}(g^p, \theta)$	46
10. Contour plots of $\sigma'_{11}(g^p)_{\theta=\theta_0}$ in Bunge-Euler space. (a) Computed using 500 dominant DFTs. (b) Computed using the conventional crystal plasticity approach.....	47
11. Magnitudes of dominant transforms (not including the zero transform) for the variables included in the plots. Note that the transforms were sorted by the magnitude before being plotted here.....	51

12. Comparison of the predictions from the spectral method described here, using a minimal set of 134 dominant DFTs for stress, 255 dominant DFTs for lattice spin, and 182 dominant DFTs for shearing rate, against the corresponding predictions from the conventional Taylor-type model for plane strain compression of OFHC Copper: (a) pole figures, and (b) stress-strain curves53
13. Comparison of the predictions from the spectral method, using 500 dominant DFTs for stress components and the shearing rate and 3000 dominant DFTs for the lattice spin components, against the corresponding predictions from the conventional Taylor-type model for plane strain compression of OFHC Copper: (a) pole figures, and (b) stress-strain curves.....53
14. Comparison of the predictions from the spectral method, using 500 dominant DFTs for stress components and the shearing rate and 3000 dominant DFTs for the lattice spin components, against the corresponding predictions from the conventional Taylor-type model for simple shear of OFHC Copper: (a) pole figures, and (b) stress-strain curves55
15. Comparison of the predictions from the spectral method, using 500 dominant DFTs for the stress components and the shearing rate and 3000 dominant DFTs for the lattice spin components, against the corresponding predictions from the conventional Taylor-type model for a deformation mode involving a path change (plane strain compression up to strain of 0.5 followed by simple shear up to strain of 1.0) of OFHC Copper: (a) pole figures, and (b) stress-strain curves. The stresses and strain plotted are axial components during plane strain compression and shear components during simple shear.....56
16. Comparison of the predicted (111) pole figures using the DFT based crystal plasticity at different locations in the billet after one pass with the corresponding measurements taken from [1]. (a) Top of the billet. (b) Middle of the billet. (c) Bottom of the billet. Contours from experiments and model: 1/1.4/2/2.8/4/5.6/8/11 ..57
17. Comparison of the predictions from the spectral method described here, using a set of 1000 dominant DFTs for each of the field variables, against the corresponding predictions from the conventional Taylor-type model for plane strain compression of α -Ti: (a) pole figures, and (b) stress-strain curves59
18. a) pole figures for the random texture, b) and c) selected projections of the yield surfaces for the random texture, d) pole figures for the (111) fiber texture, e) and f) selected projections of the yield surfaces for the fiber texture. The different shape of the yield surfaces for the two different textures should be noted62
19. Atlas of $C^*_{1111}-C^*_{1313}$ closures for a broad selection of cubic materials.....64
20. $C^*_{1111}-C^*_{1313}$ closures for alpha Ti, beta Ti-Nb, and mixture of alpha and beta Ti phases.....65

21. C^*_{1111} - C^*_{1122} , and C^*_{1111} - C^*_{1112} closures for copper polycrystals.....	66
22. Atlas of $(C^*_{1111}, \sigma_{y1}/s)$ closures for a range of FCC metals	67
23. $(C^*_{1111}, \sigma_{y1}/s)$ closure for all FCC metals.	68
24. a) $(C^*_{1111}, \sigma_{y1}/s)$ upper bound closure for copper polycrystals with no sample symmetry. b) Comparison between upper bound orthorhombic (black) and upper bound triclinic (gray) closures of polycrystalline copper	69
25. The relevant property closure for a cantilever compliant beam made of high-purity polycrystalline α -Ti with hexagonal-orthorhombic textures. The texture predicted to provide the best and the worst performances for this case study are also shown.....	73
26. First-order closures for the ultimate tensile strength (σ_{UTS}) and the yield strength (σ_{y1}) in OFHC Cu and 5754-O Al based on Taylor-type models and a consideration of all theoretically possible textures (i.e. the elements of the texture hull). The textures that are theoretically predicted to correspond to salient points of interest on the boundary are depicted. Textures A, C, and E are for OFHC Copper, while textures B, D, and F are for 5754-O Al.....	75
27. Influence of the subtle differences in the textures on the ultimate tensile strength (σ_{UTS}) and the yield strength (σ_{y1}) exhibited by the metal. The properties corresponding to pairs of slightly different textures (A, B), (C, D), and (E, F) are shown on closures for 5754-O Al and OFHC Copper	77
28. Closure for the uniform ductility (e_u) and ultimate tensile strength (σ_{UTS}) in two cubic metals based on Taylor-type models, and a consideration of all theoretically possible textures (i.e. the elements of the texture hull). The textures that are theoretically predicted to correspond to salient points of interest on the boundary are depicted	79
29. Closure for the R_f -ratio and the yield strength (σ_{y1}) in 5754-O Al based on Taylor-type model for all theoretically possible textures. The desired texture is I. The evolution of textures and properties in typical deformation processes are also shown for three initial textures. These processes do not transform the properties in the desired direction.....	81

30. (a) Projection of the texture evolution network onto the $(R_l, \sigma_{y,l})$ property closure. (b) Identification of a processing recipe to produce high values of R_l . (c) Texture obtained at the end of 18 processing operation. (d) Processing recipe identified by a brute-force constant performance maximization scheme. (e) The final texture obtained at the end of 171 processing steps.....	83
31. Processing recipes identified using the texture evolution network for enhancing both R_l and R_2 obtained at the end of 7 and 9 processing steps, respectively.....	86
32. (a) Measured pole figures showing the initial texture in the annealed AZ31 sheet. (b) Schematic showing the orientations of the cylinders used in simple compression tests performed in this study. (c) EBSD inverse pole figure (IPF) map showing orientation of the annealed sheet's ND direction with respect to the local crystal frames, collected in the sheet RD-TD plane. The crystallographic c -axis in most grains is closely aligned with the sample ND direction.....	88
33. Simple compression tests at room temperature on an annealed sheet of AZ31: (a) true stress-true strain responses, (b) normalized strain hardening responses. The various points labeled indicate locations where microstructure investigations were conducted using OIM.....	91
34. Inverse pole figure (IPF) maps showing microstructure evolution of the TD-RD compressed AZ31 samples to true strain levels of (A) 0.01, (B) 0.025, (C) 0.04, (D) 0.05, (E) 0.06, and (F) 0.08. These maps indicate the orientation of the compression axis with respect to the crystal reference frame. The marker shown in these maps corresponds to a length of 100 microns. The color-legend is the same as in Fig. 32(c)	92
35. Pole figures showing texture evolution in the TD-RD compressed AZ31 samples to true strains of: (A) 0.01, (B) 0.025, (C) 0.04, (D) 0.05, (E) 0.06, and (F) 0.08. The compression axis lies at the center of all the pole figures shown here	93
36. Extension twin boundaries identified in the OIM maps based on the expected mis-orientation in the TD-RD compressed sample interrupted at point (C) at a true strain of -0.04	94
37. Volume fraction of material with crystallographic c -axis oriented within 20 degrees of the compression direction in the TD-RD samples. The compressed samples are labeled A to F with corresponding strain level indicated in the brackets	96
38. Inverse pole figure (IPF) maps showing microstructure evolution of the ND compressed AZ31 samples to true strain levels of (I) 0.012 and (II) 0.065. These maps indicate the orientation of the compression axis with respect to the crystal reference frame. The color-legend is the same as in Fig. 32(c). Image quality map at II shows high concentration of twin like bands; we believe that these bands represent the contraction twin bands.....	97

39. Mechanical response of annealed AZ31 tested in simple compression and simple tension at room temperature and a constant strain rate of 10^{-3} s^{-1} along TD direction: a) true stress-true strain responses, b) normalized strain hardening responses, c) expanded view of the yield response shown in (a)99
40. A comparisons of the normalized true stress-true strain responses and normalized strain hardening rates during simple compression of α -Ti and AZ31 with similar initial textures.....101
41. Finite element meshes used in simulating the stress fields in the matrix-twin composite: matrix-extension twin on the left and matrix-contraction twin on the right. The crystallographic **c**-axis in the matrix was selected to be coincident with the loading direction 3 in the FEM models. The elements used for computing average stresses in the twinned region and in the matrix region are highlighted in the mesh shown on the left.....106

Abstract

A New Spectral Framework for Crystal Plasticity Modeling of Cubic and Hexagonal Polycrystalline Metals

Marko Knezevic

Surya R. Kalidindi, PhD

Crystal plasticity physics-based constitutive theories are used in understanding and predicting the evolution of the underlying microstructure and the concomitant anisotropic stress-strain response in polycrystalline metals subjected to finite plastic strains. A new scheme for efficient crystal plasticity computations for both cubic and hexagonal polycrystalline metals subjected to arbitrary deformation modes has been developed in this thesis. This new computational scheme involves building material databases comprised of spectral coefficients. These spectral coefficients are computed using discrete Fourier transforms (DFTs) and allow for compact representation and fast retrieval of crystal plasticity solutions for a crystal of any orientation subjected to any deformation mode. The novel approach is able to speed up the conventional crystal plasticity computations by two orders of magnitude. Furthermore, mathematical procedures for delineation of property closures that identify the complete set of theoretically feasible combinations of macroscale effective properties has been developed for a broad set of mechanical properties. Subsequently, these constructs were used in microstructure design for identifying an optimal microstructure for selected performance criteria. And finally, hybrid processing recipes that transform a given initial microstructure into a member of the set of optimal microstructures that exhibit superior properties or performance characteristics have been described. Insights and tremendous

potential of these novel materials knowledge systems are discussed and demonstrated through specific case-studies.

The anisotropic stress-strain response measured in simple compression and simple tension tests in different sample directions on an annealed, strongly textured, AZ31 sheet has been studied. New insights into the mechanical response of this material were obtained by correlating the changes in the measured strain-hardening rates in the different experiments to the corresponding changes in the microstructure evolution are provided. Based on the experimental observations, a hypothesis is postulated for explaining the different morphologies of the extension and contraction twins, and the apparent tension/compression asymmetry exhibited by this alloy. The main elements of the hypothesis are then critically evaluated using finite element simulations of stress fields in various matrix-twin configurations subjected to a range of loading conditions.

CHAPTER 1: INTRODUCTION

Materials science and engineering is an interdisciplinary field connecting structure, processing, and properties of matter and using them in various applications of science and engineering. The development of new materials has defined the evolutionary stages in the progression of our society (from the Stone Age to the Bronze Age to metallurgy from where modern materials science has evolved). There is constant demand for high performance specialty materials. Often, multiple property objectives are required along with rigorous treatment of material anisotropy. In recent years, the discipline of materials science has witnessed the emergence of a new paradigm where suitable processing routes are identified to produce microstructures with desired target properties. It is expected that in this new era, extensive computer simulations of various physical phenomena in materials science over a vast range of time and length scales will aid development of new materials by reducing the number of trials in traditional trial-and-error experimentation. The present thesis is a contribution in this direction.

1.1. Crystal Plasticity

One of the most widely used processes in manufacture of various metallic components is plastic deformation. The properties of a product depend significantly on the changes in the underlying microstructure details (e.g. distribution of grain orientations) in the material during deformation. These changes of the microstructure (e.g. rotation of grains towards preferred orientations) can be controlled. In order to optimize the properties of the final manufactured product, robust and reliable predictive simulation tools are highly desirable. Crystal plasticity theories are used extensively [2-

11] in understanding and predicting the evolution of the underlying microstructure (mainly texture related aspects) and the concomitant anisotropic stress-strain response in polycrystalline metals subjected to finite plastic strains. Such physics-based constitutive theories are critical for conducting more accurate simulations of various metal manufacturing/fabrication processes, since they provide better understanding and predictions of the material behavior [12-14]. The main deterrent in the more widespread use of these theories (in place of the highly simplified phenomenological isotropic plasticity theories typically used) is the fact that the implementation of the crystal plasticity theories in a finite element modeling framework demands substantial computational resources and highly specialized expertise.

A number of strategies are being explored currently to speed up the crystal plasticity calculations. The most promising of these strategies appear to be those that seek efficient spectral representations combined with a database approach that stores the main characteristics of the crystal plasticity solutions. Li *et al.* [15] and Kalidindi and Duvvuru [16] have demonstrated the viability of the Bunge-Esling approach [17,18] using generalized spherical harmonics (GSH) for texture evolution. In this approach, the important details of texture evolution were captured in a database of streamlines for a selected deformation process. A process plane concept, based on proper orthogonal decomposition in Rodrigues-Frank space [19] has been presented by Sundararaghavan and Zabaras [20], again for selected deformation modes. Both the streamline approach and the process plane approach have not yet been successfully generalized for arbitrary deformation modes. Moreover, these models are based on conservation principles in the

orientation space that do not presently resolve the differences in the strain hardening responses of differently oriented crystals.

In this work, a new scheme for efficient crystal plasticity computations for arbitrary deformation modes is developed. This new computational scheme involves building material databases comprised of spectral coefficients. These spectral coefficients are computed using discrete Fourier transforms (DFTs) and allow for compact representation and fast retrieval of crystal plasticity solutions for a crystal of any orientation subjected to any deformation mode. The novel approach is able to speed up the conventional crystal plasticity computations of cubic and hexagonal polycrystals by two orders of magnitude. It is anticipated that the computational speed gained provides significant incentive for incorporating the novel approach into finite element simulation tools of bulk deformation processing and studying microstructure evolution during complex deformation processes. The details of this new approach are described in this thesis and validated through several case studies.

1.2. Materials Design

The concept of materials design has been an emerging research topic in materials science and engineering. The drive to design materials is driven by several factors: better materials with improved performance, better components in advanced technology, and a shortened development cycle from concept to implementation. The predominant design methodology in current engineering practice is largely focused on the optimization of relevant geometric parameters using robust numerical simulations tools. Material selection is often restricted to search of a relatively small database [e.g. 21], with no real

concept of microstructure as a design variable. These databases are generally compiled from experimentally measured values in available materials. It should be recognized that only a very small subset of all feasible microstructures in a given material system have been produced and characterized to date. Furthermore, for ease of analysis, material properties are often assumed to be isotropic. However, the majority of commercially available structural metals exhibit anisotropic mechanical properties as a natural consequence of anisotropy at the single crystal level, combined with complex changes in microstructure as a consequence of the thermo-mechanical loading histories experienced during their manufacturing process. Thus, the initial challenge that must be tackled is identification of the complete space of feasible anisotropic properties and related polycrystalline microstructures. The subsequent goal is to link processing routes with resulting material structure. Hence, a systematic approach to materials design is required which incorporates the full anisotropy of the underlying constituents, and provides not only a method for identifying microstructures that will provide optimal performance, but also a guide to the designer as to how to arrive at such structures.

In this context, a number of alternative approaches have been proposed for materials-by-design in recent years. The systems approach, pioneered by Olson [22,23], embodies the integration of processing-structure-property relations using a set of multi-scale, hierarchical models (spanning thermodynamics, molecular dynamics, micromechanics, solidification). The system approach has not yet incorporated the anisotropy of the properties of interest in its considerations, and does not address whether the solutions obtained correspond to local or global optima. Some of the remarkable successes of this approach have included the development of high-strength, high-

toughness, steels for advanced applications in gears and bearings [24-27]. Another approach, called Topology Optimization, arrives at new microstructures through clever spatial distribution of material phases, and aims to optimize a prescribed objective function formulated in terms of desired macroscale properties. This methodology has been successful in designing microstructures that are theoretically predicted to exhibit certain extremal macroscale properties [28-35], including materials with negative thermal expansion coefficients. Topology optimization has thus far been largely restricted to multi-phase material systems with either isotropic constituents and anisotropic macroscale properties, or anisotropic constituents and isotropic macroscale properties. This methodology has not yet addressed rigorously the design of processing recipes to produce the optimal microstructures identified to possess the extremal properties. Furthermore, the methodology does not fully address the issue of local vs global optimal solutions.

In recent years, Adams, Kalidindi, and Garmestani have successfully formulated microstructure-property-processing linkages in a spectral framework called Microstructure Sensitive Design (MSD) [36-39] using a statistical description of the microstructure. Salient features of MSD include: (i) construction of a *Microstructure Hull* that includes the complete set of theoretically feasible statistical distributions that quantitatively describe the relevant details of the microstructure (at different levels of detail, classified as ' n -point' statistics [40]), and (ii) delineation of *Property Closures* that identify the complete set of theoretically feasible combinations of macroscale effective properties of interest in a given application, for a selected homogenization theory. The primary advantages of the MSD approach lie in its (a) consideration of *anisotropy* of the

properties at the local length scales, (b) exploration of the *complete* set of relevant microstructures (captured in the microstructure hull and property closures) leading to global optima, and (c) *invertibility* of the microstructure-property-processing relationships (due to the use of spectral methods in representing these linkages). Successful implementation of the framework facilitates a rigorous consideration of microstructure as a continuous design variable in the design and optimization of multifunctional engineering components.

The spectral microstructure-property-processing linkages of MSD were represented using generalized spherical harmonics (GSH). Although the GSH representation can be customized to automatically reflect the various symmetries associated with the selection of the crystal and sample reference frames, the main difficulty with their usage lies in the fact that they are computationally expensive. In this thesis, it will be demonstrated that the use of Discrete Fourier Transforms (DFTs) in place of the GSH representation leads to tremendous computational efficiency. Furthermore, the MSD framework will be extended using rigorous mathematical procedures for delineating property closures for broader set of mechanical properties and texture evolution networks for deformation processing. Next two sections describe these two goals in more details.

1.2.1. Property Closures

Property closures delineate the complete set of theoretically feasible macroscale (homogenized) anisotropic property combinations in a given material system, and are of tremendous interest in optimizing the performance of engineering components.

Historically, this problem has been referred to as the G-closure problem by the applied mathematics community [41-44]. To date, G-closures have been obtained only for a limited set of two-dimensional microstructures comprised of isotropic phases and have been largely focused on properties such as effective conductivity and elastic stiffness. In recent years, MSD [36,37,45,46] was demonstrated to provide approximations to the G-closures for a number of combinations of the elastic properties and yield properties of polycrystalline materials [47-49] and two-phase composites [50,51].

All of the previous reports in literature on delineation of property closures of polycrystalline metals have focused on a class of properties that treat the microstructure as being static. Moreover, orthorhombic sample symmetry was always imposed on all textures considered in arriving at the property closures. In the present work, closures were obtained without any restrictions of the sample symmetry. Furthermore, in consideration of a broader class of plastic properties of metals, we immediately encounter two important features: (i) strain hardening, and (ii) concurrent evolution of microstructure due to plastic strain. Prime examples of such properties include the uniform ductility and the ultimate tensile strength. Because of their influence on the toughness exhibited by the material, these properties play an important role in materials selection for critical structural components. Since these properties directly influence the formability (and thereby the success of certain deformation processing operations), they are also of tremendous interest for deformation processing of metals. In order to successfully delineate a broader class of plastic property closures, the previous framework [47-49] needed to be extended to allow for the evolution of the associated local state variables. An important goal of this work is to use spectral representation of

microstructure-property-processing relationships to produce for the first time a new class of property closures that address plastic properties at finite strains (requiring explicit consideration of strain hardening and texture evolution).

1.2.2. Process Design

Historically, much of the development of novel processing routes for materials with desired combinations of properties has resulted from clever intuition, combined with empiricism and a healthy dose of serendipity. Examples of rigorous design of a processing recipe to meet a set of designer-specified properties are rare in the literature. The availability of a large number of manufacturing options to control and modify the internal material structure (i.e. microstructure) raises the exciting possibility of combining known manufacturing options in arbitrary sequences (i.e. hybrid processing) to develop new materials with as yet unrealized (but desired) combinations of macroscale properties. However, because of the very large number of available manufacturing options and the enormous space of potential microstructures, successful design of hybrid processing routes critically needs a computationally efficient approach.

In this thesis, the texture evolution networks for deformation processing is projected into the property closure and used to identify processing paths to textures with optimal performances. The processing options selected for this work include deformation processing at low homologous temperatures under all possible deformation modes, while allowing for arbitrary sample rotations.

1.3. Material Systems for Modeling

The primary focus in this thesis is on the crystal lattice orientation as the primary descriptor of the local state in polycrystalline metallic systems. OFHC copper and Al-5754-O are examples of high stacking fault energy, face-centered cubic (fcc) metals that will be used in developing and evaluating the analytical framework. These metals were selected because the Taylor-type crystal plasticity models have been extensively validated on them. The interest in properties and process modeling of materials with hexagonal structure has increased dramatically in the last decade with the emergence of titanium alloys as candidates for high specific-strength and high temperature applications in aerospace and transportation systems. Ti will be used in some case studies involving materials with hexagonal structure. Hence, both cubic and hexagonal polycrystalline metallic systems are considered for the development of this analytical framework.

1.4. Plastic Deformation Mechanisms in Mg alloy

Magnesium alloys are being increasingly evaluated for applications in the automotive components due to their outstanding properties such as low density, high specific strength, castability, machinability at high speeds, and weldability under controlled atmospheres. The automobile industry is already utilizing cast magnesium alloys [52]. Although wrought magnesium alloys are expected to possess better mechanical properties, the main hurdle has been the limited room temperature formability exhibited by these alloys. Enhancing the formability of Mg alloys requires a better understanding of the prevailing mechanisms of deformation in these alloys to large plastic strains.

Pure magnesium has a hexagonal close-packed (HCP) structure with a c/a ratio of 1.624 [53], which is close to the ideal ratio of 1.633. Consequently, basal $\langle a \rangle$ slip systems are the easy glide systems in Mg [54]. Although prism $\langle a \rangle$ and pyramidal $\langle a \rangle$ slip systems also operate in Mg, they require higher driving forces [55-57]. All of the slip systems mentioned above provide only a total of four independent slip systems. In particular, none of these are capable of accommodating any plastic strain along the c direction. The activation of 2nd pyramidal $\langle c+a \rangle$ slip systems is generally assumed to provide the needed additional degree of freedom, and has been confirmed experimentally [55,58-63]. Alternatively, deformation twinning can also provide the needed additional degree of freedom for isochoric plastic deformation. Two common twin modes have been observed in magnesium. These are classified as $\{10\bar{1}2\}\{10\bar{1}\bar{1}\}$ extension twins and $\{10\bar{1}1\}\{10\bar{1}\bar{2}\}$ contraction twins [53], because they result in the extension and the contraction of the crystal along the c direction, respectively. The extension twins are thick and are readily observed [64,65], while the contraction twins are very thin and harder to detect [66]. The physical origin of the different morphologies of the extension and the contraction twins are not yet fully understood. Interestingly, the extension twins are also found within the contraction twin lamella, leading to a “double-twinning” phenomena [62-64,66-72]. Since deformation twinning in Mg is often easier than pyramidal $\langle c+a \rangle$ slip, it represents a dominant mechanism of plastic deformation in various magnesium alloys. The geometries of the plastic deformation mechanisms in Mg are illustrated in the Fig. 1.

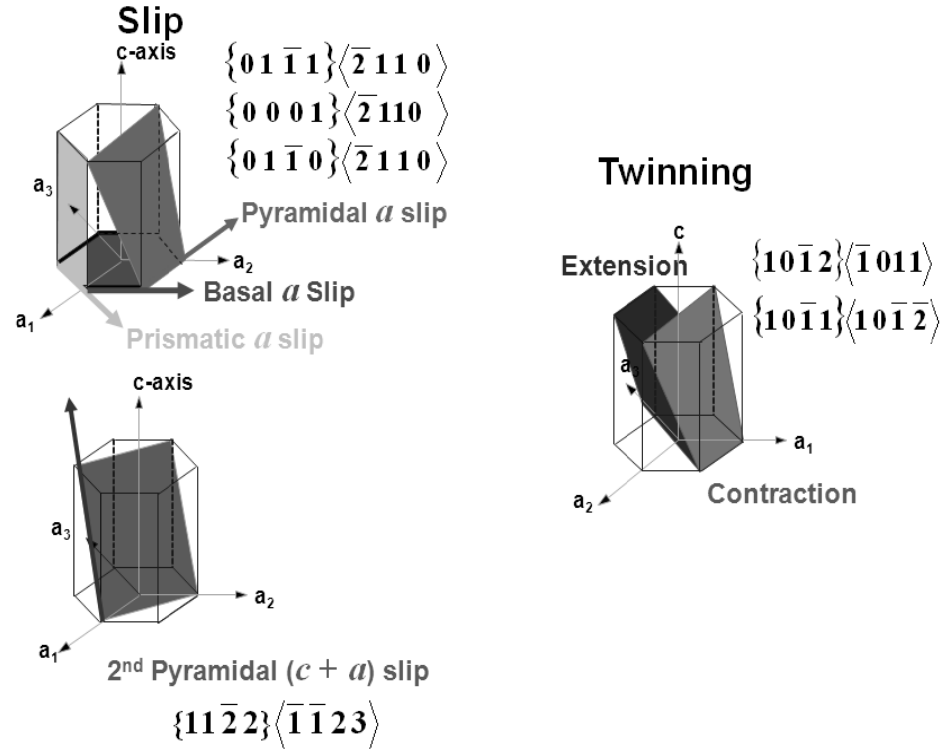


Figure 1 Plastic deformation mechanisms in Mg.

The influence of deformation twinning on the anisotropic strain hardening response as well as the evolution of the underlying microstructures in a broad range of fcc metals [73,74] and in α -Ti [75-77] has been studied. In these studies, measured changes in strain hardening responses were correlated to distinct changes in the mechanisms of plastic deformation, while simultaneously providing new insights into the observed changes in the underlying microstructure. In this thesis, a similar study is conducted on AZ31.

The anisotropic stress-strain response measured in simple compression and simple tension tests in different sample directions on an annealed, strongly textured, AZ31 sheet is studied. The concomitant evolution of microstructure using electron back-scattered diffraction (EBSD) based orientation image mapping (OIM) is also documented. New

insights into the mechanical response of this material by correlating the changes in the measured strain-hardening rates in the different experiments to the corresponding changes in the microstructure evolution are provided. Based on the experimental observations, a hypothesis is postulated for explaining the different morphologies of the extension and contraction twins, and the apparent tension/compression asymmetry exhibited by this alloy. The main elements of the hypothesis are then critically evaluated using finite element simulations of stress fields in various matrix-twin configurations subjected to a range of loading conditions.

1.5. Objective

In summary, the objective of this thesis is to develop suitable materials knowledge databases for studying effects of complex deformation processes on texture and the effects of texture on a broad set of mechanical properties. An advantage of these knowledge systems (spectral databases) is that they allow extremely fast explorations of these linkages. This feature is of paramount importance in materials modelling and design. The crystallographic texture is the only microstructural parameter that is considered. Specifically, the objectives are:

(i) Develop an efficient crystal plasticity framework using discrete Fourier transforms for both cubic and hexagonal metals that will capture texture evolution and the concomitant anisotropic stress-strain response during any general deformation process.

(ii) Develop rigorous mathematical procedures for identifying a complete set of theoretically feasible anisotropic property combinations for a broad set of mechanical

properties. Here, the focus is on building material knowledge databases of property closures of elastic properties and plastic properties involving combinations of yield strength, ultimate tensile strength, uniform ductility, and the Lankford parameter R . A number of examples of property closures will be presented and discussed. Subsequent goal is to use these developments into microstructure design and identify an optimal microstructure for selected performance criteria. And finally, we aim to identify hybrid processing recipes to transform a given initial microstructure into a member of the set of optimal microstructures that exhibit superior properties or performance characteristics. Insights and tremendous potential of this new approach will be discussed and demonstrated through specific case-studies.

(iii) Establish the fundamental mechanisms of plastic deformation in AZ31 Mg alloy and obtain the information and understanding needed for the development of reliable crystal plasticity models for Mg alloys. Insights into the mechanical response of this material will be obtained by correlating the changes in the measured strain-hardening rates in the different experiments to the corresponding changes in the microstructure evolution. A hypothesis for explaining the different morphologies of the extension and contraction twins, and the apparent tension/compression asymmetry exhibited by this alloy will be postulated and validated.

Chapter 2 will provide the necessary background, and clearly identifies the work done by previous graduate students from our research group on which the present work is built upon. Chapter 3 covers modeling part of the research work done in this thesis. Chapter 4 covers experimental part of the research work done in this thesis. Chapter 5 will present conclusions and suggestions for future work.

CHAPTER 2: BACKGROUND

2.1. Crystallographic Texture

A crystal is characterized by repeating lattice patterns extending in all three spatial dimensions. The constituent crystal in a polycrystalline metal is referred to as grain. The orientation of the grain can be defined relative to a coordinate frame. This frame is usually the sample coordinate frame in which properties are to be specified. A distribution of all orientations with respect to the sample frame in a polycrystalline aggregate is referred to as crystallographic texture. Crystallographic texture is widely recognized as an important detail of the microstructure in polycrystalline materials that is known to have a strong influence on their macroscale anisotropic elastic-plastic properties [11,17,36,46,47,78-80]. The anisotropy of material properties is associated with a non-random distribution of the crystal orientations. Any non-random distribution of these crystal orientations is a consequence of the complex thermo-mechanical loading history experienced in their manufacture. There are a lot of examples of materials engineered to possess specific textures, for example [13,81,82].

Any crystal orientation, g , may be described using any one of the established representations [19,83,84], including Euler angles, angle-axis pairs, Rodriguez vectors, quaternions, or orthogonal matrices. A common feature of these different, but equivalent, representations is that all of them require specification of three independent parameters to describe a given crystal orientation. Consequently, the orientation space of interest can always be reduced to a three-dimensional space.

In the present thesis, orientation is described using a set of three Bunge-Euler angles [84], i.e. $g = (\varphi_1, \Phi, \varphi_2)$. The main advantage of the Bunge-Euler space is that all

functions of interest (ODF, structure-property relationships) can be defined in such a way that they are inherently periodic. This is mainly because this space is defined by rotation angles that make their appearance in structure-property relationships of interest only in the form of integer powers of sines and cosines of the rotation angles. This important attribute of the Bunge-Euler space has been central to the successful development and application of spectral representations in this space. A transformation matrix that transforms a crystal frame to the sample frame using Bunge-Euler angles is constructed as:

$$\mathbf{g} = \begin{pmatrix} \cos\varphi_1 \cos\varphi_2 - \sin\varphi_1 \sin\varphi_2 \cos\Phi & -\cos\varphi_1 \sin\varphi_2 - \sin\varphi_1 \cos\varphi_2 \cos\Phi & \sin\varphi_1 \sin\Phi \\ \sin\varphi_1 \cos\varphi_2 + \cos\varphi_1 \sin\varphi_2 \cos\Phi & -\sin\varphi_1 \sin\varphi_2 + \cos\varphi_1 \cos\varphi_2 \cos\Phi & -\cos\varphi_1 \sin\Phi \\ \sin\varphi_2 \sin\Phi & \cos\varphi_2 \sin\Phi & \cos\Phi \end{pmatrix}. \quad (2.1)$$

The Bunge-Euler space should ideally be defined as $(\phi_1 \in (0, 2\pi], \Phi \in (0, 2\pi], \phi_2 \in (0, 2\pi])$, as all functions of interest are naturally periodic in this space in each of the three dimensions. However, because of crystal symmetry there are several redundancies within this space that can be exploited in the computations. For crystals of any symmetry, the definitions of the Bunge-Euler angles require that locations (ϕ_1, Φ, ϕ_2) and $(\phi_1 + \pi, 2\pi - \Phi, \phi_2 + \pi)$ correspond to the exact same crystal lattice orientation. The space after this reduction is depicted in the Fig. 2. Furthermore, consideration of eight of the lattice symmetry operations associated with a cubic crystal lattice (e.g. FCC, BCC) require that the locations corresponding to $(\phi_1 + \pi, \pi - \Phi, 2\pi - \phi_2)$, $(\phi_1 + \pi, \pi - \Phi, \pi - \phi_2)$, $(\phi_1 + \pi, \pi - \Phi, \pi/2 - \phi_2)$, $(\phi_1 + \pi, \pi - \Phi, 3\pi/2 - \phi_2)$, $(\phi_1, \Phi, \phi_2 + \pi/2)$, $(\phi_1, \Phi, \phi_2 + \pi)$, and $(\phi_1, \Phi, \phi_2 + 3\pi/2)$

also correspond to the exact same crystal lattice orientation defined by (ϕ_1, Φ, ϕ_2) . These equivalencies indicate that the natural periodic unit cell for all functions defined for cubic crystals in the Bunge-Euler space can be defined as $(\phi_1 \in [0, 2\pi), \Phi \in [0, 2\pi), \phi_2 \in [0, \pi/2))$.

As a result of all of the considerations of symmetry for cubic crystals described above, it can be easily seen that we can focus our attention on the space defined by

$$FZ3 = \left\{ (\phi_1, \Phi, \phi_2) \left| \phi_1 \in [0, 2\pi), \Phi \in \left[0, \frac{\pi}{2}\right), \phi_2 \in \left[0, \frac{\pi}{2}\right) \right. \right\}. \quad (2.2)$$

The shaded area in the Fig. 2 (b) represents the $FZ3$. It is important to note here that if the values of any desired function are obtained on a uniform grid in $FZ3$, then it is fairly simple to assign values on a uniform grid over the periodic unit cell $(\phi_1 \in [0, 2\pi), \Phi \in [0, 2\pi), \phi_2 \in [0, \pi/2))$ using the relationships mentioned earlier. The space defined here as $FZ3$ is actually three times the FZ defined in conventional texture analyses for cubic-triclinic (i.e. cubic symmetry in crystal reference frame and triclinic symmetry in the sample reference frame) functions. Note that only eight of the symmetry operators are used in defining $FZ3$. The FZ can be constructed if additional 3-fold symmetry operations belonging to the $\langle 111 \rangle$ axes are applied:

$$FZ = \left\{ (\phi_1, \Phi, \phi_2) \left| 0 \leq \phi_1 < 2\pi, \cos^{-1} \left(\frac{\cos \phi_2}{\sqrt{1 + \cos^2 \phi_2}} \right) \leq \Phi \leq \frac{\pi}{2}, 0 \leq \phi_2 \leq \frac{\pi}{4} \right. \right\}. \quad (2.3)$$

FZ represents the complete set of physically distinct orientations that can occur in the sample, and is depicted in the Fig. 2 (a). The main reason for the preferred use of $FZ3$ instead of FZ is that a uniform grid in FZ does not map to uniform grids in the remainder of $FZ3$. At this point, it may be appropriate to reflect importance of the uniform grid. As it will be apparent shortly, in this thesis, discrete Fourier transforms (DFTs) can be used for the representation of texture and properties in place of the GSH (generalized spherical harmonics) being used currently. A feature of DFTs is that they provide the maximum computational efficiency if a function is on a uniform grid. In summary, the values of all desired functions established on a uniform grid in the $FZ3$ space, can easily be expanded to the periodic unit cell ($\phi_1 \in [0, 2\pi)$, $\Phi \in [0, 2\pi)$, $\phi_2 \in [0, \pi/2)$) using the relationships mentioned earlier, and then used to compute DFTs. Similarly, symmetry operations associated with hexagonal crystal lattice (hcp) can reduce the Bunge-Euler space to FZ by recognizing following twelve equivalent orientations: (ϕ_1, Φ, ϕ_2) , $(\phi_1, \Phi, \phi_2 + \pi/3)$, $(\phi_1, \Phi, \phi_2 + 2\pi/3)$, $(\phi_1, \Phi, \phi_2 + \pi)$, $(\phi_1, \Phi, \phi_2 + 4\pi/3)$, $(\phi_1, \Phi, \phi_2 + 5\pi/3)$, $(\phi_1 + \pi, \pi - \Phi, \pi/3 - \phi_2)$, $(\phi_1 + \pi, \pi - \Phi, 2\pi/3 - \phi_2)$, $(\phi_1 + \pi, \pi - \Phi, \pi - \phi_2)$, $(\phi_1 + \pi, \pi - \Phi, 4\pi/3 - \phi_2)$, $(\phi_1 + \pi, \pi - \Phi, 5\pi/3 - \phi_2)$, $(\phi_1 + \pi, \pi - \Phi, 2\pi - \phi_2)$. The periodic unit cell for all functions defined for hexagonal crystals in the Bunge-Euler space can be defined as ($\phi_1 \in [0, 2\pi)$, $\Phi \in [0, 2\pi)$, $\phi_2 \in [0, \pi/3)$). Fortunately, all transactions and reflections associated with hexagonal crystal symmetry preserve the regular grid required by DFTs. The hexagonal FZ is shown as shaded area in the Fig. 2 (c) and is defined as:

$$FZ = \left\{ (\phi_1, \Phi, \phi_2) \mid 0 \leq \phi_1 \leq \frac{\pi}{2}, 0 \leq \Phi \leq \frac{\pi}{2}, 0 \leq \phi_2 \leq \frac{\pi}{3} \right\}. \quad (2.4)$$

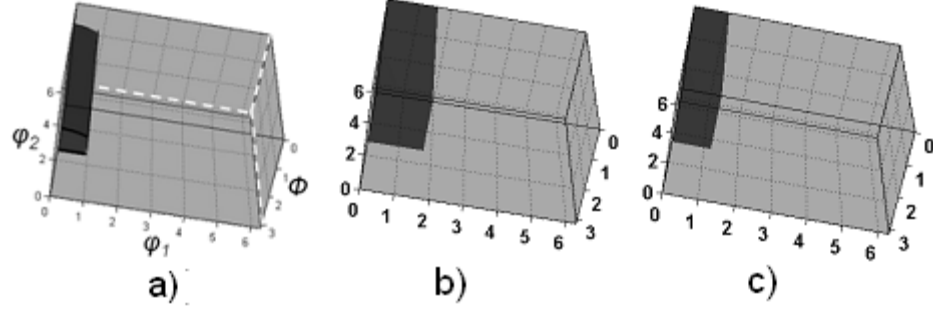


Figure 2 Bunge-Euler space containing (a) fundamental zone of cubic crystals (FZ), (b) three-times fundamental zone for cubic crystals (FZ3), and (c) fundamental zone for hexagonal crystals (FZ).

Furthermore, in some of the case studies cubic-orthorhombic textures will be used. The orthorhombic description here refers to the symmetry resulting from processing history (many of the typical processing operations used on metals such as rolling produce this symmetry).

The crystallographic texture or the Orientation Distribution Function (ODF) is denoted as $f(g)$, and reflects the normalized probability density associated with the occurrence of the crystallographic orientation g in the sample. ODF is formally defined as

$$\frac{dV_g}{V} = f(g)dg, \quad \int_{FZ} f(g)dg = 1.0, \quad (2.5)$$

where V denotes the total sample volume and dV_g is the sum of all sub-volume elements in the sample that are associated with a lattice orientation that lies within an incremental invariant measure, dg , of the orientation of interest, g . This statistical representation of

the material allows the derivation of relations between the microstructure of a material and the bounds on the properties, as will be shown in the following chapters.

2.2. Orientation Imaging Microscopy

Among several methods, such as X-ray or neutron diffraction, the orientation is best revealed using electron backscatter diffraction (EBSD) in the scanning electron microscope (SEM). This section outlines Orientation Imaging Microscopy (OIM) as an experimental technique that enables an investigator to efficiently obtain a great deal of information about the orientation of crystals in a polycrystalline specimen. The OIM entails collection and automatic determination (i.e. indexing) of the orientation of the diffracting lattice from the EBSD patterns (also called Kikuchi diffraction patterns). OIM has transformed the labor intensive process of manually indexing EBSD patterns to an efficient systematic tool that facilitates rapid and automatic indexing. The options offered by the OIM tool offer tremendous help in understanding the relationships between processing, microstructure and properties in terms of better understanding of texture evolution and its influence on properties.

The OIM systems are integrated with a SEM to utilize its electron gun, vacuum system, optical column, etc, as shown in Fig. 3. A stationary beam is focused on a tilted sample mounted in a sample holder. The sample is tilted to approximately 70° ensuring sufficient number of diffracted electrons to escape towards the detector. A part of the EBSD system in the chamber of an SEM is a phosphor screen whose purpose is to capture the pattern and transmit it to the CCD camera. In order to improve the diffraction pattern detection, the processing/camera control unit performs operations such as

background subtraction, image averaging and smoothing and compression. The final additional unit in this setup is a computer equipped with the OIM software that is devoted to EBSD pattern analysis. This is where all aspects of analyses are conducted including indexing, data storage, and data representation/manipulation.

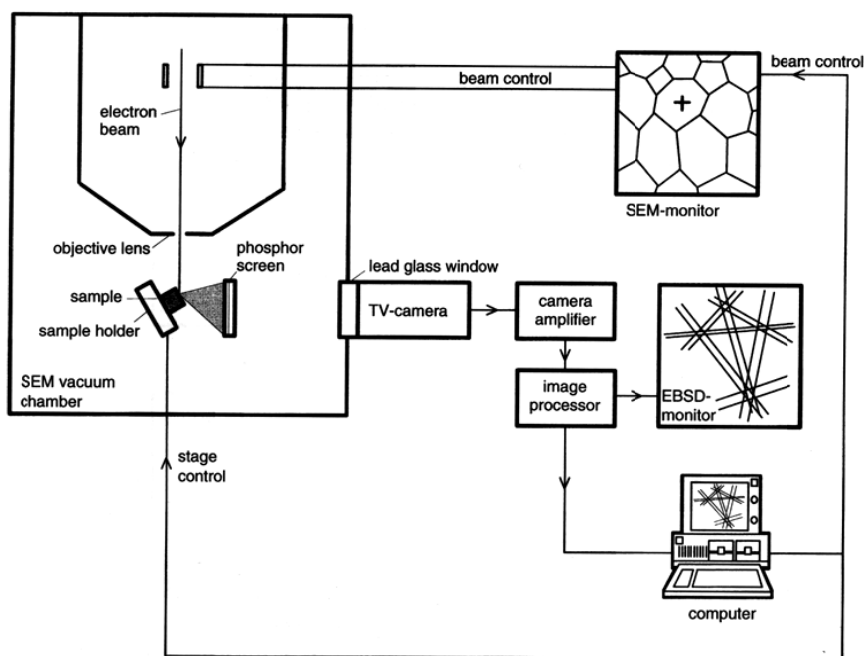


Figure 3 Schematic representation of the components of an EBSD system in an SEM [83].

Automated EBSD pattern indexing made OIM a widely used tool. Indexing involves detection and identification of sufficient number of the bands and the poles (zone axis) in a EBSD pattern and the determination of the crystal orientation. The EBSD patterns are obtained by focusing the electron beam on a crystalline sample (see Figure 4). The electrons disperse beneath the surface, subsequently diffracting among the crystallographic planes. The diffracted electrons produces a pattern composed of intersecting bands, termed electron backscatter diffraction (EBSD) patterns (see Figure 4). The patterns are imaged by placing a phosphor screen close to the sample in the SEM

chamber. The bands in the pattern represent the reflecting planes in the diffracting crystal volume. Thus, the geometrical arrangement of the bands is a function of the orientation of the diffraction crystal lattice. The width and the intensity of the bands are directly related to the spacing of atoms in the crystallographic plane and the angles between the bands are directly related to the angles between the crystallographic planes. This technique allows crystal orientation information to be determined at very specific points in a sample. The spatial resolution varies with the accelerating voltage, beam current and spot size of the SEM along with the atomic number of the sample material.

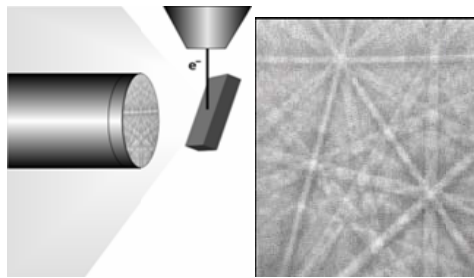


Figure 4 Schematic of the sample inside the SEM chamber and EBSD pattern.

There are several ways how the data can be represented. The most common ones are using orientation imaging maps, pole figures, inverse pole figures and sections through an orientation space. Grains in an OIM map are formed by an algorithm that groups points of similar orientation. The OIM software checks the misorientation of each point and its neighbors. Points that are within the specified tolerance are grouped together into a grain. Grain boundaries are created by rows of points that are not within the misorientation tolerance of each other. An example of an OIM map is shown in the Fig. 5 (a). A pole figure shows the normal to a specific plane as a pole projected onto a two

dimensional section. An example of (001) pole of an arbitrarily oriented cube is shown in the Fig. 5 (b). It is easily seen that the pole figures show the orientation of selected crystallographic planes with respect to the sample axis. An inverse pole figure shows the orientation of a given sample axis with respect to the crystal coordinate frame. A standard inverse pole figure triangle of an arbitrary orientation is shown in the Fig. 5 (c). Orientations can also be shown in an orientation space. Texture is most commonly represented as a series of sections through Euler space, as in the Fig. 5. (d).

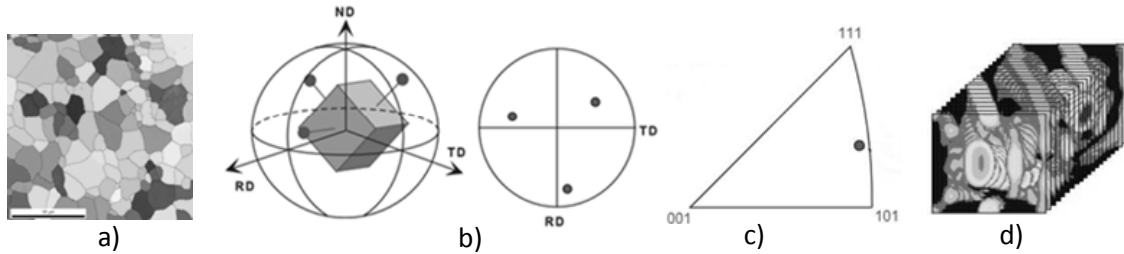


Figure 5 Some common ways of visualizing crystal orientations: a) an orientation imaging map of a polycrystalline sample b) a pole figure c) an inverse pole figure and d) a series of sections through Euler space.

2.3. Crystal Plasticity Theories

The rigid-viscoplastic crystal plasticity model [2] used in this work can be described by the following set of equations:

$$\mathbf{D} = \sum_{\alpha} \dot{\gamma}^{\alpha} \mathbf{P}^{\alpha}, \quad \mathbf{P}^{\alpha} = 0.5(\mathbf{m}^{\alpha} \otimes \mathbf{n}^{\alpha} + \mathbf{n}^{\alpha} \otimes \mathbf{m}^{\alpha}), \quad (2.6)$$

$$\dot{\gamma}^{\alpha} = \dot{\gamma}_0 \left| \frac{\tau^{\alpha}}{S^{\alpha}} \right|^{1/m} \text{sgn}(\tau^{\alpha}), \quad \tau^{\alpha} = \boldsymbol{\sigma}' \cdot \mathbf{P}^{\alpha}. \quad (2.7)$$

In Eqs. (2.6) and (2.7), \mathbf{D} is the applied isochoric stretching tensor, \mathbf{m}^α and \mathbf{n}^α are the unit vectors identifying the slip direction and the slip plane normal, respectively, for slip system α . For the fcc crystals studied in this thesis, the family of twelve $\{111\}\langle 1\bar{1}0\rangle$ slip systems were considered as potential slip systems. The deviatoric component of the Cauchy stress tensor in the crystal, denoted by $\boldsymbol{\sigma}'$, can be evaluated by solving Eqs. (2.6) and (2.7). τ^α , $\dot{\gamma}^\alpha$, and s^α represent the resolved shear stress, the shearing rate, and the slip resistance, respectively, on slip system α . The reference value of the shearing rate, $\dot{\gamma}_o$, is taken here as 0.001 sec^{-1} for quasi-static loading conditions. The strain rate sensitivity parameter denoted by m is taken to be 0.01, which is in agreement with measurements on most single phase fcc metals at low homologous temperatures. The lattice spin tensor \mathbf{W}^* (and the related lattice rotation tensor, \mathbf{R}^*) in the crystalline region is given by

$$\mathbf{W}^* = \dot{\mathbf{R}}^* \mathbf{R}^{*T} = \mathbf{W}^{app} - \mathbf{W}^p, \quad \mathbf{W}^p = \sum_{\alpha} 0.5 \dot{\gamma}^\alpha (\mathbf{m}^\alpha \otimes \mathbf{n}^\alpha - \mathbf{n}^\alpha \otimes \mathbf{m}^\alpha), \quad (2.8)$$

where \mathbf{W}^{app} is the applied spin tensor, and \mathbf{W}^p is the plastic spin tensor.

In this study, simplified saturation type hardening law has been adopted, which assumes that the slip resistances of all slip systems at any given location in a crystalline region exhibit the same slip resistance. They are, however, allowed to vary from one location to another depending on the local crystal orientation and the deformation history. This simplified slip hardening law is expressed as

$$\dot{s}^\alpha = h_o \left(1 - \frac{s^\alpha}{s_s} \right)^a \sum_\beta |\dot{\gamma}^\beta|, \quad (2.9)$$

where h_o , s_s and a denote the slip hardening parameters. The values of the slip hardening parameters were taken here to correspond to the values established previously [5] by calibrating the Taylor-type model to experimental measurements in OFHC copper (see Table 1). The slip hardening parameters for annealed Al 5754-O have been established here by calibrating the Taylor model predictions to experimental measurements using procedures described in the earlier paper [5] (see Table 1). Note that these hardening parameters are expected to be strongly influenced by composition (e.g. purity levels) and the grain size distribution in the metal.

Table 1 Summary of estimated hardening parameters for selected FCC metals.

	$s_o [MPa]$	$s_s [MPa]$	$h_o [MPa]$	a
OFHC	16	148	180	2.25
Al 5754-O	17	130	745	1.81

α -Ti is a metal with a hexagonal structure of interest in this work. The families of three basal $\{0001\} < \bar{2}110 >$, three prismatic $\{10\bar{1}0\} < \bar{2}110 >$, and twelve pyramidal $\{10\bar{1}1\} < 11\bar{2}\bar{3} >$ slip systems were considered. In addition to slip, six compressive $\{10\bar{1}2\} < \bar{1}011 >$ and six tensile $\{11\bar{2}2\} < 11\bar{2}\bar{3} >$ twin systems could be operative. When deformation twinning is to be included in addition to slip, the crystal plasticity models get substantially more complicated because of the creation of a very large number of new grains as a consequence of the deformation twinning. Amongst a number of

different approaches, a grain fragmentation model provided the best results when compared against experimental evidence [85]. In this model, twinning was considered as a pseudo-slip mechanism until the twin volume fraction in the grain reached a pre-determined saturation value (determined from experiments to be 0.4 for α -Ti). At that point, the grain was fragmented into a matrix grain and several offspring grains corresponding to each of the dominant twin systems. The newly formed grains were allowed to independently undergo further slip and concomitant lattice rotation, but further twinning was prohibited.

For the hexagonal α -Ti polycrystals deforming by slip and twinning, the hardening laws had to be modified significantly from that given in Eq. (2.9):

$$\dot{s}^\alpha = h_s^{pri} \left(1 - \frac{s^\alpha}{s_s^\alpha}\right) \sum_{k=1}^{N_s^{pri}} \dot{\gamma}^k + h_s^{bas} \left(1 - \frac{s^\alpha}{s_s^\alpha}\right) \sum_{l=1}^{N_s^{bas}} \dot{\gamma}^l + h_s^{pyr} \left(1 - \frac{s^\alpha}{s_s^\alpha}\right) \sum_{n=1}^{N_s^{pyr}} \dot{\gamma}^n, \quad (2.10)$$

$$h_s^{pri} = h_{so}^{pri} (1 + C(\sum_{\beta} f^{\beta})^b), h_s^{bas} = h_{so}^{bas} (1 + C(\sum_{\beta} f^{\beta})^b), h_s^{pyr} = h_{so}^{pyr} (1 + C(\sum_{\beta} f^{\beta})^b), \quad (2.11)$$

$$s_s^\alpha = \begin{cases} s_{so}^{pri} + s_{pr} (\sum_{\beta} f^{\beta})^{0.5} & \text{if } \alpha \in \text{prism slip systems} \\ s_{so}^{bas} + s_{pr} (\sum_{\beta} f^{\beta})^{0.5} & \text{if } \alpha \in \text{basal slip systems} \\ s_{so}^{pyr} + s_{pr} (\sum_{\beta} f^{\beta})^{0.5} & \text{if } \alpha \in \text{pyramidal slip systems.} \end{cases} \quad (2.12)$$

In Eqs. (2.10)-(2.12) h_s^{pri} , h_s^{bas} , h_s^{pyr} , s_{so}^{pri} , s_{so}^{bas} , s_{so}^{pyr} , C , s_{pr} and b denote the material hardening parameters. The values of this hardening parameters were taken here to correspond to the values established previously by calibrating the Taylor-type model to experimental measurements [85] (see Table 2).

Table 2 Summary of estimated hardening parameters for α -Ti.

S_o^{pri}	S_o^{bas}	S_o^{pyr}	S_{tw}	$h_{so}^{pri-bas}$	h_{so}^{pyr}
30MPa	150MPa	120MPa	125MPa	15MPa	300MPa
S_{so}^{pri}	$S_{so}^{bas-pyr}$	S_{pr}	C	b	
100MPa	300MPa	100MPa	25	2	

Note that in Eq. (2.10) it is assumed that all the different slip systems belonging to one family (e.g. pyramidal, basal or prismatic) in one crystal possess the same value of slip resistance. Note also that in this model, the twin resistance is maintained constant up to saturation of twin volume fraction. These decisions were made based on the experimental observations in titanium [77,85]. The physical interpretations of these parameters and their influence on specific aspects of the stress-strain curves were established in previous work. $\sum_{\beta} f^{\beta}$ denotes the total twin volume fraction in the grain. The numerical procedures for the integration of this constitutive model have been described in Refs. [5,85].

The most widely used approach to obtain the response of a polycrystal from the response of the individual grains is to use the extended Taylor's assumption of iso-deformation gradient in all of the crystals comprising the polycrystal. This model has enjoyed remarkable successes in predicting both the anisotropic stress-strain response and the evolution of the underlying texture in single-phase medium to high stacking fault energy cubic metals subjected to finite plastic strains in a broad range of deformation paths [3,4,6-9,11].

2.4. Property Bounds

As explained in the previous sections, in this thesis, the microstructures of the polycrystalline metals are described using distributions of the lattice orientation g , which is an important microstructural parameter influencing the elastic and plastic properties of polycrystalline materials. The ODF provides information regarding only the volume fractions of the various crystallographic orientations present in the material. Therefore, it is not possible to predict the exact properties associated with a given microstructure. However, these distributions can be used to obtain rigorous lower and upper bounds for the elastic and plastic yielding properties using first-order homogenization theories. This section defines the lower and upper bounds for all the components of the elastic stiffness, which allow a complete description of the elastic behavior of FCC and HCP polycrystalline metals, and the models used to compute the six plastic parameters required to describe the Hill's yield surface, which is generally used to define the plastic yielding properties of metals.

The elementary bounds on effective elastic stiffness parameters, C_{ijkl}^* , can be expressed as [47,86-88] (no summation implied on repeated indices in the following set of equations)

$$(\bar{S}^{-1})_{ijij} \leq C_{ijij}^* \leq \bar{C}_{ijij}, \quad (2.13)$$

$$\max(\bar{C}_{ijij}, (\bar{S}^{-1})_{ijij}) - \sqrt{A_i A_j} \leq C_{ijij}^* \leq \min(\bar{C}_{ijij}, (\bar{S}^{-1})_{ijij}) + \sqrt{A_i A_j}, \quad \text{when } i \neq j, \quad (2.14)$$

$$\text{with } A_i = \bar{C}_{iiii} - (\bar{S}^{-1})_{iiii}. \quad (2.15)$$

In Eqs. (2.13) - (2.15), the bars on top of a field quantity denote its volume averaged value, and \mathbf{C} and \mathbf{S} are the local fourth-rank elastic stiffness and elastic compliance tensors, respectively.

The effective plastic yield properties are bounded rigorously on the upper side by the Taylor-type model [5,11], and approximately on the lower side by the Sachs model [89]. Taylor model has been described in the previous section. The Sachs's model assumes that the same stress state is applied in all constituent grains in a polycrystal [90,91]. In this model, it is assumed that a grain undergoes plastic deformation as soon as the resolved shear stress applied on one of its slip systems reaches the critical resolved shear stress (CRSS); only grains that are oriented along symmetry lines would have more than one active system.

2.5. Spectral Representation of ODF Using GSH

Fourier or spectral analysis is one of the most valuable techniques in mathematical analysis in general. It essentially represents an arbitrary function as a combination of weighted harmonic functions. The weights are referred as Fourier coefficients while harmonic functions belong to a class of special functions. Fourier or spectral analysis is a very useful data processing technique used in various engineering and science fields to dramatically compress the amount of data involved. Typical examples include compression of a bitmap image by 95% or more by using the 'spectral' jpeg format [92]. Another example involves the commonly used MP3 format for audio compression [93]. The spectral approach is fundamental to the ability to efficiently store,

analyze and manipulate microstructure databases (for example when developing property or process relations, or inverting such relations during material design).

The representation of the ODF as a continuous function offers tremendous advantages in many aspects of texture analyses (e.g. visualization, comparisons) as well as in the use of homogenization theories for the estimation of the overall macroscopic properties of the polycrystalline sample. Although there currently exist many different approaches to represent the ODF as a continuous function, spectral representations using the generalized spherical harmonics (GSH) in the Bunge-Euler space have been found to be particularly convenient in many applications [47,49,94,95].

The ODF can be expressed efficiently in a Fourier series using generalized spherical harmonic (GSH) functions [84,94] as

$$f(g) = \sum_{l=0}^{\infty} \sum_{\mu=1}^{M(l)} \sum_{\nu=1}^{N(l)} F_l^{\mu\nu} \dot{T}_l^{\mu\nu}(g), \quad (2.16)$$

where $\dot{T}_l^{\mu\nu}(g)$ denote the symmetrized GSH functions and $F_l^{\mu\nu}$ coefficients represent uniquely the ODF. The suitably symmetrized sets of GSH functions used for cubic, cubic-orthorhombic, hexagonal, and hexagonal-orthorhombic crystals are denoted as $\dot{T}_l^{\mu\nu}(g)$, $\dot{T}_l^{\mu\nu}(g)$, $\dot{T}_l^{\mu\nu}(g)$, and $\dot{T}_l^{\mu\nu}(g)$, respectively [84]. Eq. (2.16) allows the visualization of ODF as a single point in an infinite dimensional Fourier space (coordinates given by $F_l^{\mu\nu}$). The set of all such points, corresponding to the complete set of all physically realizable ODFs, is called the texture hull in the MSD framework

[36,96]. The hull for cubic-orthorhombic textures is depicted in the first three dimensional Fourier subspace in Fig. 6. It should be recognized that any physically realizable texture has to have a representation inside the depicted hull. Note also that the texture hulls are compact and convex in any of their subspaces [97].

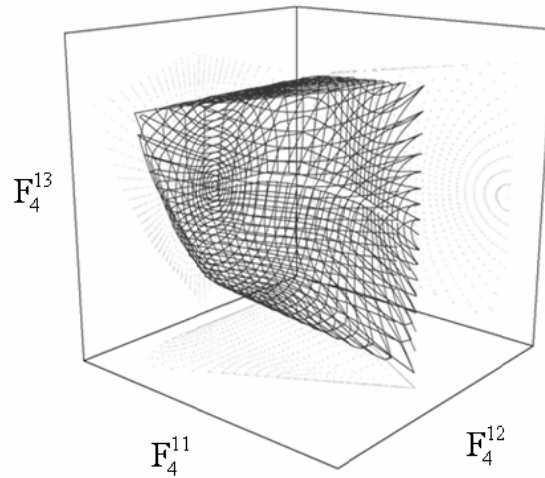


Figure 6 Texture hull for cubic-orthorhombic materials in the first three dimensions of the Fourier space.

The GSH offers a highly efficient Fourier basis that has been shown to result in the most compact representations for describing the crystal orientation dependence of several tensorial variables of interest (e.g. elastic stiffness components for the cubic-orthorhombic textures include only four non-zero coefficients). The efficiency observed in GSH representations is, in part, attributable to the fact that the GSH basis can be customized to automatically reflect the various symmetries associated with the selection of the crystal and sample reference frames. GSH representations in the Bunge-Euler space have been successfully applied to numerous problems in texture analyses and the estimation of macroscale properties in polycrystalline solids [36,47,94,95].

The main difficulty with using GSH is the fact that they are computationally expensive. They are defined as

$$T_l^{mn}(g) = T_l^{mn}(\phi_1, \Phi, \phi_2) = e^{im\phi_1} \cdot P_l^{mn}(\cos \Phi) \cdot e^{in\phi_2} \quad (2.17)$$

where $P_l^{mn}(\cos \Phi)$ is

$$\begin{aligned} P_\ell^{mn}(x) &= \frac{(-1)^{\ell-m} i^{n-m}}{2^\ell (\ell-m)!} \left[\frac{(\ell-m)! (\ell+n)!}{(\ell+m)! (\ell-n)!} \right]^{1/2} \\ &\times (1-x)^{-\frac{n-m}{2}} (1+x)^{-\frac{n+m}{2}} \frac{d^{\ell-n}}{dx^{\ell-n}} \left[(1-x)^{\ell-m} (1+x)^{\ell+m} \right] \end{aligned} \quad (2.18)$$

a certain generalizations of the associated Legendre function that are themselves computed using a classical Fourier series expansion [94]. In this thesis, it will be demonstrate that the use of Discrete Fourier Transforms (DFTs) in the representation of the ODF leads to tremendous computational efficiency.

2.6. First Order Homogenization Using GSH

The ODF described above constitutes a first-order description of the microstructure (also referred to as 1-point statistics). Using this microstructure description, only the bounds of the effective elastic and plastic properties can be evaluated. Higher order descriptions, called n-point spatial correlation function, are also possible [80,98,99].

The volume averages needed in the computation of the bounds described above can be evaluated as follows. For a macroscopic tensorial property of interest, P , its dependence on the local crystal orientation is denoted by $P(g)$ and expressed in Fourier series as [94]

$$P(g) = \sum_{l=0}^{\tilde{l}} \sum_{\mu=1}^{M(l)} \sum_{\nu=1}^{N(l)} P_l^{\mu\nu} \dot{T}_l^{\mu\nu}(g), \quad (2.19)$$

where $P_l^{\mu\nu}$ are referred to as the property coefficients, and it is explicitly noted that this Fourier representation extends to only a finite number of terms [47,94]. For example, if we consider cubic orthorhombic textures and elastic properties there exist only four non-zero terms. This is an important advantage of the GSH representation. The values of the property coefficients relevant to the elastic-plastic properties of interest in both FCC and HCP metals with cubic-orthorhombic textures have been presented in a prior study [47]. Using the orthonormality of the Fourier bases, the volume averaged value is then computed as

$$\bar{P} = \oint P(g) f(g) dg = \sum_{l=0}^{\tilde{l}} \sum_{\mu=1}^{M(l)} \sum_{\nu=1}^{N(l)} \frac{1}{(2l+1)} P_l^{\mu\nu} F_l^{\mu\nu}. \quad (2.20)$$

The concepts described above facilitated delineation of the first-order property closures. Following is an example of the mathematical formulation for identifying the (C_{1111}^*, C_{1313}^*) closure done in prior studies. Let \tilde{C}_{1313}^* denote a specific value of C_{1313}^* that

lies in between its theoretical maximum and minimum values (identified by a consideration of all feasible single crystal orientations). The complete set of Fourier coefficients, \tilde{M} , that can be associated with the selected value of \tilde{C}_{1313}^* can be expressed as

$$\tilde{M} = \left\{ F_l^{\mu\nu} \middle| F_l^{\mu\nu} \in \text{Hull}, \tilde{C}_{1313}^* = \alpha \bar{C}_{1313} + (1-\alpha) \bar{S}_{1313}^{-1}, \alpha \in [0,1] \right\}, \quad (2.21)$$

where Hull denotes the set of all Fourier coefficients that lie on or inside the texture hull representing the complete set of physically realizable textures (see Fig. 6). Note that the values of $F_l^{\mu\nu}$ influence the values of \bar{C}_{1313} and \bar{S}_{1313} (see Eq. (2.20)). The maximum and minimum values of C_{1111}^* are then established as

$$\left(\tilde{C}_{1111}^* \right)_{\max} = \text{Max} \left\{ \bar{C}_{1111} \middle| F_l^{\mu\nu} \in \tilde{M} \right\} \quad (2.22)$$

$$\left(\tilde{C}_{1111}^* \right)_{\min} = \text{Min} \left\{ \left(\bar{S}^{-1} \right)_{1111} \middle| F_l^{\mu\nu} \in \tilde{M} \right\} \quad (2.23)$$

It should be noted above that $\left(\bar{S}^{-1} \right)_{1111}$ in Eq. (2.23) denotes the (I, I, I, I) component of the inverse of the averaged fourth-rank compliance tensor. $\left(\left(\tilde{C}_{1111}^* \right)_{\max}, \tilde{C}_{1313}^* \right)$ and $\left(\left(\tilde{C}_{1111}^* \right)_{\min}, \tilde{C}_{1313}^* \right)$ constitute two of the points on the first-order closure we seek. By letting \tilde{C}_{1313}^* vary systematically between its theoretical maximum and minimum values, we can delineate the complete first-order property closure. It should be clear from the above description that the mathematical procedures used in the prior work in delineating the first-order

closures are quite complex and require substantial computational effort and resources. This procedure has thus far only been applied on a set of properties that do not require consideration of the strain hardening and texture evolution. Additionally, orthorhombic sample symmetry was always imposed in arriving at the property closures.

CHAPTER 3: IMPROVED SPECTRAL METHODS FOR CRYSTAL PLASTICITY

This chapter describes work done in this Ph.D. thesis by building on the background described in the previous chapter.

3.1. Discrete Representation of ODF and Homogenization Using DFTs

Traditionally the ODF has been represented in terms of generalized spherical harmonics, which are theoretically the most compact Fourier representations for various homogenization relations described in the last chapter. However, they are computationally expensive. An alternative to the use of GSH representations in various aspects of texture analyses is developed in this thesis and presented below. These new representations utilize discrete Fourier transforms (DFT).

A major advantage of using Fourier transforms in place of GSH representations is that we can compute the transforms using the much more computationally efficient algorithms (such as Fast Fourier Transforms or FFTs). The cheap availability of computer memory in recent times makes the fact that the representations using Fourier transforms are not likely to be as compact as the GSH representations not a significant drawback.

DFTs, or FFTs because of the algorithms used in their computation, are typically computed using the function values on a uniform grid [100-104]. Let the three-dimensional Bunge-Euler space of interest be discretized uniformly into $B_1 \times B_2 \times B_3$ bins, and let (b_1, b_2, b_3) enumerate these bins. The DFT representation of the ODF is defined as

$$f_{b_1 b_2 b_3} = \frac{1}{B_1 B_2 B_3} \sum_{k_1=0}^{B_1-1} \sum_{k_2=0}^{B_2-1} \sum_{k_3=0}^{B_3-1} F_{k_1 k_2 k_3} e^{\frac{2\pi i k_1 b_1}{B_1}} e^{\frac{2\pi i k_2 b_2}{B_2}} e^{\frac{2\pi i k_3 b_3}{B_3}} \quad (3.1)$$

where $f_{b_1 b_2 b_3}$ denotes the value of the ODF in the bin identified by (b_1, b_2, b_3) . In the remainder, for simplicity of notation, equations such as Eq. (3.1) will be expressed in a condensed notation as

$$f_b = \frac{1}{B} \sum_{k=0}^{B-1} F_k e^{\frac{2\pi i k b}{B}}. \quad (3.2)$$

F_k denotes the DFT for the ODF. For given values of the ODF on a uniform grid in the Bunge-Euler space, its DFT can be computed as

$$F_k = \sum_{b=0}^{B-1} f_b e^{\frac{-2\pi i k b}{B}}. \quad (3.3)$$

In previous section [47,49], it has been demonstrated that spectral approaches (based on GSH basis) can be used effectively to build volume average macroscale properties. Here, we show that the same can be computed much more efficiently using the DFT representations.

A common feature of all the first-order homogenization theories is that they require computation of the volume averaged values of selected property variables in the polycrystalline sample. Let $P(g(x))$ denote one such variable that depends on the local

crystal orientation at location \mathbf{x} in the sample. Invoking statistical homogeneity (i.e. volume averages are equal to ensemble averages), we can write

$$\overline{P} = \frac{1}{V} \int_V P(\mathbf{x}) d\mathbf{x} = \int_{3FZ} f(g) P(g) \sin \Phi d\phi_1 d\Phi d\phi_2 \quad (3.4)$$

where the bar on top of a variable indicates an volume-averaged value. With the intent of computing the integral in Eq. (3.4) efficiently by exploiting the orthogonal properties of the spectral representations, we need to combine $\sin \Phi$ with either $f(g)$ or $P(g)$. For given values of the ODF and the properties on a uniform grid in the Bunge-Euler space, its DFT can be computed as

$$F_k = \sum_{b=0}^{B-1} f_b e^{\frac{-2\pi i k b}{B}}, \quad \tilde{P}_k = \sum_{b=0}^{B-1} P_b \sin \Phi_b e^{\frac{-2\pi i k b}{B}}. \quad (3.5)$$

Using the orthogonal properties of DFTs, it is easy to show that

$$\overline{P} = \frac{1}{B} \sum_{k=0}^{B-1} F_k \tilde{P}_k \quad (3.6)$$

It is also worth noting that the computations in Eq. (3.6) can be simplified a little by recognizing that about half of the DFT terms of real functions are complex conjugates of the other half (i.e. $F_k = F_{B-k}^*$, and $\tilde{P}_k = \tilde{P}_{B-k}^*$).

The number of non-zero DFT terms varied for the different stiffness components, and were in the range of 9 to 61. It should be noted that the maximum number of Fourier coefficients needed for the same variables in GSH representations is 9. It is therefore clear from this comparison that the GSH representations are indeed more efficient in capturing the function with a smaller number of terms in the Fourier expansions. However, the DFT computations are significantly faster by at least two orders of magnitude. Another major advantage of the DFT representations is their easy access (FFT algorithms are much more readily available in many software packages compared to the availability of the GSH functions).

The DFT based texture representation and homogenization will be used here in building material knowledge databases of property closures of elastic-plastic properties. Numerous examples of these property closures will be presented later.

3.2. Spectral Crystal Plasticity of FCC metals

The crystal plasticity computations typically demand significant computational resources because of the low value of m (which makes the resulting system of algebraic equations numerically extremely stiff). Moreover, the same computations are likely to be repeated several times in simulations performed by the conventional approach, because the results of computations in any one time step are immediately forgotten when the computations advance to the next time step.

In the spectral crystal plasticity approach [105,106], our goal is to establish efficient spectral representations for the essential functions capturing the solutions to the crystal plasticity theory described above. In other words, our interest here is in

establishing the functions $\sigma'_{ij}(g, \mathbf{L})$, $W_{ij}^*(g, \mathbf{L})$, and $\sum_{\alpha} |\dot{\gamma}^{\alpha}|(g, \mathbf{L})$, where g is the crystal lattice orientation and \mathbf{L} is the applied velocity gradient tensor. In any given time step in the simulation of the deformation process, these functions can then be used to compute all of the needed microscale and macroscale field quantities that would be typically computed by the traditional crystal plasticity approach.

It is important to recognize that the spectral representations described above are independent of the specific homogenization theory used in bridging the microscale response of the crystalline regions within individual grains to the macroscale polycrystal response. In the simple Taylor-type models, the applied velocity gradient tensor at the microscale is assumed to be the same as the one applied at the macroscale (on the polycrystal). The macroscopic stress for the polycrystal is then obtained by volume averaging the stresses inside the polycrystal. In using the spectral databases described here with more sophisticated homogenization theories, it will be necessary to first solve for the local (microscale) velocity gradient tensor to be applied and then use that as input to the functions described above.

Next, a strategy for compacting the domain of the functions established earlier is described. Following the approach described by Van Houtte [107], the applied traceless velocity gradient tensor (plastic deformations in metals are isochoric), \mathbf{L} , is additively decomposed into a spin component, \mathbf{W}^{app} , and a traceless stretching component, \mathbf{D} , which can be expressed using a single angular variable in its principal frame. This decomposition can be mathematically expressed as

$$\begin{aligned} \mathbf{L} &= \dot{\varepsilon} \mathbf{D}_0 + \mathbf{W}^{app}, \quad \mathbf{D}_0 = \sum_{j=1}^3 D_j \mathbf{e}_j^p \otimes \mathbf{e}_j^p, \quad \dot{\varepsilon} = |\mathbf{D}|, \\ D_1 &= \sqrt{\frac{2}{3}} \cos\left(\theta - \frac{\pi}{3}\right), \quad D_2 = \sqrt{\frac{2}{3}} \cos\left(\theta + \frac{\pi}{3}\right), \quad D_3 = -\sqrt{\frac{2}{3}} \cos(\theta), \end{aligned} \quad (3.7)$$

where $\{\mathbf{e}_i^p, i=1,2,3\}$ denotes the principal frame of \mathbf{D} , and the range of angular variable θ that defines all possible diagonal matrices is $[0, 2\pi)$. Consequently, the functions we seek can be expressed in terms of $(\theta, \dot{\varepsilon}, \{\mathbf{e}^p\}, \mathbf{W}^{app})$, instead of \mathbf{L} . As an example, the function for the deviatoric stress in the crystal can be expressed as $\sigma'_{ij}(g, \theta, \dot{\varepsilon}, \{\mathbf{e}^p\}, \mathbf{W}^{app})$. Recognizing that all crystal plasticity computations can be performed in the $\{\mathbf{e}^p\}$ reference frame and converted back to the sample reference frame when needed, we can transform $(g, \{\mathbf{e}^p\}) \Rightarrow g^p$, where g^p denotes the crystal orientation with respect to the $\{\mathbf{e}^p\}$ reference frame. Furthermore, the roles of variables $\dot{\varepsilon}$ and \mathbf{W}^{app} in the functions of interest here can be explicitly described. These simplifications allows us to focus our efforts in building the spectral databases on two primary variables, g^p and θ . In other words, we will be seeking spectral representations of $\boldsymbol{\sigma}'(g^p, \theta)$, $\mathbf{W}^*(g^p, \theta)$, and $\sum_{\alpha} |\dot{\gamma}^{\alpha}|(g^p, \theta)$. For the tensorial variables listed above (stresses and lattice rotations), these functions will describe the components in the principal frame of the stretching tensor, which can then be transformed appropriately to the sample or crystal reference frames, as needed. Spectral representations of these functions using DFTs can be expressed as

$$\mathbf{W}_{rq}^* = \dot{\varepsilon} \frac{1}{N_g N_\theta} \sum_k \sum_n \mathbf{B}_{kn} e^{\frac{2\pi i k r}{N_g}} e^{\frac{2\pi i n q}{N_\theta}} + \mathbf{W}^{app}, \quad (3.8)$$

$$\boldsymbol{\sigma}'_{rq} = s |\dot{\varepsilon}|^m \text{sgn}(\dot{\varepsilon}) \frac{1}{N_g N_\theta} \sum_k \sum_n \mathbf{C}_{kn} e^{\frac{2\pi i k r}{N_g}} e^{\frac{2\pi i n q}{N_\theta}}, \quad (3.9)$$

$$\left(\sum_\alpha |\dot{\gamma}^\alpha| \right)_{rq} = |\dot{\varepsilon}| \frac{1}{N_g N_\theta} \sum_k \sum_n G_{kn} e^{\frac{2\pi i k r}{N_g}} e^{\frac{2\pi i n q}{N_\theta}}. \quad (3.10)$$

In Eqs. (3.8)-(3.10), r and q enumerate the grid points while N_g and N_θ represent the total number of grid points in the orientation space (domain of g^p) and the θ space (describing the deformation mode), respectively. The sets of coefficients \mathbf{B}_{kn} , \mathbf{C}_{kn} , and G_{kn} are referred to as the DFTs, and are completely independent of the values of the variables g^p and θ at grid points r and q .

In order to compute these transforms, we first need to compute the values of the functions of interest on a uniform grid in the naturally periodic product space defined by the Bunge-Euler space and the deformation mode space. These values are computed using the crystal plasticity theory described earlier. In this work, this was accomplished using a regular three-degree grid in each of the angular variables involved. The Bunge-Euler space of interest in computing DFTs for orientation-dependent periodic functions in cubic crystals can be identified as $(\phi_1 \in [0, 2\pi), \Phi \in [0, 2\pi), \phi_2 \in [0, 2\pi))$ [84]. The periodic space of interest in defining the deformation mode is identified as $\theta \in [0, 2\pi)$. It is further emphasized that the space described above has been chosen as it provides the natural periodicity for all the functions of interest identified earlier. All the functions of interest

have very efficient spectral representation in this space, which will become apparent later. It should be noted that there exist quite a few redundancies in the space identified above. In other words, a selected combination of a lattice orientation and a deformation mode have multiple (but equivalent) function value in this space. These equivalent representations have been exploited in the computations of the function values.

For the functions studied in this work, it is typically observed that only a small fraction of the DFTs are numerically significant compared to the others. In other words, although the number of DFTs computed is as large as the discrete dataset of the function values that was used in computing the transform, only a relatively small fraction of the terms in the computed transform need to be stored; ignoring the rest of the terms in the transform does not have any noticeable influence on the reconstructed values. The numbers of numerically significant DFTs (henceforth referred to as dominant DFTs) varied for the different field variables. Figure 7 illustrates the variation of the magnitudes of the dominant DFTs (sorted by magnitude without including the zero transform which simply represents the average value of the function over the entire domain) for (a) $\sigma'_{11}(g^p, \theta)$, (b) $W_{12}(g^p, \theta)$, and (c) $\sum_{\alpha} \dot{\gamma}(g^p, \theta)$. A substantial compaction of the dataset is clearly possible for these functions. It can be seen that as few as 200 DFTs dominate the representations of the various functions of interest. In producing such a compact set, we have also taken advantage of the fact that about half of the DFTs are complex conjugates of the other half for all real-valued functions (e.g. $\mathbf{C}_{kn} = \mathbf{C}_{N_g - k, N_{\theta} - n}^*$).

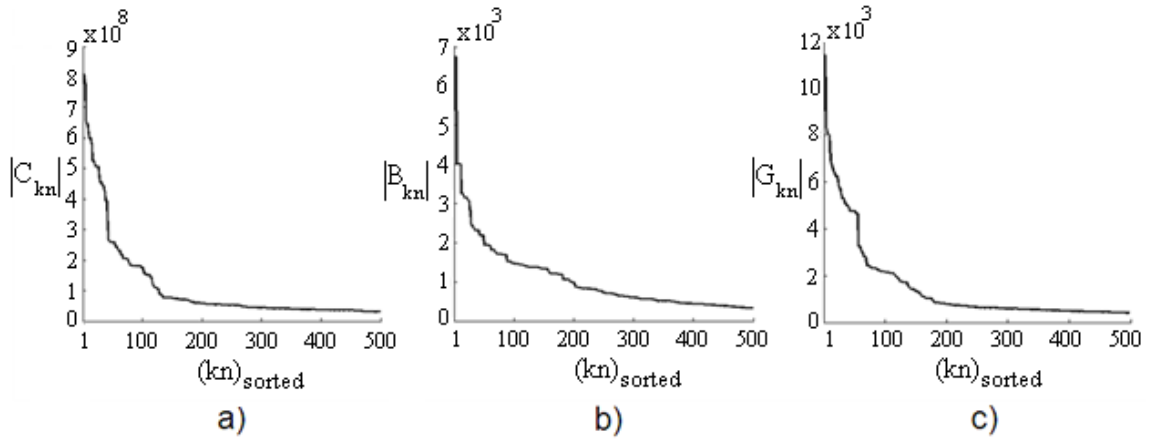


Figure 7 Magnitudes of dominant transforms (not including the zero transform) for (a) $\sigma'_{II}(g^p, \theta)$, (b) $W_{I_2}(g^p, \theta)$, and (c) $\sum_{\alpha} \dot{\gamma}(g^p, \theta)$. Note that the transforms were sorted by the magnitude before being plotted here.

An inverse DFT of any of the transforms described above will recover exactly the function values at all of the grid points (these are the function values that were used originally in computing the transforms). However, it is much more computationally efficient to simply compute directly the function value at the desired location using Eqs. (3.8)-(3.10), while exploiting the fact that there are only a limited number of dominant DFTs (as few as 200 terms based on Fig. 7). In order to recover the function values at any other location of interest (i.e. not on a grid point), we used the spectral interpolation technique. Spectral interpolation assumes that the DFTs were computed on a grid that is sufficiently finely discretized to capture all of the important frequencies embedded in the function of interest. In other words, a finer discretization would not reveal any new frequencies or any significant changes in the amplitudes of the frequencies already identified. Consequently, the function value at any new location in the domain of the function can be obtained by defining a new (finer) grid such that the point of interest lies

on a grid point in the new grid. The DFTs for the new finer grid can be obtained simply by padding the DFTs of the original grid with certain number of appropriately placed zeros to reflect the assumption that there are no new frequencies in the function.

The spectral interpolation scheme described above is clarified next with an example of a local interpolation. Let us consider the function $\sigma'_{11}(g, \theta)$. For simplicity of the presentation of plots, we fixed the values of some of the independent variables as $\phi_2 = 21^\circ$, $\Phi = 72^\circ$, and $\theta = 30^\circ$, and chose to vary only ϕ_1 . Let $\tilde{\sigma}'_{11}(\phi_1)$ represent this reduced function. Let $\tilde{\sigma}'_{11}(\phi_1)_j$ denote the function values sampled at equally spaced points, $\phi_{1j} = j \frac{L}{N}$, $j = 0 \dots N-1$, where N represents the number of grid points and L denotes the domain of interest in ϕ_1 (assumed to be periodic). This is depicted in Figure 8, with $N = 6$. This grid has been deemed adequate to capture all of the important frequencies embedded in $\tilde{\sigma}'_{11}(\phi_1)$. Let the DFTs computed from $\tilde{\sigma}'_{11}(\phi_1)_j$ be denoted as F_k . Let ϕ_1^* denote an interior point (not on the original grid) where it is desired to recover the value of the function. It is possible to design a finer uniform grid such that point ϕ_1^* lies at one of the grid points in the finer mesh. In the example shown in Fig. 8, the finer grid had a total of 36 grid points. The DFT corresponding to this finer grid is obtained simply by adding a total of 30 additional zeroes to F_k in appropriate locations. Let \tilde{F}_k denote this expanded DFT. An inverse DFT of the \tilde{F}_k provides an excellent interpolation of the function at all grid points in the finer mesh, including the point of interest, ϕ_1^* . In order to validate this concept, the value of the $\tilde{\sigma}'_{11}(\phi_1)$ was also computed directly on some of the finer grid points using the Taylor-type model and depicted in

Figure 8. It can be seen that the spectral interpolation is in excellent agreement with the correct values. It is also worth noting that it is not necessary to compute the interpolated values at all points on the finer grid; the DFT algorithms we used in this study allow one to compute the function values only at desired locations.

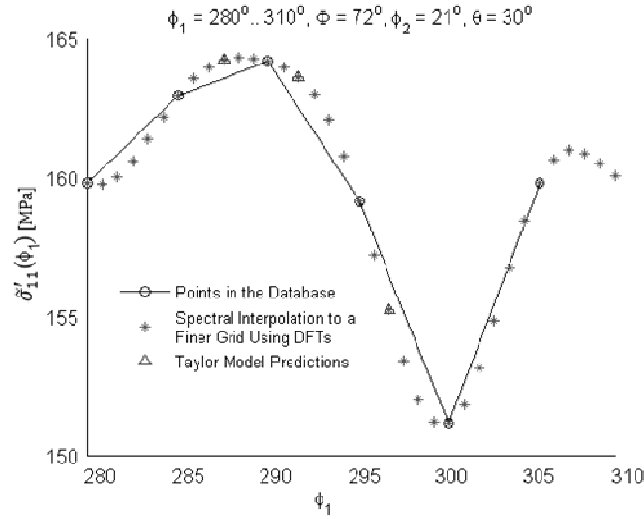


Figure 8 An example demonstrating the DFT interpolation scheme described in this thesis, and its validation by direct comparison with the corresponding predictions from the Taylor-type model used in this study.

Keeping a minimal set of dominant DFTs is the key for gaining computational speed in the spectral approach to the crystal plasticity computations described in this thesis. Taking into account more of the DFTs will improve the accuracy at the expense of computational cost. This important feature of the spectral approach will be demonstrated later with specific examples. In order to quantify the accuracy of the spectral representation using only the dominant transforms, we have defined appropriate normalized error metrics expressed in Eq. (3.11). In this equation, f denotes any one of the functions of interest computed using the conventional crystal plasticity approach,

while f^{DFT} represents the value computed using a selected set of dominant DFTs representing the same function. The normalization factor f^n has been selected to represent typical values of the function. For the results presented here, f^n was taken as $3s_o$ for the deviatoric stress components and as $3\dot{\epsilon}$ for the spin tensor components and the total shearing rate. Figures 9(a) – 9(c) plot the average percentage errors in the spectral representations of the functions of interest for a set of 100,000 randomly selected orientations subjected to randomly selected deformation modes. It can be seen that by retaining only the 500 dominant transforms for the stress tensor, the spin tensor and the total shearing rate, the average error is well below 5%.

$$e = \frac{1}{N} \sum_1^N \frac{|f - f^{DFT}|}{f^n} \times 100 \quad (3.11)$$

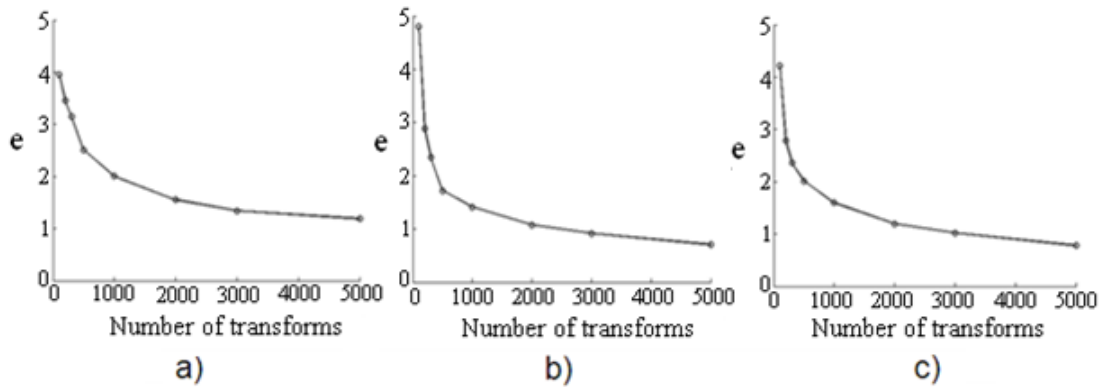


Figure 9 Average percentage error between the spectral predictions and direct computations for 100,000 randomly selected orientations subjected to randomly selected deformation modes as a function of the number of the dominant DFTs used in the spectral databases: (a) $\sigma'_{II}(g^p, \theta)$, (b) $W_{I2}(g^p, \theta)$, and (c) $\sum_{\alpha} \dot{\gamma}(g^p, \theta)$.

For visual comparison, we present in Fig. 10 contour plots in the orientation space for the stress function for a prescribed deformation mode, i.e. $\sigma'_{II}(g^p)|_{\theta=\theta_0}$. The plots compare function values computed using the conventional crystal plasticity computations and using the spectral methods described here with only the 500 dominant DFTs. It is seen that the DFT method described in this work reproduces faithfully the conventional crystal plasticity model predictions. Several other similar checks were conducted on the various functions of interest in this work.

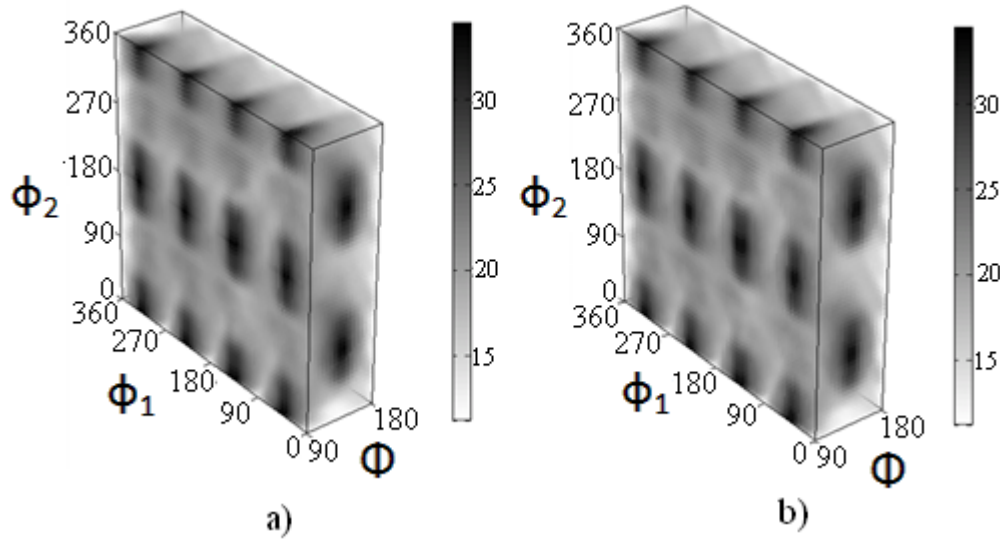


Figure 10 Contour plots of $\sigma'_{II}(g^p)|_{\theta=\theta_0}$ in Bunge-Euler space. (a) Computed using 500 dominant DFTs. (b) Computed using the conventional crystal plasticity approach.

The new approach presented in this thesis has been validated by comparing the solutions obtained by the conventional computational approaches against those obtained from the spectral approach described here for few selected examples of deformation processes. These comparisons will be presented shortly.

3.3. Spectral Crystal Plasticity of HCP Metals

The spectral approach to the conventional Taylor-type crystal plasticity calculations of hexagonal metals is presented in this section. The extension of the spectral crystal plasticity framework to hexagonal metals requires several modifications to the framework described in the previous section for cubic metals. Required modifications are due to the twinning and successive grain fragmentation and three distinct slip families that have different values of slip resistances (their values could be substantially different from each other).

As we did for cubic metals, we explore strategies that circumvent the need to repeatedly solve sets of highly non-linear, extremely stiff, algebraic equations with poor convergence characteristics that are inherent to these calculations (i.e. Eqs. 2.6 and 2.7). Following the same ideas, the strategies consist of computing only once all of the needed variables in crystal plasticity calculations, computing discrete Fourier transforms (DFTs), and storing only the dominant transforms (i.e. numerically significant ones) that can be later recursively used in any specific simulation. The essential variables are not only the components of the deviatoric stress and the lattice spin tensors, but also the sums of the shearing rates on individual slip families (basal, prism and pyramidal) and the sum of the twin volume fractions predicted by the Taylor-type crystal plasticity model for individual grains as a function of their lattice orientation, the imposed velocity gradient, and the set of slip and twin resistances. Note that the domain of these functions is eight dimensional and is defined to be the product space of the orientation space, the deformation mode, the set of three slip resistances and a twin resistance. In order to reduce dimensionality of the effective space we chose to normalize the set of the slip resistances with the twin

resistance. Therefore, the field variables are cast as functions of the ratios of the slip resistances and the twin resistance in hcp crystals in addition to the crystal lattice orientation and deformation mode. We seek the spectral representation of

$$\sigma'(g^p, \theta, s^{BAS}/s_{tw}, s^{PRI}/s_{tw}, s^{PYR}/s_{tw}), W^*(g^p, \theta, s^{BAS}/s_{tw}, s^{PRI}/s_{tw}, s^{PYR}/s_{tw}),$$

$$\sum_{\alpha} |\dot{\gamma}^{\alpha}|(g^p, \theta, s^{BAS}/s_{tw}, s^{PRI}/s_{tw}, s^{PYR}/s_{tw}) \quad \text{and} \quad \sum_{\alpha} |\dot{f}^{\beta}|(g^p, \theta, s^{BAS}/s_{tw}, s^{PRI}/s_{tw}, s^{PYR}/s_{tw}). \quad \text{It}$$

can be noted that the number of dimensions went from four for the cubic crystals to seven for hexagonal metals requiring more computational power for computation of the DFTs.

As an example, the spectral representation of stress using DFTs can be expressed as

$$\sigma'_{pqrstuv} = s_{tw} |\dot{\epsilon}|^m \text{sgn}(\dot{\epsilon}) \frac{I}{N_k N_l N_m N_n N_o N_p N_b} C_{klmnobj} e^{\frac{2\pi i k p}{N_g}} e^{\frac{2\pi i l q}{N_{\theta}}} e^{\frac{2\pi i m r}{N_g}} e^{\frac{2\pi i n s}{N_{\theta}}} e^{\frac{2\pi i o t}{N_g}} e^{\frac{2\pi i p u}{N_{\theta}}} e^{\frac{2\pi i b v}{N_g}}.$$

(3.12)

Similar expressions can be recognized for the other field variables. In order to compute the transforms, the functions values need to be computed on a uniform grid in the respective periodic domain. The orientation periodic unit cell is defined in section 2.1; the periodic space for the deformation mode had been defined in the previous section. It remains to establish the periodic spaces for the remaining three dimensions. This has been addressed by expressing each of the slip resistance ratios with a single angular variable. An example of parameterization of the basal slip to twin resistance ratio with $\lambda = [0, 2\pi)$ is

$$\frac{s^{BAS}}{s_{tw}} = \frac{\frac{s_o^{BAS}}{s_{tw}} + \frac{s_s^{BAS}}{s_{tw}}}{2} + \frac{\frac{s_o^{BAS}}{s_{tw}} - \frac{s_s^{BAS}}{s_{tw}}}{2} \cos(\lambda) \quad (3.13)$$

The same equation holds for the prism and pyramidal slip to twin resistance ratios. It remains to define boundaries of the slip-twin ratios. These ratios were established based on previous estimated hardening parameters and are chosen in such a way to be sufficient for broad range of Ti alloys: $s^{PRI}/s_{tw} = 0.1 - 1.0$, $s^{BAS}/s_{tw} = 0.75 - 2.5$, $s^{PYR}/s_{tw} = 0.5 - 2.5$. In the periodic domain, a regular grid has been designed to capture most of the important frequencies. It consisted of the five degree grid in the first three directions defined by the orientation space and twenty degree grid in the deformation mode and the slip-twin ratios. Figure 11 illustrates the variation of the magnitudes of the dominant DFTs (sorted by magnitude without including the zero transform which simply represents the average value of the function over the entire domain) computed for several variables.

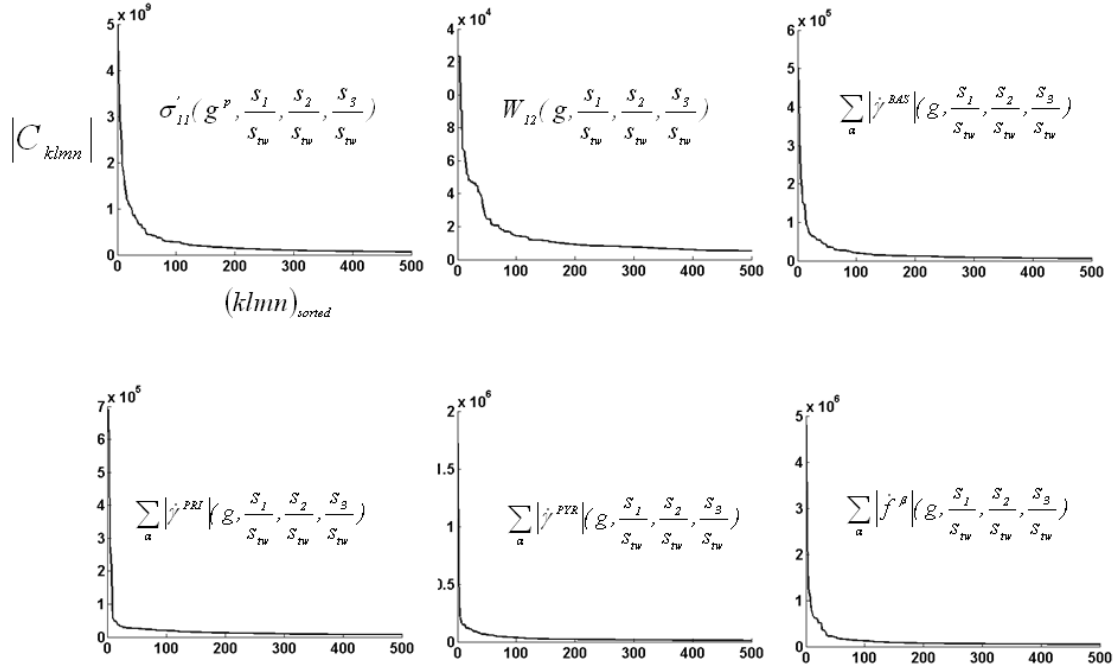


Figure 11 Magnitudes of dominant transforms (not including the zero transform) for the variables included in the plots. Note that the transforms were sorted by the magnitude before being plotted here.

A substantial compaction of the dataset is clearly possible for these functions. This new approach is validated through an example case study on commercial purity alpha-titanium in the next section.

3.4. Selected Spectral Crystal Plasticity Case Studies

Spectral crystal plasticity framework is validated by comparing the predicted anisotropic stress-strain response and texture evolution from the conventional crystal plasticity against those obtained by spectral approach developed here. To this end, several representative case studies of deformation processes are selected and discussed below for both fcc and hcp metals.

3.4.1. Plane Strain Compression in FCC Metals

In order to demonstrate the validity of the new DFT-based spectral approach described in this work, we simulated plane strain compression on polycrystalline OFHC copper to a true strain of $\varepsilon = -1.0$ along the compression axis. The polycrystal was assumed to possess a random initial texture that was captured by a set of 1000 discrete crystal orientations. We computed the deformed textures and the anisotropic stress-strain curves using the Taylor-type model, both by the traditional approach and the new DFT spectral approach based on the dominant transforms described here. In the DFT method, we applied Eqs. (3.8)-(3.10) recursively twenty times, each time for a true strain step of -0.05. In each strain step, the grain orientations were updated and the new orientations were used as the starting orientations in the next strain step. The predicted textures from the traditional approach are compared against those obtained from the DFT method using a minimal set of dominant transforms (134 for stress, 255 for lattice spin, and 182 for shearing rate) in Fig. 12(a), while the corresponding predictions of the stress-strain responses are shown in Fig. 12(b). Another calculation was performed using more of the dominant DFTs (500 for stress and 3000 for lattice spin and shearing rate) and its comparison with predictions from the traditional approach is presented in Fig. 13 (note the slight improvement in the accuracy of the spectral approach between Fig. 12 and Fig. 13). It is seen that the DFT method described here accurately reproduced all of the features of the Taylor-type model predictions.

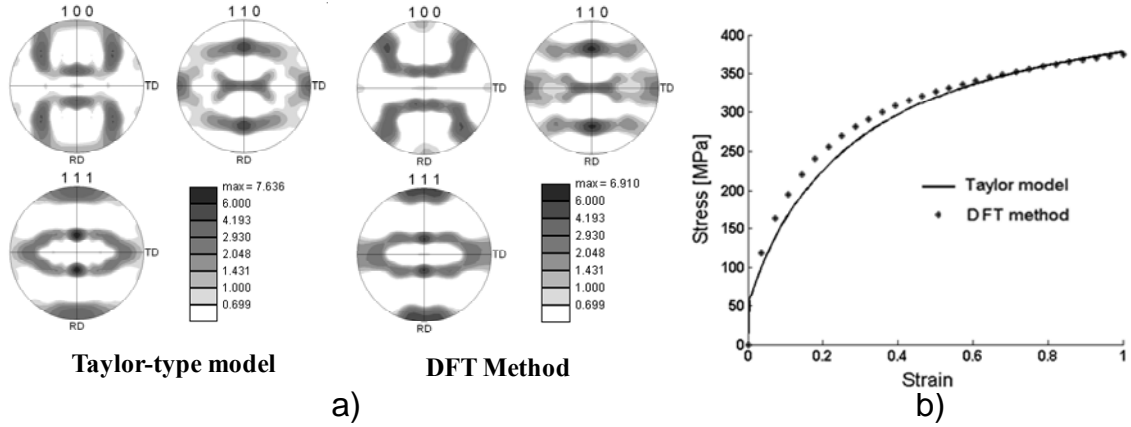


Figure 12 Comparison of the predictions from the spectral method described here, using a minimal set of 134 dominant DFTs for stress, 255 dominant DFTs for lattice spin, and 182 dominant DFTs for shearing rate, against the corresponding predictions from the conventional Taylor-type model for plane strain compression of OFHC Copper: (a) pole figures, and (b) stress-strain curves.

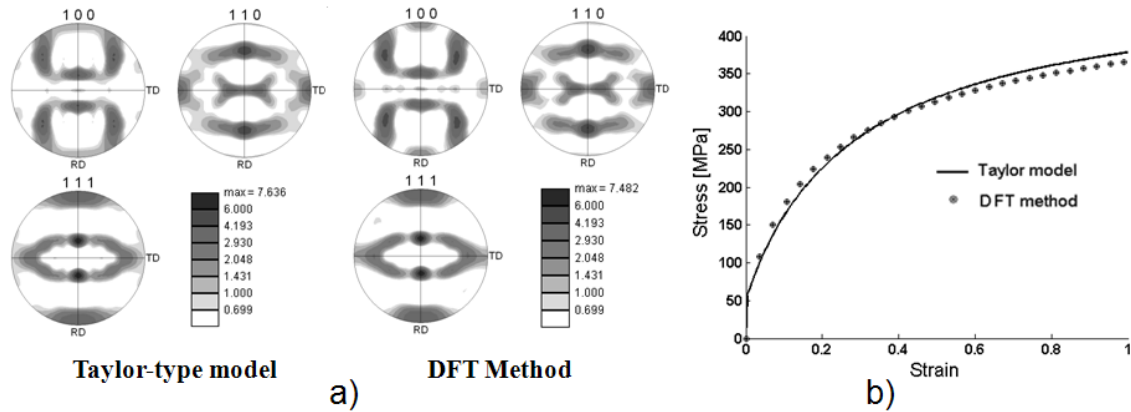


Figure 13 Comparison of the predictions from the spectral method, using 500 dominant DFTs for stress components and the shearing rate and 3000 dominant DFTs for the lattice spin components, against the corresponding predictions from the conventional Taylor-type model for plane strain compression of OFHC Copper: (a) pole figures, and (b) stress-strain curves.

This simulation took 108 seconds on a regular Pentium 4 desktop PC using the conventional crystal plasticity algorithms (solving explicitly Eqs. (2.6) and (2.7)) and 0.7 seconds using the minimal set of the dominant DFTs, and 2.3 seconds using the larger number of dominant DFTs. Thus, an attractive feature of this new approach is that it provides the user with tremendous flexibility in making trade-offs between accuracy and

computational speed. In other words, the new spectral database described in this paper will allow the user to perform a large number of very quick simulations at a lower than desired accuracy, identify the specific ones that appear to produce promising results, and redo these much more accurately (at a higher computational cost). This represents a tremendous savings in computational time.

3.4.2. Simple Shear in FCC Metals

As the next case study we simulated simple shear deformation, where the principal orientations of the imposed stretching tensor do not coincide with the sample reference frame. The sample was assumed to have the same random initial texture as in the previous case study, and was subjected to a strain of $\gamma = 1.0$. The predictions from the new DFT spectral approach based on the 500 dominant DFTs for the stress components and the shearing rate, and 3000 dominant DFTs for the lattice spin components are compared against the corresponding predictions from the conventional Taylor-type model calculations in Fig. 14. It is seen once again that the DFT method described here provides excellent predictions at a significantly faster computational speed. This prediction took 107 seconds on a regular PC for the conventional Taylor-type calculations, but only 2.4 seconds for the DFT based spectral methods described in this thesis.

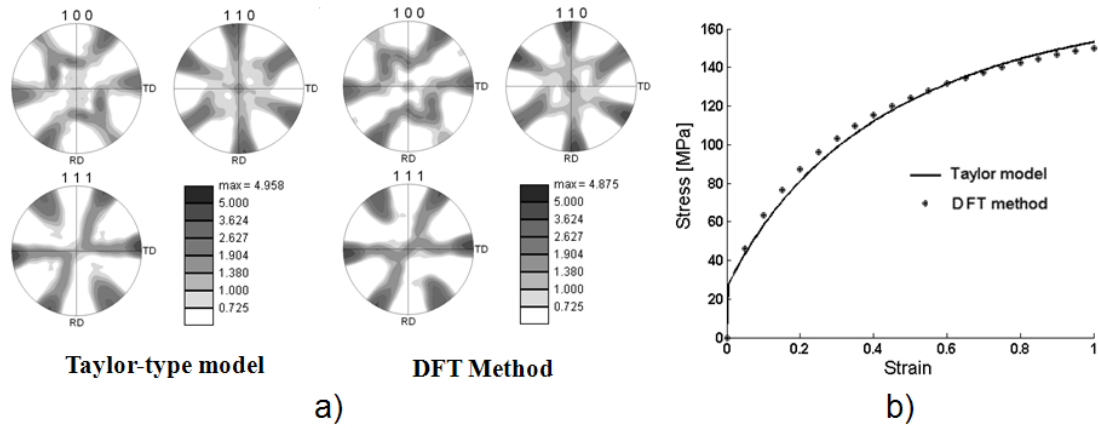


Figure 14 Comparison of the predictions from the spectral method, using 500 dominant DFTs for stress components and the shearing rate and 3000 dominant DFTs for the lattice spin components, against the corresponding predictions from the conventional Taylor-type model for simple shear of OFHC Copper: (a) pole figures, and (b) stress-strain curves.

3.4.3. Plane Strain Compression Followed by Simple Shear in FCC Metals

As the next case study we simulated plane strain compression followed by simple shear deformation. The sample was assumed to have the same random initial texture as in the previous case studies, and was subjected to a strain of $\varepsilon = -0.5$ in plane strain compression followed by a $\gamma = 0.5$ in simple shear. The predictions from the DFT method described here are also compared against the corresponding predictions from the conventional Taylor-type model calculations in Fig. 15. It was seen once again that the DFT method described here provides excellent predictions at significantly faster computational speeds similar to those reported in the other case studies described earlier.

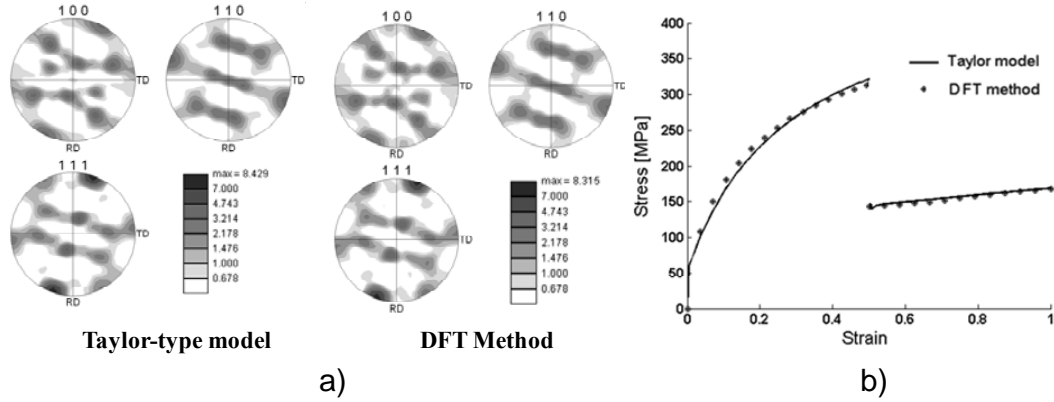


Figure 15 Comparison of the predictions from the spectral method, using 500 dominant DFTs for the stress components and the shearing rate and 3000 dominant DFTs for the lattice spin components, against the corresponding predictions from the conventional Taylor-type model for a deformation mode involving a path change (plane strain compression up to strain of 0.5 followed by simple shear up to strain of 1.0) of OFHC Copper: (a) pole figures, and (b) stress-strain curves. The stresses and strain plotted are axial components during plane strain compression and shear components during simple shear.

3.4.4. Equi-Channel Angular Extrusion in FCC Metals

As another example, we present a simulation of texture evolution in a more complex non-monotonic deformation process. In this example, Hamad F. Al-Harbi, a research student in our group performed a simulation of the ECAE (Equi-Channel Angular Extrusion) process using a commercial finite element software package FORGE3 [108]. The deformation history was extracted at three different locations in the billet: one close to the top, one at the middle, and one close to the bottom of the billet. The extracted deformation histories were provided as inputs to the Taylor-type DFT-based crystal plasticity model described above.

The initial texture was assumed to be random and numerically approximated by a set of 1000 discrete crystal orientations. The (111) pole figures of the predicted textures using the DFT based crystal plasticity at the selected locations in the billet after one pass of ECAE were in reasonable agreement with the experimentally measured textures , as

shown in Fig. 16. However, the agreement is much better for the top and the middle locations on the billet compared to the bottom location on the billet. It is known that grain interactions and the associated anisotropy in the mechanical response of the material play an important role in the texture gradients obtained in the ECAE process [1,109]. Since neither of these aspects of material behavior were incorporated in the present study, it is only reasonable to see some discrepancies between the predictions and the experimental measurements in Fig. 16. However, it is gratifying to see that the present model is able to capture to a reasonable extent the texture gradients obtained in the highly complex ECAE process.

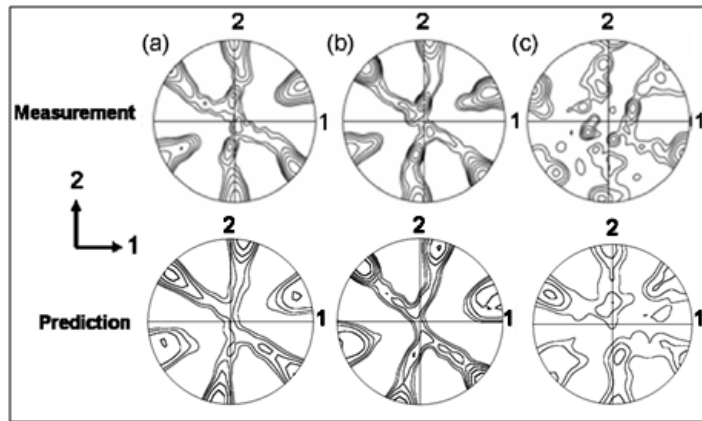


Figure 16 Comparison of the predicted (111) pole figures using the DFT based crystal plasticity at different locations in the billet after one pass with the corresponding measurements taken from [1]. (a) Top of the billet. (b) Middle of the billet. (c) Bottom of the billet. Contours from experiments and model: 1/1.4/2/2.8/4/5/6/8/11.

3.4.5. Plane Strain Compression in HCP Metals

In order to demonstrate the validity of the DFT-based spectral approach for hcp metals, we simulated plane strain compression on polycrystalline α -Ti to a true strain of $\varepsilon = -1.0$ along the compression axis. The polycrystal was assumed to possess the same

random initial texture as all previous fcc case studies. We computed the deformed textures and the anisotropic stress-strain curves using the Taylor-type model, both by the traditional approach and the new DFT spectral approach based on the dominant transforms for hcp metals. In the DFT method, we applied the spectral linkages recursively twenty times, each time for a true strain step of -0.05. In each strain step, the grain orientations were updated and the new orientations were used as the starting orientations in the next strain step. In addition, the number of orientations was increasing due to grain fragmentation induced by twinning from last to the next strain step. This increase in the number of orientations was present until twinning saturated in all grains that undergone twinning. The predicted textures from the traditional approach are compared against those obtained from the DFT method using a set of 1000 dominant transforms for each of the field variables (the stress, the lattice spin, the three sums of shearing rates, and the sum of twin volume fractions) in Fig. 17(a), while the corresponding predictions of the stress-strain responses are shown in Fig. 17(b). It is seen that the DFT method described here accurately reproduced all of the features of the Taylor-type model predictions for hcp metals, too.

This simulation took 172 seconds on a regular Pentium 4 desktop PC using the conventional crystal plasticity algorithms (solving explicitly Eqs. (2.6) and (2.7)) and 5.7 seconds using the dominant DFTs. Ones more, this represents a tremendous savings in computational time.

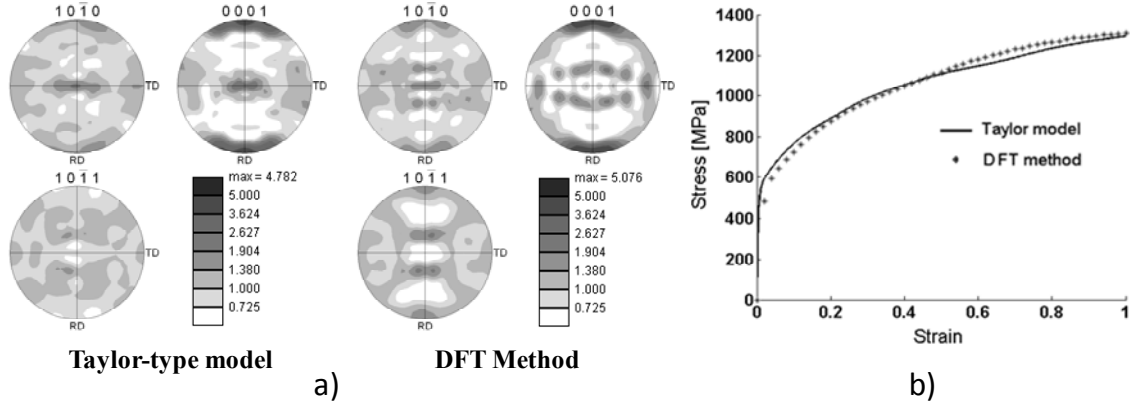


Figure 17 Comparison of the predictions from the spectral method described here, using a set of 1000 dominant DFTs for each of the field variables, against the corresponding predictions from the conventional Taylor-type model for plane strain compression of α -Ti: (a) pole figures, and (b) stress-strain curves.

3.5. Delineation of Yield Surfaces Using DFTs

The yield surface is a boundary between the elastic and the plastic deformation regimes for all possible stress states. While it is possible, in principle, to characterize the complete anisotropic yield surface of a given work-piece via experimental testing, it is quite cumbersome, requiring specialized test machines and fixtures. The more commonly used approach is to develop a mathematical tool that can predict the yield surface based on a limited number of simple experimental measurements. In this study, the state of stress is characterized by the Cauchy stress deviator predicted by Taylor-type crystal plasticity model, thus the yield surface is five dimensional and contains all the stress states that cause yielding. The shape, size and orientation of the anisotropic yield surface are expected to vary strongly with texture. Combining the developed database of spectral coefficients for predictions of the stress deviator and the DFT based homogenization, we present in this section a mathematical procedure for fast computation of the anisotropic

crystal plasticity based yield surfaces. The volume average stress for a given texture and a specific deformation mode in the principle frame can be computed as

$$\bar{\sigma}'_{ij}(\theta) = \frac{I}{\pi^2} \int_{FZ3} f(g^p) \sigma'_{ij}(g^p, \theta) \sin \Phi d\phi_1 d\Phi d\phi_2. \quad (3.14)$$

The integral in the Eq. (3.14) can be computed using the orthogonal properties of the spectral representations. Since we already have DFTs for stress, it is convenient to combine $\sin \Phi$ with $f(g)$, thus we seek here a DFT representation of

$$\tilde{F}_k = \sum_{b=0}^{B-1} f_b \sin \Phi_b e^{\frac{-i 2 \pi b k}{B}}. \quad (3.15)$$

The volume average stress can then be written as

$$\bar{\sigma}'_q = \frac{I}{BN_\theta} \sum_n \sum_k C_{kn} \tilde{F}_k^* e^{\frac{2 \pi i n q}{N_\theta}} \quad (3.16)$$

Note, the star on \tilde{F}_k indicates the complex conjugate quantity. It may be beneficial to remind ourselves that the sets of coefficients C_{kn} are independent of the values of the variables g^p and θ . In Eq. (3.16), q enumerates the grid points in the deformation mode space. Therefore, Eq. (3.16) would produce q points on the yield surface. However, this is not yet a complete yield surface of a given polycrystal. In order to compute an entire yield surface of the given polycrystal using DFT method one needs to select a certain

number of principle frames and transform the original texture to all of them and then for each transformed texture use Eq. (3.16) to compute the stress deviator components. The principle frames are selected from the following orthorhombic space

$$(\beta_1, \beta_2, \beta_3) \mid 0 \leq \beta_1 < 2\pi, 0 \leq \beta_2 \leq \frac{\pi}{2}, 0 \leq \beta_3 \leq \pi .$$

Note that the computed stress in the selected principle frames needs to be transformed back to the sample frame of the original texture. The collection of all these points is the yield surface.

The yield surfaces for two textures were efficiently delineated using the described procedure. The pole figures for a random texture and an (111) fiber texture represented each by 1000 crystals are shown in the Fig. 18(a) and 18(d), respectively. The selected projections of the corresponding yield surfaces are shown in the Fig. 18(b) and 18(c) for the random texture and Fig. 18(e) and 18(f) for the fiber texture. The different shape of the yield surfaces for the two different textures should be noted from the plots. The computational time needed for the delineation of a yield surface for a texture represented by 1000 crystals was 8 seconds on a regular Pentium 4 desktop PC.

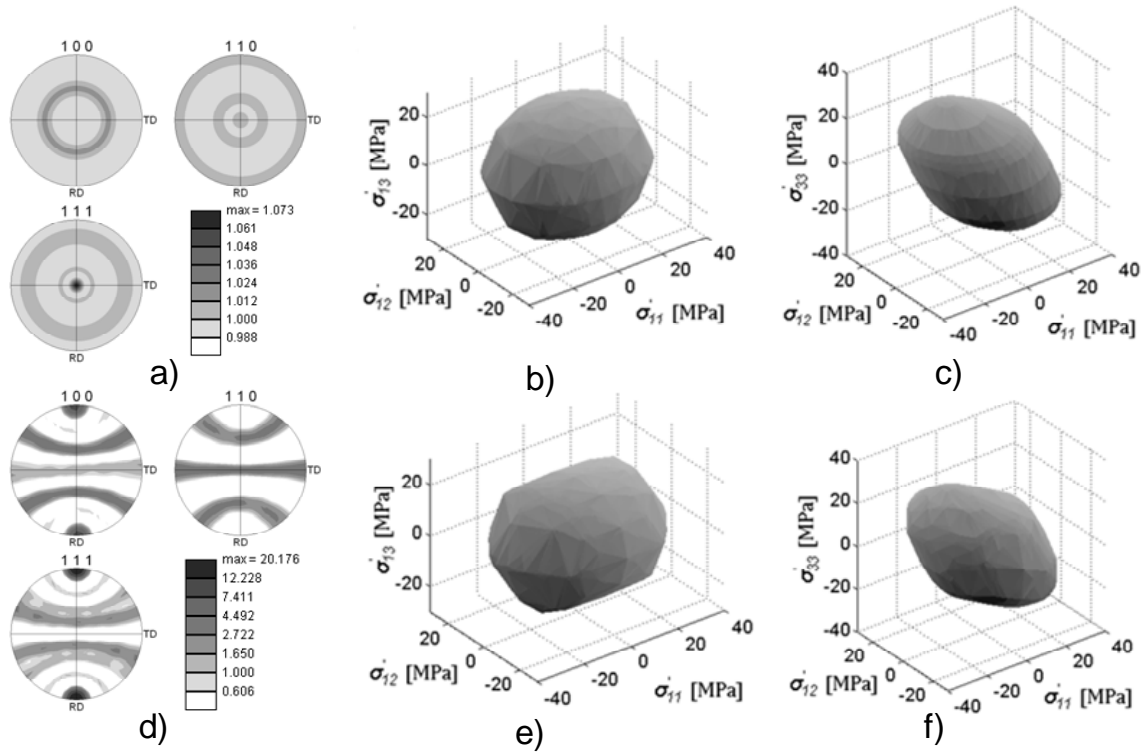


Figure 18 a) pole figures for the random texture, b) and c) selected projections of the yield surfaces for the random texture, d) pole figures for the (111) fiber texture, e) and f) selected projections of the yield surfaces for the fiber texture. The different shape of the yield surfaces for the two different textures should be noted.

Although the yield surface is an important and valuable construct in the design we will use it here only to establish the tensile yield stress in delineating the property closures for triclinic textures. From the yield surface the yield stress can be established for any stress state. Specifically, we are looking for the intersection of $(1, 0.5, 0, 0, 0)$ vector and the yield surface. The intersection point is established using Gram-Schmidt orthonormalization [39].

3.6. Property Closures and Microstructure Design

In this section, results and insights from numerous examples of atlases of property closures corresponding to selection of different pairs of effective elastic-plastic properties of interest are provided. The relevant material properties are defined in the Appendix A. New mathematical procedures established in this thesis for delineation of both the property closure that do not require and the property closures that require consideration of the strain hardening and texture evolution are presented in Appendix B and Appendix C, respectively.

3.6.1. Atlases of Elastic-Plastic Property Closures

We start with a selection of a pair of effective elastic properties, C_{1111}^* and C_{1313}^* . These correspond to the effective modulus in uniaxial strain and the effective shear modulus in the sample, and play an important role in the design of components subjected simultaneously to axial loads and twisting moments. The values of $F_l^{\mu\nu}$ (or F_k using DFTs) coefficients corresponding to the boundary points on the (C_{1111}^*, C_{1313}^*) closure were obtained using the methods described in the previous sections. Using these coefficients, the (C_{1111}^*, C_{1313}^*) closures have been produced for a broad range of cubic materials with different anisotropy ratios A , and these are depicted in Fig. 19 as an atlas of closures. The shaded areas inside the closures represent all of the possible combinations of the selected elastic stiffness components that can be obtained according to the first-order bounding theories for the particular material. Figure 19 reveals that the shapes of the property closures shown can be broadly classified into two groups. These correspond to materials with the A ratio being greater and smaller than one, respectively. For example, *Mo* and

LiO exhibit values of A less than one, while all of the other materials in Fig. 19 exhibit values of A larger than one. Note also that the relative (normalized) size of the closure scales with the magnitude of $(A-1)$. For example, Tungsten with A ratio close to 1.0, exhibits the smallest closure, while $MgAl_2O_3$ with an A ratio of 2.43 exhibits one of the larger closures obtained. Obviously, with larger closures there exists a higher potential for improvement of performance in a given design application.

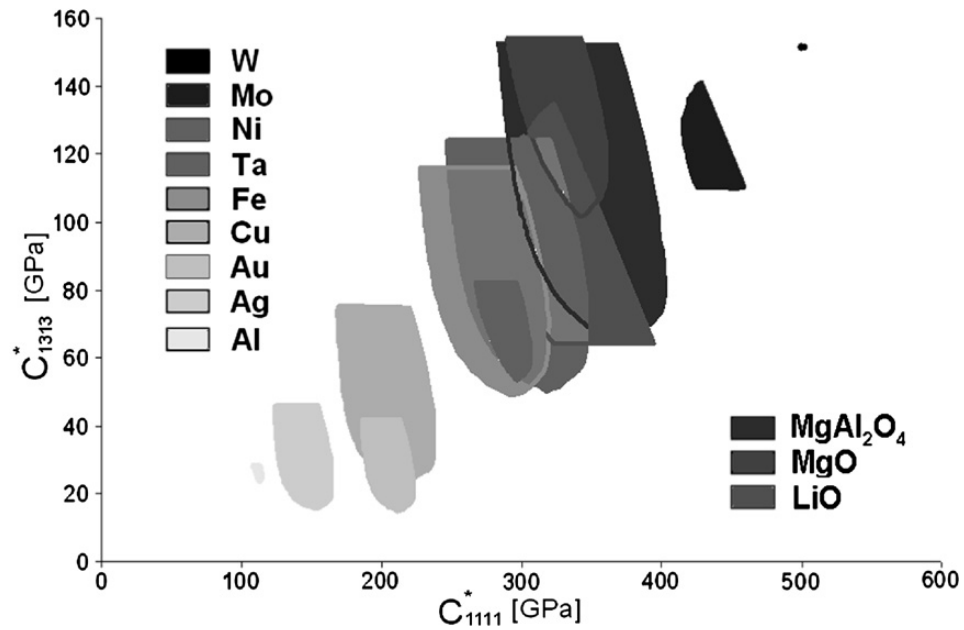


Figure 19 Atlas of $C_{1111}^*-C_{1313}^*$ closures for a broad selection of cubic materials.

Figure 20 depicts the same type of the closure but for multiphase materials. Polycrystalline beta Ti-Nb phase, Ti alpha phase and mixtures of these two phases were considered examples. This multiphase closures are of particular interest for biomedical applications. It is desirable to design implants with stiffness values that is as close as

possible to the stiffness of the skeleton since the stress shielding effect depends on the difference between the stiffness of an implant component and the stiffness of the bone.

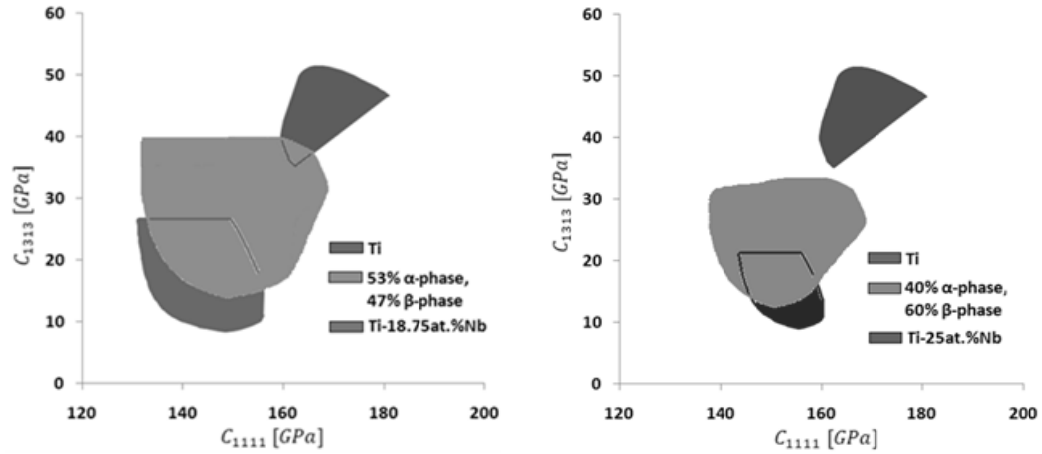


Figure 20 C_{1111} - C_{1313} closures for alpha Ti, beta Ti-Nb, and mixture of alpha and beta Ti phases.

As final examples of the closures involving elastic properties we present in the Fig. 21 two different combinations of the elastic stiffness components. The closure involving the effective pair of the C_{1111} - C_{1112} properties is only relevant for the triclinic textures since C_{1112} component of the elastic stiffness for orthorhombic textures is zero. This signifies the potential role of processing symmetry on the anisotropy of the properties.

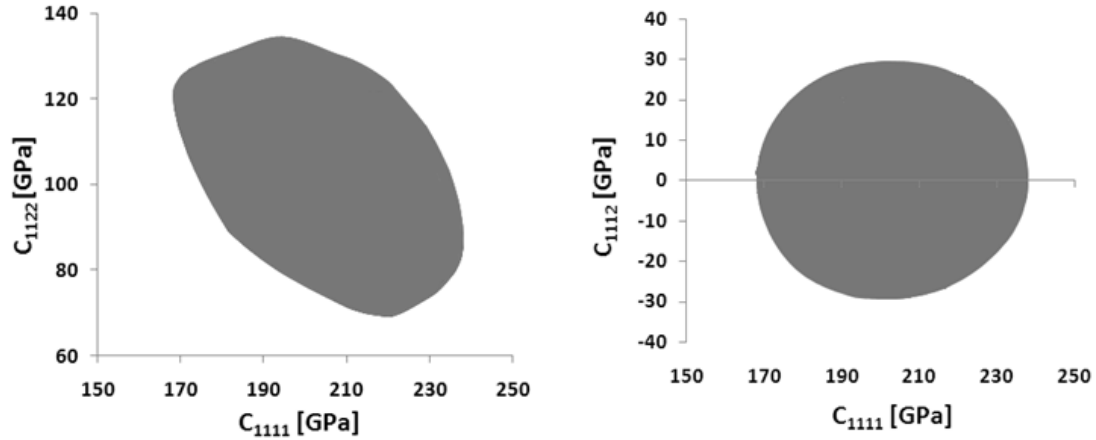


Figure 21 C_{1111} - C_{1122} , and C_{1111} - C_{1112} closures for copper polycrystals.

As the next example, we consider closures for $(C_{1111}^*, \sigma_{y1}/s)$ that has an important role in design of compliant beam mechanisms and other similar components [36,96]. Once again we obtained the values of the $F_l^{\mu\nu}$ or F_k coefficients corresponding to the boundary of the closure using the methods described earlier, and then use these coefficients to produce closures for different material systems. This particular closure has been focused on fcc metals where the operating slips systems are known to be $(111)\langle 1\bar{1}0 \rangle$ systems. The set of Fourier coefficients needed to plot the closure have to be recomputed for a different class of metals with a different set of operating slip systems (e.g. bcc metals). Figure 22 presents an atlas of $(C_{1111}^*, \sigma_{y1}/s)$ closures for a range of fcc metals. Not surprisingly, the range of feasible values for the effective plastic yield is significantly larger than the range of feasible elastic properties in this class of materials.

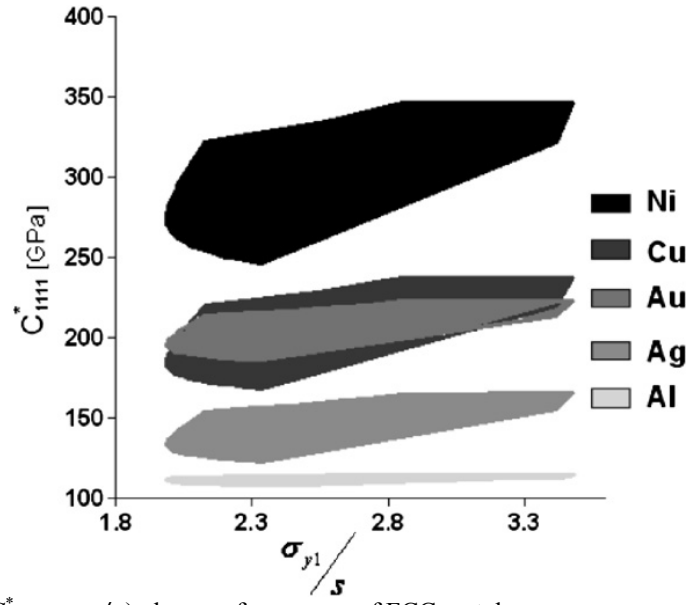


Figure 22 Atlas of $(C_{111}^*, \sigma_{y1}/s)$ closures for a range of FCC metals.

As a next example, we consider the $(R_l, \sigma_{y1}/s)$ closure. This closure has many applications in the metal sheet forming industry. A higher value of R_l typically indicates better sheet workability and a lower value of σ_{y1} would lead to lower load requirements in the forming operation. Once again, we obtain the Fourier coefficients corresponding to the boundary points on this closure using the methods described before. In this specific example, the closure obtained is actually a universal closure for all fcc metals, subject to the assumptions that only $(111)\langle 1\bar{1}0 \rangle$ slip systems are allowed to operate and exhibit the same slip resistance. This closure is presented in Fig. 23.

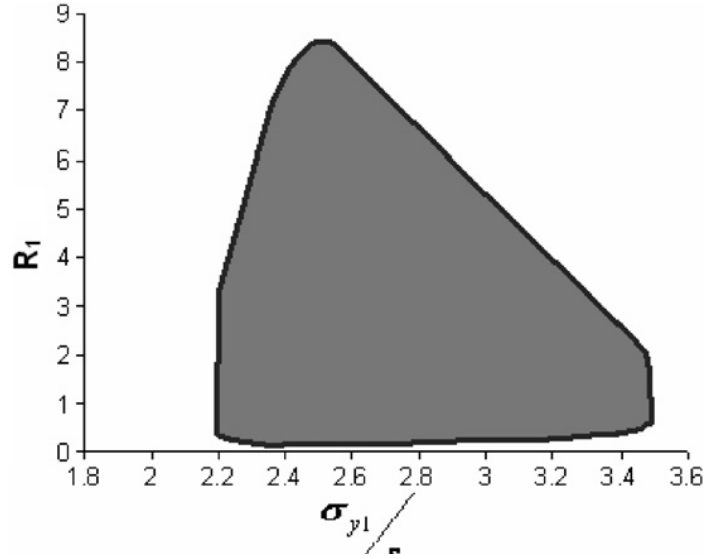


Figure 23 (C_{1111}^* , σ_{y1}/s) closure for all FCC metals.

An example of the closures involving elastic properties of triclinic textures revealed more available property combinations than for the orthorhombic textures. The restriction on the orthorhombic textures may reflect on the size of the property closures involving tensile yield stress. In order to investigate if the closures for the triclinic textures is bigger we next consider an example of a closure for the triclinic textures (i.e. no sample symmetry) involving yield stress. As described in the section 3.5, in order to delineate the closure involving the tensile yield stress with no sample symmetry the tensile yield stress needs to be established using the yield surfaces.

Figure 24(a) depicts the triclinic closure for polycrystalline copper whereas Fig. 24(b) shows comparison between the closures for copper with the assumption of the two different sample symmetries. It is evident that there are indeed more property combinations available if there is no restriction on the sample symmetry in the material.

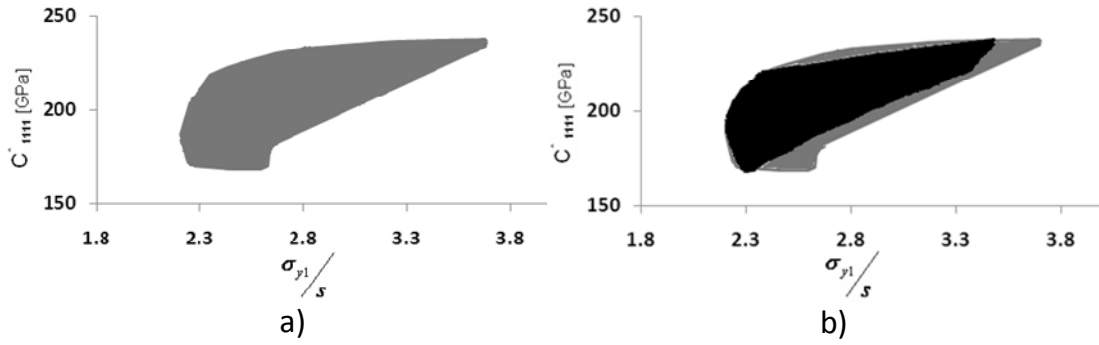


Figure 24 a) $(C_{1111}^*, \sigma_{y1}/s)$ upper bound closure for copper polycrystals with no sample symmetry. b) Comparison between upper bound orthorhombic (black) and upper bound triclinic (gray) closures of polycrystalline copper.

3.6.2. Performance Optimization Case Study: Compliant Mechanism

At this point, we point out that the microstructure-property linkages established are invertible (because they are simple algebraic equations) and can be used in microstructure design. The optimization problem for microstructure design involving components with statistically homogeneous microstructures can be formulated as

$$\text{Maximize } O(\rho), \text{ where } \rho = (P_1(\alpha), P_2(\alpha), \dots, P_N(\alpha)), \text{ subject to } \alpha_p \geq 0, \sum_p \alpha_p = 1, \quad (3.17)$$

where O denotes a objective function characterizing the performance of the mechanical component, ρ is a set of relevant macroscale material properties (denoted as $P_i(\alpha)$) influencing the performance, and α_p denotes volume fraction of a single crystal of orientation g^p in the polycrystal. The procedure will be demonstrated using an example case study for microstructure design of a compliant beam involving polycrystalline α - Ti.

The microstructural design variable for this study has been selected to be the ODF (or texture) in the beam. Since the sample is made from a hexagonal metal and the macroscale properties are expected to exhibit orthorhombic symmetry, the space of relevant ODFs for this case study is the class of hexagonal-orthorhombic ODFs.

Compliant mechanisms are single-component flexible structures that deliver a desired motion by undergoing elastic deformation [110]. In this case study, we will seek the texture(s) that will maximize the deflection of the beam without initiating plastic deformation.

The compliant mechanism is idealized here as a long slender cantilever beam whose macroscale elastic-plastic properties exhibit orthorhombic symmetry (presumably the processing options have been restricted to accomplish this). The stress field in the cantilever beam, with one end fixed to a rigid surface and the other end subjected to a point load P is expressed as [111]

$$\sigma_{11} = -\frac{12P}{hw^3}x_1x_2, \quad (3.18)$$

where h and w are the beam height and width, respectively. Since the normal stresses are much higher than the shear stresses in a slender beam, we have ignored the shear stresses in this case study.

The application of Hill's anisotropic yield criterion requires

$$\frac{|\sigma_{11}|}{\sigma_{y1}} \leq 1. \quad (3.19)$$

The maximum deflection in the cantilever beam, at the time of the initiation of plastic strain, is expressed as

$$\delta = \frac{2}{3} \sigma_{y1} S_{1111} \frac{L^2}{w}, \quad (3.20)$$

where L is the length of the beam. For a fixed beam geometry, the maximum deflection that can be attained without initiating plastic strain is therefore dependent only on the macroscale material properties S_{1111} and σ_{y1} . In the case study presented here, the beam is assumed to have a square cross section with $b = w = 18 \text{ mm}$, and $L = 180 \text{ mm}$.

By coupling the constitutive equations of material behavior with a spectral representation, the inverse design methodology is enabled for optimal material design. An optimal solution is obtained by searching the complete set of all theoretically feasible ODFs and associated properties. The property closure, together with the optimal property combination for the case study, with a corresponding texture, will be presented later.

In the subsequent section a procedure for processing network will be developed to help designer realize the identified texture.

A closure depicting the complete set of feasible combinations of S_{1111} and σ_{y1} for all theoretically feasible hexagonal-orthorhombic textures in the selected α -Ti metal was obtained using the procedures described earlier and plotted in Fig. 25. Performance contours for maximum deflection (based on Eq. (3.20)) have been superimposed on this

figure. The maximum deflection attainable in the compliant beam with isotropic properties (corresponding to a random texture) is 2.41 mm, while the expansion of the design space to the set of hexagonal-orthorhombic textures provides performances ranging from 1.01 mm to 3.31 mm. The best performance represents a 37% improvement over that of the isotropic solution. It is just as important to note that ignoring the inherent texture in the sample can result in extremely poor performance of the component (58% reduction in performance compared to the isotropic solution).

The best performance in this design case study corresponded to a yield strength of 322.6 MPa (close to the maximum yield strength possible in the selected material system, which was 329.23 MPa) and a compliance of 0.0086 GPa^{-1} (which is significantly lower than the maximum possible compliance of 0.0096 GPa^{-1}). This is because the combination of the highest yield point and the highest compliance is not feasible in any one texture. The best feasible performance resulted from a trade-off between yield strength and compliance. It is also worth noting that the worst performance corresponded to the lowest yield strength, in spite of the fact that it exhibited the highest compliance. Clearly, the value of the yield strength dominated this design.

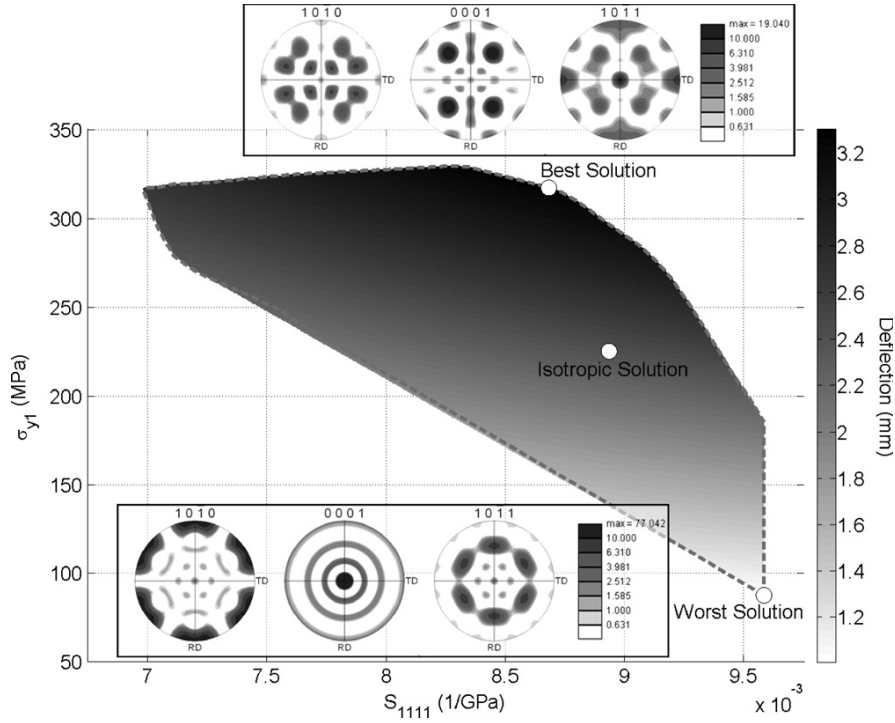


Figure 25 The relevant property closure for a cantilever compliant beam made of high-purity polycrystalline α -Ti with hexagonal-orthorhombic textures. The texture predicted to provide the best and the worst performances for this case study are also shown.

The RD direction in the pole figures shown in Fig. 25 corresponds to the beam axis. The best performance was observed to correspond to a texture with the crystal (0001) planes inclined at a small angle to the RD axis, while the worst performance corresponded to a texture with the (0001) planes inclined at about 90 degrees to the RD axis. This is consistent with the results described above, because the yield strength of a titanium single crystal is expected to decrease significantly as the (0001) plane is tilted away from the loading direction.

3.6.3. Closures of Plastic Properties Requiring Explicit Consideration of Strain Hardening and Crystallographic Texture Evolution

The first-order closures presented in this section differ substantially from those in the previous sections by showing the set of theoretically feasible plastic property combinations while taking into account strain hardening and concurrent texture evolution due to plastic strain. Three specific examples of these closures for two fcc metals: oxygen-free high-conductivity (OFHC) copper, and Al 5754-O are provided and discussed.

The first-order closure for the ultimate tensile strength (σ_{UTS}) and the yield strength (σ_{y1}) in Fig. 26 is expected to be of interest to mechanical designers as they seek superior combinations of these two properties in their designs. It is observed that the closures for the two metals selected in this study are strongly influenced by the strain hardening parameters. The slight vertical translation of the 5754-O Al closure with respect to the OFHC Copper closure can be easily explained based on the slightly higher value of the initial slip resistance used for 5754-O Al (17 MPa) compared to the value used for OFHC Copper (16 MPa). The significant horizontal translation of the 5754-O Al closure compared to the closure for OFHC Copper in Fig. 26 has to be attributed to the differences in the slip hardening parameters for these two metals. It is especially noteworthy that 5754-O Al exhibits higher values of σ_{UTS} in spite of a lower saturation value of slip resistance (130 MPa for 5754-O Al versus 148 MPa for OFHC Copper). These higher values σ_{UTS} are attributed to the significantly higher strain hardening rates in 5754-O Al compared to OFHC Copper (h_o is 180 MPa for OFHC Copper while it is 745 MPa for 5754-O Al).

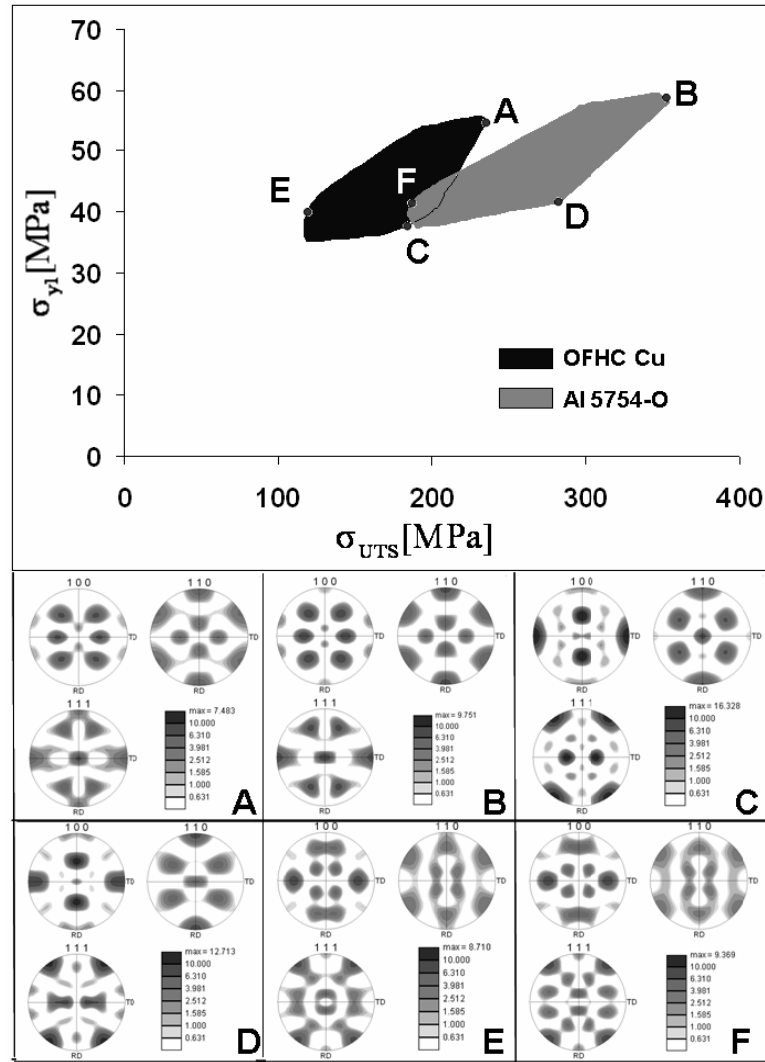


Figure 26 First-order closures for the ultimate tensile strength (σ_{UTS}) and the yield strength (σ_{y1}) in OFHC Cu and 5754-O Al based on Taylor-type models and a consideration of all theoretically possible textures (i.e. the elements of the texture hull). The textures that are theoretically predicted to correspond to salient points of interest on the boundary are depicted. Textures A, C, and E are for OFHC Copper, while textures B, D, and F are for 5754-O Al.

Textures corresponding to corners A and B are theoretically identified to possess the combination of the highest values of σ_{y1} and σ_{UTS} feasible in the materials studied here.

It should, however, be noted that these predictions are based on the selected

homogenization theory (Taylor-type model) and the prescribed slip hardening parameters. Examples of textures corresponding to corners A and B are presented in Fig. 26. It is seen that the main texture component providing this optimal combination of properties appears to be the $(111)[\bar{1}\bar{1}0]$ in both materials, and is not a major component in any of the widely used deformation processing operations by the metal working industry. On the other hand, materials processing specialists relate the ratio of the yield strength to the ultimate tensile strength of the metal to its strain hardening response. Generally, a lower value of σ_{y1}/σ_{UTS} is correlated to higher capacity for plastic deformation. For example, textures corresponding to points C and D in Fig. 26, for OFHC copper and 5754-O Al, respectively, exhibit the lowest value of σ_{y1}/σ_{UTS} in these metals. The dominant texture component in both textures C and D is close to the $(110)[\bar{1}\bar{1}0]$ orientation. The slight differences between these textures and their influence on the properties of interest will be discussed shortly. Textures corresponding to points E and F in Fig. 26 provide much lower values of both σ_{y1} and σ_{UTS} , and may be of interest to processing specialists because of the lower load requirements in metal shaping operations (provided they exhibit adequate ductility). The dominant texture component in both textures E and F is close to the $(121)[0\bar{1}2]$ orientation, while there are again subtle differences between them.

The subtle differences in the optimal textures for the two different metals studied here reflect the important role of strain hardening in influencing strength. To illustrate this, we have calculated the properties of 5754-O Al corresponding to salient textures A, C, and E (these were initially identified on the closure for OFHC Copper). Likewise, we have also

computed the properties of OFHC Copper corresponding to salient textures B, D, and F (initially identified on the closure for 5754-O Al). The property combinations for all textures A through F are shown in Fig. 27 on closures for both metals. It is seen that the differences between textures A and B have very little effect on the σ_{y1} and σ_{UTS} of these two metals, while the differences between textures C and D and between textures E and F result in significant differences in the σ_{y1} and σ_{UTS} exhibited by these two metals. These observations confirm our expectation that the strain hardening parameters do play a significant role on the class of plastic closures presented in this paper.

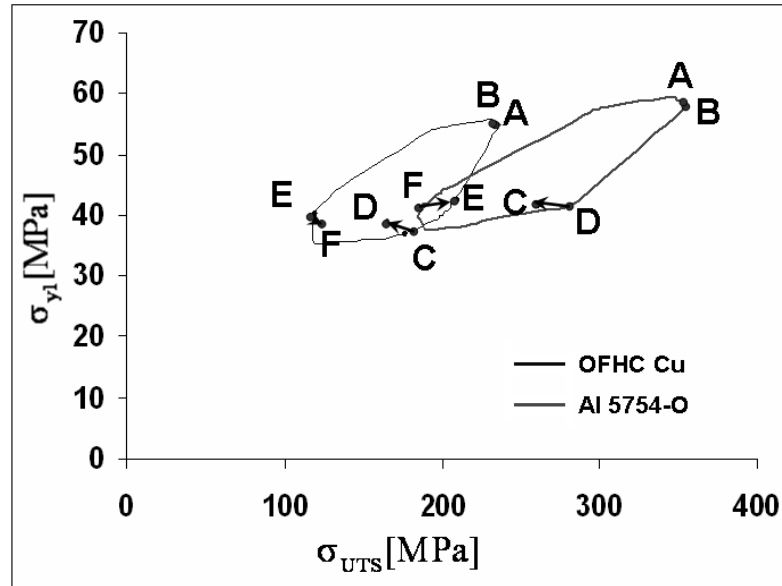


Figure 27 Influence of the subtle differences in the textures on the ultimate tensile strength (σ_{UTS}) and the yield strength (σ_{y1}) exhibited by the metal. The properties corresponding to pairs of slightly different textures (A, B), (C, D), and (E, F) are shown on closures for 5754-O Al and OFHC Copper.

Figure 28 depicts property closures for uniform ductility (e_u) and ultimate tensile strength (σ_{UTS}), both defined along the e_1 direction of the sample. These specific property

combinations are of interest in developing high strength high-toughness alloys for structural applications. Also, in metal forming operations, uniform ductility (e_u) is given special importance because it reflects workability of the metal. The textures predicted to exhibit superior combinations of ultimate tensile strength and uniform ductility lie on the B-H and A-G boundaries of the closures shown in Fig. 31. Different points on these boundaries provide different trade-offs in the achievable combinations of ultimate tensile strength and uniform ductility in the two alloys studies. The main component in textures G and H is close to $(110)[\bar{1}\bar{1}0]$ orientation, whereas the textures A and B have already been discussed (see Fig. 26). Although textures G and H appear to be similar to the textures C and D discussed earlier (corresponding to the lowest values of σ_{y1}/σ_{UTS} in Fig. 26), there are indeed significant differences between these textures. In order to illustrate these differences, the property combinations corresponding to texture C are also shown on the closure for OFHC Copper in Fig. 28. It is clearly observed that the property combinations exhibited by textures C and G are substantially different from each other.

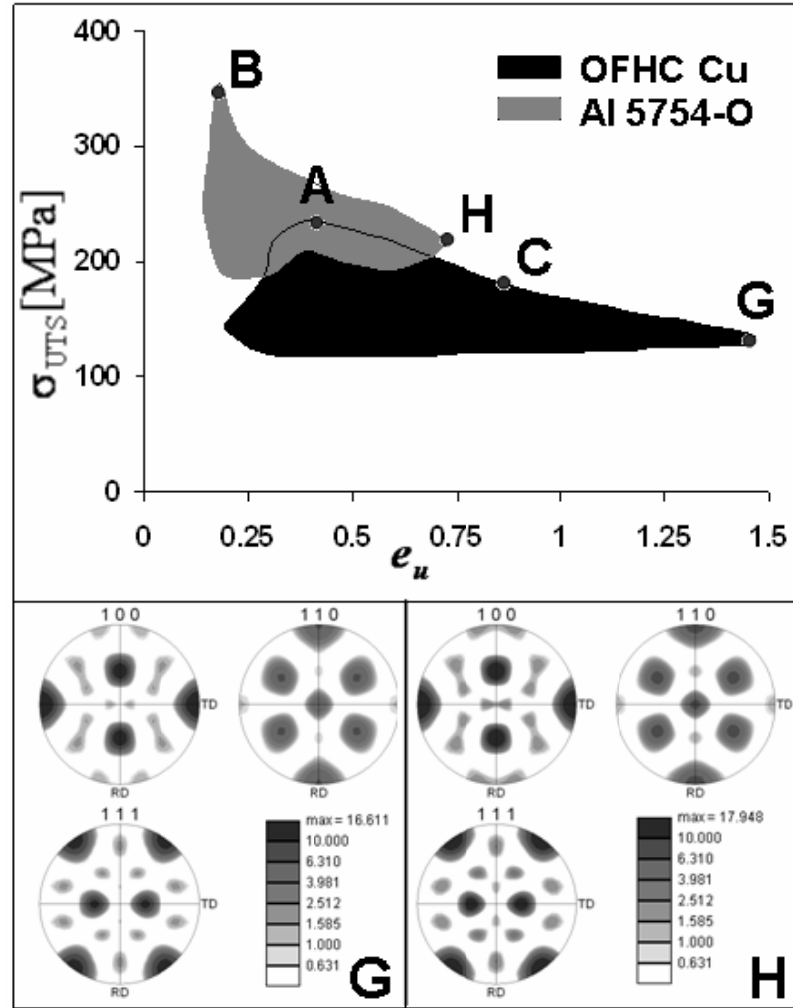


Figure 28 Closure for the uniform ductility (e_u) and ultimate tensile strength (σ_{UTS}) in two cubic metals based on Taylor-type models, and a consideration of all theoretically possible textures (i.e. the elements of the texture hull). The textures that are theoretically predicted to correspond to salient points of interest on the boundary are depicted.

As a final illustration of the potential benefits of the mathematical framework presented in this section, we present a different kind of example. Here we consider a closure for properties that are defined at yield, and therefore there is no need to consider the evolution of texture or strain hardening in delineating the closure. In other words, the closure itself could have been obtained using the methods described in the section 4.2 for

any material for which the strain hardening characteristics are known. Figure 29, shows a closure for the R_f -ratio and the yield strength for 5754-O Al that was presented in section 3.6.1. This closure is of interest to the sheet metal forming industry where the goal is to maximize the workability of the material (high R_f -ratios) while keeping the yield strength low. We now explore here a range of processing paths in this closure to examine if the desired combination of properties can be obtained using several different starting textures and a set of readily available deformation processing options. The mathematical framework presented in this paper allows us to very quickly evaluate the evolution of the properties of interest during any imposed deformation path. Here, we have selected three different initial textures and subjected them to two different deformation paths. The initial textures, chosen for this study, include a random texture, a (110) fiber texture, and a (100)[001] cube texture, shown as J, K, and L, respectively in the Fig. 32. These textures were subjected to plane-strain rolling and simple compression deformation. The evolution of the properties of interest during the selected deformation processes is depicted in Fig. 29. It is observed that none of the combinations of initial textures and deformation paths selected produced a substantial increase in the R_f value. The texture that is theoretically predicted to produce a high value of R_f is shown as texture I in Fig. 29. This dominant component in this desired texture is $(221)[\bar{1}\bar{1}0]$, and is not seen as a major texture component in any of the deformation processing operations typically used by the metal working industry.

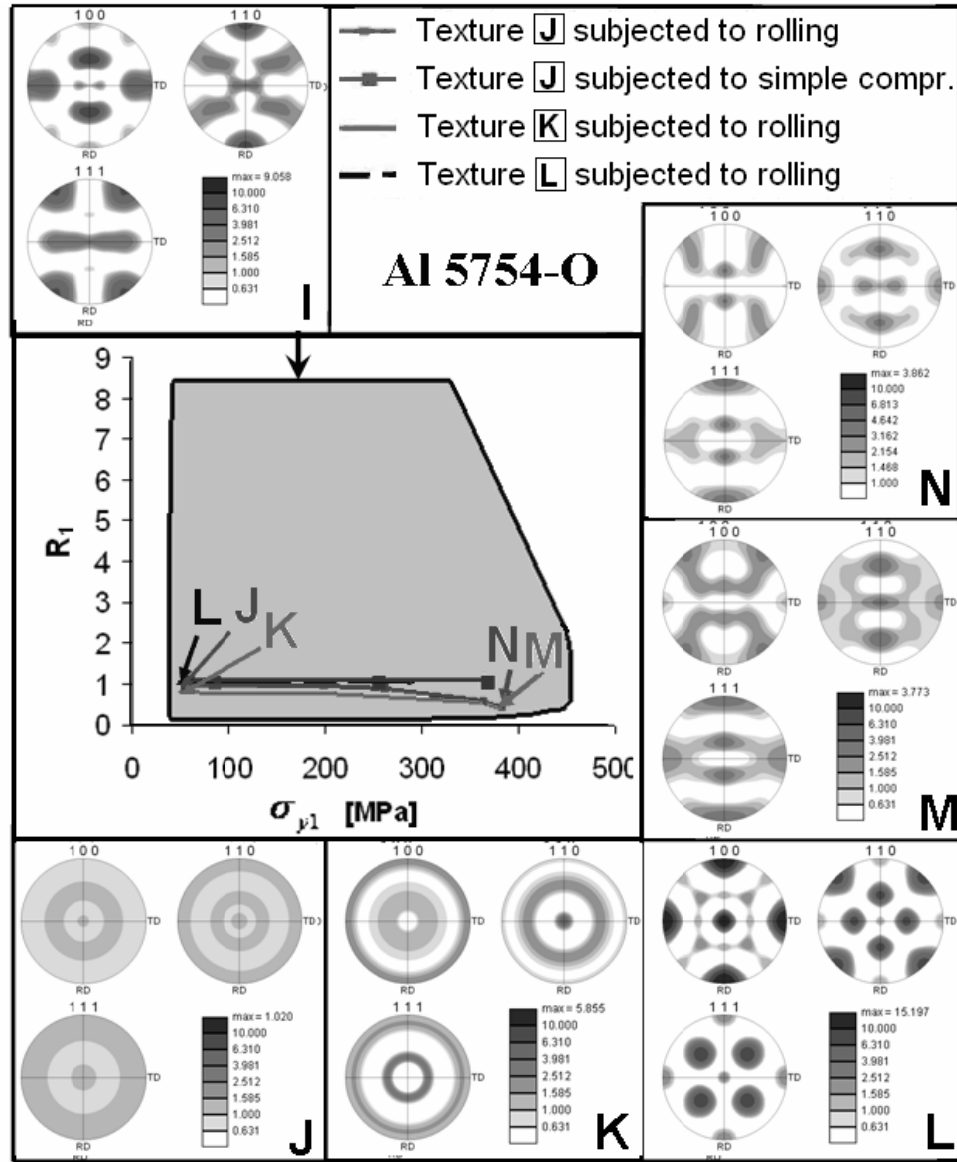


Figure 29 Closure for the R_f -ratio and the yield strength (σ_{y1}) in 5754-O Al based on Taylor-type model for all theoretically possible textures. The desired texture is I. The evolution of textures and properties in typical deformation processes are also shown for three initial textures. These processes do not transform the properties in the desired direction.

All of the examples presented here have highlighted the need and potential for the development of novel processing routes resulting in superior combinations of properties.

3.7. Texture Evolution Networks for Deformation Processing

Any change in texture caused by an imposed deformation process on a sample can be visualized as a “pathline” in the texture hull. The texture evolution networks are essentially made of these pathlines corresponding to different deformation processes. The spectral crystal plasticity methods described earlier are the basis for the fast computation of deformation process paths. The computed pathlines are stored compactly in terms of the Fourier coefficients of the evolving ODF. Every point in the network represents a physically realizable texture whose processing history is fully documented. Therefore, it should be possible to identify a processing recipe to move from any point in the network to another point in the network.

Procedures for building a texture evolution network is an ongoing research work of Joshua Shaffer in our research group and details will be described in his thesis. In the next two sections of this thesis, we demonstrate the potential benefits of the texture evolution networks by considering specific case studies. In the first example, we explored the texture evolution networks to find processing recipes for maximization of the single R -value. In the second example, we explored the networks to find processing recipes for textures that would maximize two in-plane R -values simultaneously. The later is likely to be more meaningful for enhancing workability of sheet metal products.

The imposition of orthorhombic symmetry in the sample reference frame restricts the process design space here to include only the following processes: (i) the complete set of non-zero stretching tensors, \mathbf{D} , whose principle frames are aligned with the sample reference frame, together with zero applied spin tensors, and (ii) 90 degree rotation of the sample about any of the sample reference axes, together with zero stretching tensors. It is

important to note that the process networks are not directly aimed at transforming any given texture into a specific desired texture. Instead, the objective of the process network is to guide us in finding a processing recipe that will transform a given initial texture into one that will exhibit a desired combination of macroscale plastic properties.

3.7.1. Maximizing R_1

In prior sections, we have demonstrated the construction of first-order property closures based on the Taylor-type crystal plasticity models and a rigorous consideration of relevant subspace of the texture hulls. In other words, the property closures are essentially projections of the texture hull into a desired property space.

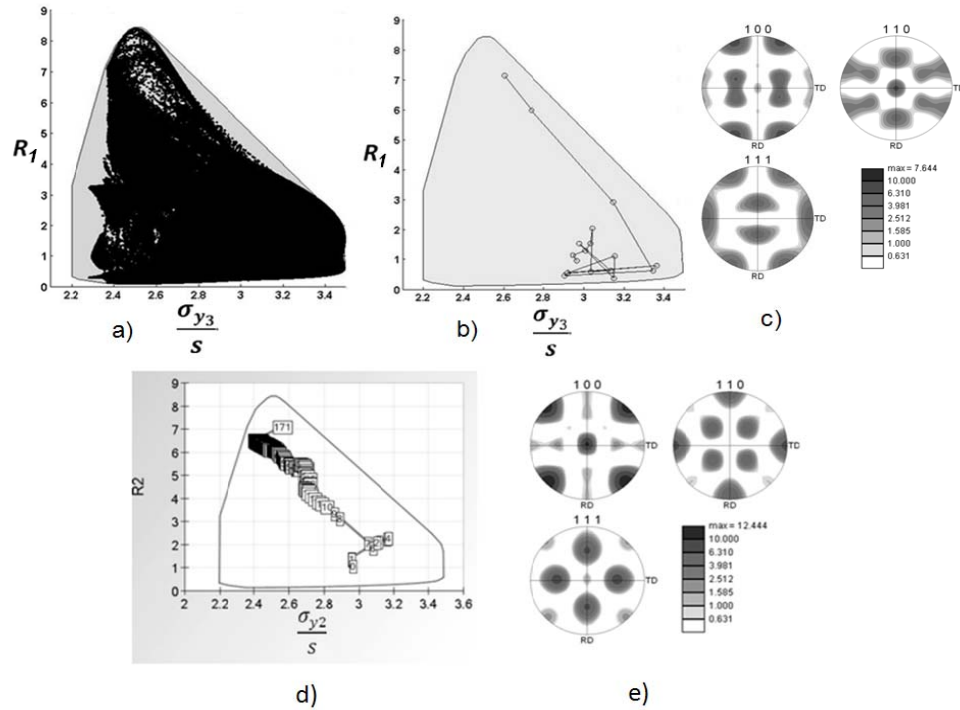


Figure 30 (a) Projection of the texture evolution network onto the (R_1, σ_{y1}) property closure. (b) Identification of a processing recipe to produce high values of R_1 . (c) Texture obtained at the end of 18 processing operation. (d) Processing recipe identified by a brute-force constant performance maximization scheme. (e) The final texture obtained at the end of 171 processing steps.

Figures 30(a) and 30(b) present a property closure for (R_1, σ_{y1}) computed using the spectral database presented earlier as a gray-shaded region. It was noted earlier that a Goss-like texture would produce a high R -value in fcc metals. The texture evolution network is projected into this closure in Figure 30(a). It can be seen that the texture evolution network covers most, but not all, of the property network. Recognizing that every point in this network has a known processing history allows us to find suitable processing recipes for any selected property combination in this closure. A search of points corresponding to the high R_1 values identified the processing recipe depicted in Figure 30(b) comprising 18 different processing steps. The final texture does indeed exhibit a strong two Goss-like component as shown in Figure 30(c).

It is indeed very interesting to note that the processing recipe identified is not one that consistently improves the value of R_1 with each processing step. It is interesting to note that we need several short processing steps initially (some of which actually reduce the values of R_1), before the texture starts evolving towards the desired Goss-like component. In fact, if we addressed the above process design problem simply by searching for processes that produced the largest increase in the value of R_1 in each processing step, we found that we needed about 171 processing steps to reach a comparably high value of R_2 (see Fig. 30 (e)). The texture evolution networks are able to capture and exploit the many complex peculiarities in the texture evolution caused by deformation processes and identify a better processing recipe with only 18 processing steps (Fig. 30(b)). It should also be noted that it would be very difficult, if not impossible, to arrive at this processing solution purely intuitively (or using repeated trials).

The above example also highlights one of the main advantages of texture evolution networks. Since the texture evolution network is built in the texture hull, it can be projected into any property space of interest. However, if the texture evolution network was actually built directly in the property space, it would only be applicable to that specific property space.

3.7.2. Maximizing R_1 and R_2

In many sheet forming applications, it is important to achieve high values of in-plane R -values. Therefore, as the next case study, we explore processing recipes that would enhance both R_1 and R_2 . The same texture evolution network that was used earlier was projected into this closure and several of the points in the region of interest were explored.

Figure 31 show the property closure for (R_1, R_2) obtained using the methods from earlier chapters. It appears from the closures in Fig. 32 that it is only possible to achieve maximum values of about 5 simultaneously for both these parameters (based on the simplified Taylor-type model in this study). The processing paths shown in Fig. 36 were identified as the ones that achieved high values of both R_1 and R_2 in the minimal 7 and 9 number of processing steps, respectively. The starting point was a random texture.

This processing solution probably could not have been produced purely intuitively or by repeated trials.

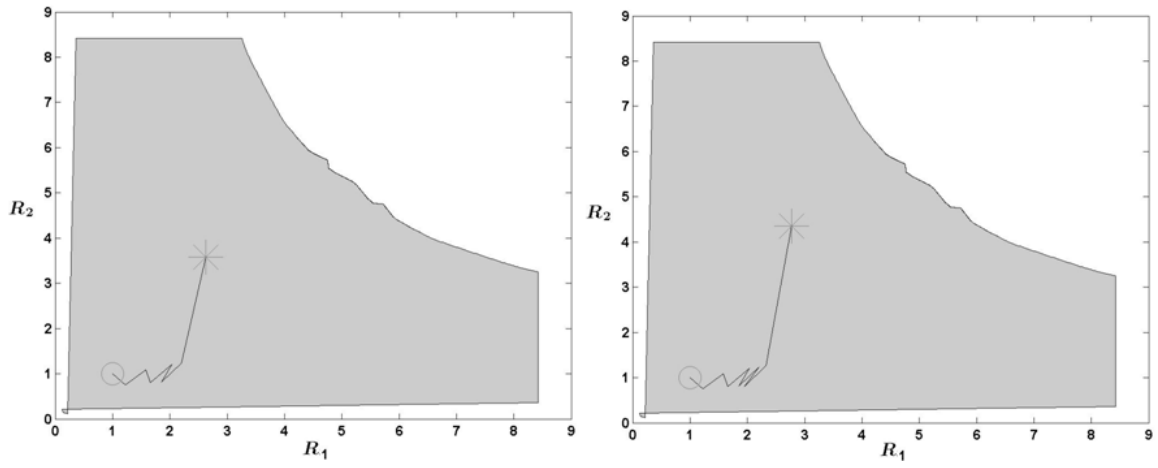


Figure 31 Processing recipes identified using the texture evolution network for enhancing both R_1 and R_2 obtained at the end of 7 and 9 processing steps, respectively.

CHAPTER 4: DEFORMATION TWINNING IN AZ31 Mg ALLOY

This chapter describes the experiments and simulations conducted in this Ph.D. thesis on AZ31 to understand the deformation twinning in this alloy system. These insights and observations are the key to the future extension of crystal plasticity models to Mg alloys.

4.1. Mechanical Testing and Metallography

The composition of the commercial magnesium alloy AZ31 used in this study is 3.1 wt.% Al, 1.05 wt.% Zn, 0.0035 wt.% Fe, 0.007 wt.% Ni, 0.008 wt.% Cu, and Mg balance. This alloy was reported to exhibit a Young's modulus of 45GPa and a shear modulus of 17GPa. Cylindrical samples for simple compression tests were machined from an annealed (O-temper) 3.2mm thickness sheet. The annealed sheet showed a strong fiber texture with most of the basal planes aligned parallel to the RD-TD plane (see the pole figures in Fig. 32 (a)). The average grain size in the sheet was about 8 micrometers (μm). As shown in Fig. 32(b), compression samples were machined in different orientations and grouped into two sets based on their initial texture with respect to the axis of the cylindrical samples. The axis of the first set of cylindrical samples (labeled as the loading axis LA in Fig. 32(b)) was parallel to the sheet ND direction, which is also parallel to the crystallographic **c**-axis in most of the grains. The axis of the second set of cylindrical samples was perpendicular to the sheet ND, with the crystallographic **c**-axis in most grains perpendicular to the loading axis. Because of the sheet's geometry, the two sets of samples had different initial dimensions: 3.2 mm diameter and 3.2 mm length for

the first set (i.e. ND \parallel LA) and 3.2 mm diameter and 5 mm length for the second set (i.e. TD-RD \parallel LA).

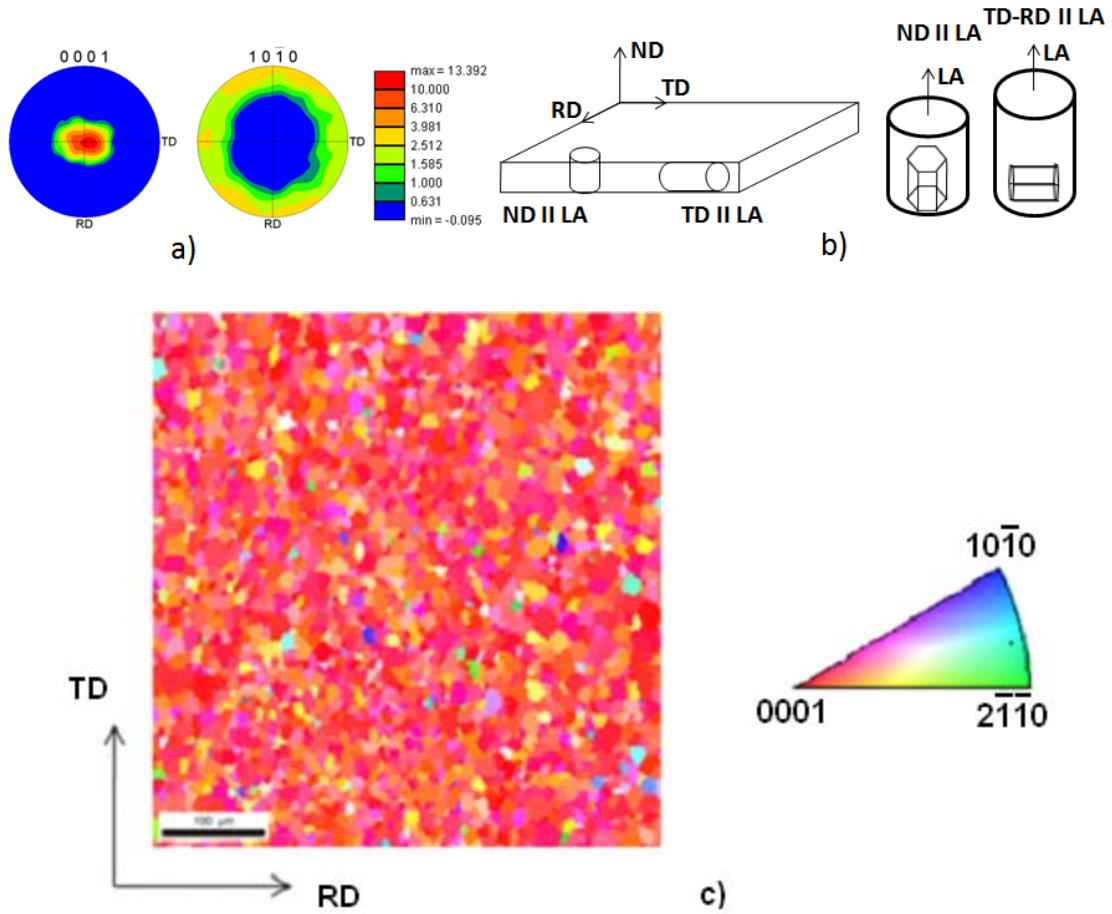


Figure 32 (a) Measured pole figures showing the initial texture in the annealed AZ31 sheet. (b) Schematic showing the orientations of the cylinders used in simple compression tests performed in this study. (c) EBSD inverse pole figure (IPF) map showing orientation of the annealed sheet's ND direction with respect to the local crystal frames, collected in the sheet RD-TD plane. The crystallographic c-axis in most grains is closely aligned with the sample ND direction.

Constant strain rate simple compression tests were performed at a strain rate of 10^{-3} sec^{-1} at room temperature using a screw-driven INSTRON 58R1127. Teflon sheets were used between the sample and compression surfaces to reduce frictional effects. The tests were interrupted frequently to change the Teflon sheets, typically after true strain

increments of about -0.1. The raw data was collected in the form of load and displacement, and was corrected for machine compliance [112] before computing the true stress-true strain curves. The ND || LA samples were deformed to true strains of 0.012, 0.065, 0.075, 0.13 and 0.26, whereas the TD-RD || LA samples were deformed to true strains of 0.01, 0.025, 0.04, 0.05, 0.06, 0.08, and 0.2. The highest strain levels mentioned for each set corresponded to the strain levels where the samples typically failed by shear. The later set of samples required more strain steps because of more dramatic changes in the microstructure.

All samples were prepared for orientation imaging microscopy (OIM) by sectioning parallel to the loading direction. The samples were mechanically polished on Buehler PowerPro 4000 Specimen Preparation System using a sequence of oil-based diamond suspensions of 9, 3, and 1 μm , respectively. This was then followed by fine-polishing using 1 part 0.02 micron colloidal silica, 1 part ethanol, and 1 part ethylene glycol. A final 2-4 seconds etch using a solution of 60mL ethanol, 20mL distilled water, 15mL acetic acid, and 5mL nitric acid was helpful in improving quality of the electron backscatter diffraction (EBSD) patterns. The EBSD data was collected using a Orientation Image Mapping (OIM) system [113] attached to a FEI XL30 ESEM at a voltage of 20KV.

To complement the compression tests, a set of tensile tests were conducted by our collaborators at General Motors Research, Warren, MI. The tensile data were collected on the same material in the same condition.

4.2. Results

The stress-strain curves measured on different samples in each group (at least three samples were tested in each group) were found to exhibit very little variance (less than 4 %). Figure 33(a) shows representative true stress-true strain response of annealed AZ31 sheet measured in simple compression in the two mutually perpendicular directions described earlier (see Fig. 33 (b)). A comparison of the two stress-strain curves in Fig. 33(a) indicates significant anisotropy in the plastic response of the AZ31 sheet. It can be seen that the yield stress is about 150 MPa in the ND samples whereas it is about 115 MPa in the TD-RD samples. The associated strain hardening behaviors shown in Fig. 33(b) also indicate a major difference. The strain hardening rates plotted in Fig. 33(b) are computed numerically from the stress-strain curves shown in Fig. 33(a), and were normalized by the shear modulus to facilitate comparisons with published data on other hexagonal metals [76,77,114].

The strain hardening curves for both the ND and the TD-RD samples show distinct regimes that are reminiscent of those seen previously in both fcc and hcp metals that exhibit deformation twinning [73,76,77,114-117]. In the TD-RD samples, the strain hardening response shows three distinct regimes. The first regime reveals a steadily falling strain hardening rate that can be attributed to dynamic recovery. At the end of this first regime, the strain hardening rate almost drops to zero. This dynamic recovery stage is then followed by a second regime of sharply increasing strain hardening rate. This second regime is then followed by the final regime of falling strain hardening rate. In the ND sample, although the same three strain hardening regimes are seen, the second regime of increasing strain hardening rate is significantly less pronounced. The presence of these

distinct regimes of strain hardening and their similarity to those observed previously in low stacking fault energy fcc metals [73,115-117] and α -Ti [76,77,114] suggests the dominance of deformation twinning in both sets of samples. The differences in the strain hardening responses between the two sets of samples should be attributable to the different initial textures, which in turn can lead to major differences in the type and extent of the deformation twins produced in these samples.

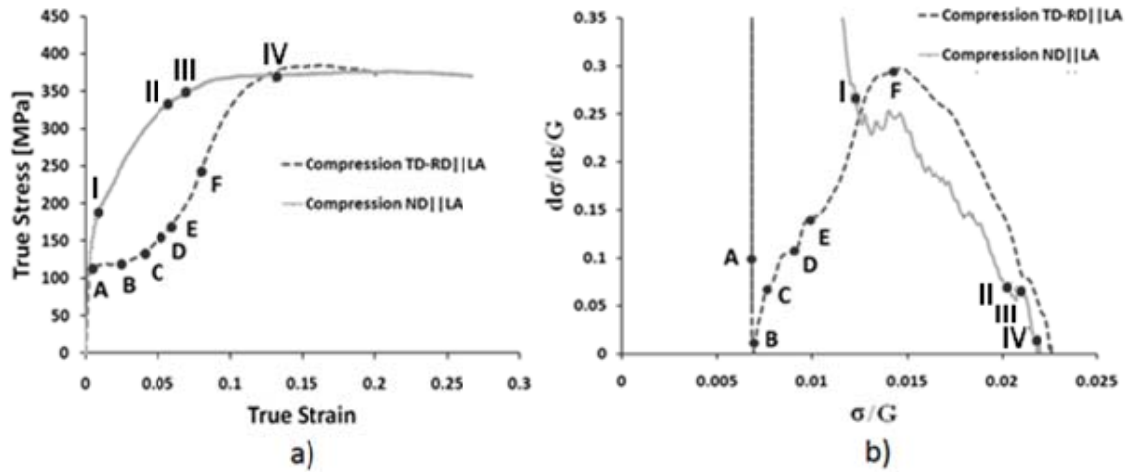


Figure 33 Simple compression tests at room temperature on an annealed sheet of AZ31: (a) true stress-true strain responses, (b) normalized strain hardening responses. The various points labeled indicate locations where microstructure investigations were conducted using OIM.

Microstructure evolution was investigated by orientation imaging microscopy (OIM) in both sets of the samples compressed to several strain levels. The tests performed on the set of TD-RD samples were interrupted at the locations indicated by A to F in the Fig. 33(a). Figure 34 and Figure 35 show the inverse pole figure maps and the pole figures, respectively, for the TD-RD samples deformed to true strain levels ranging

from -0.01 to -0.08. The inverse pole figure maps are collected on the longitudinal section of the compressed samples and reflect the orientation of the loading axis (LA) with respect to the crystal reference frame.

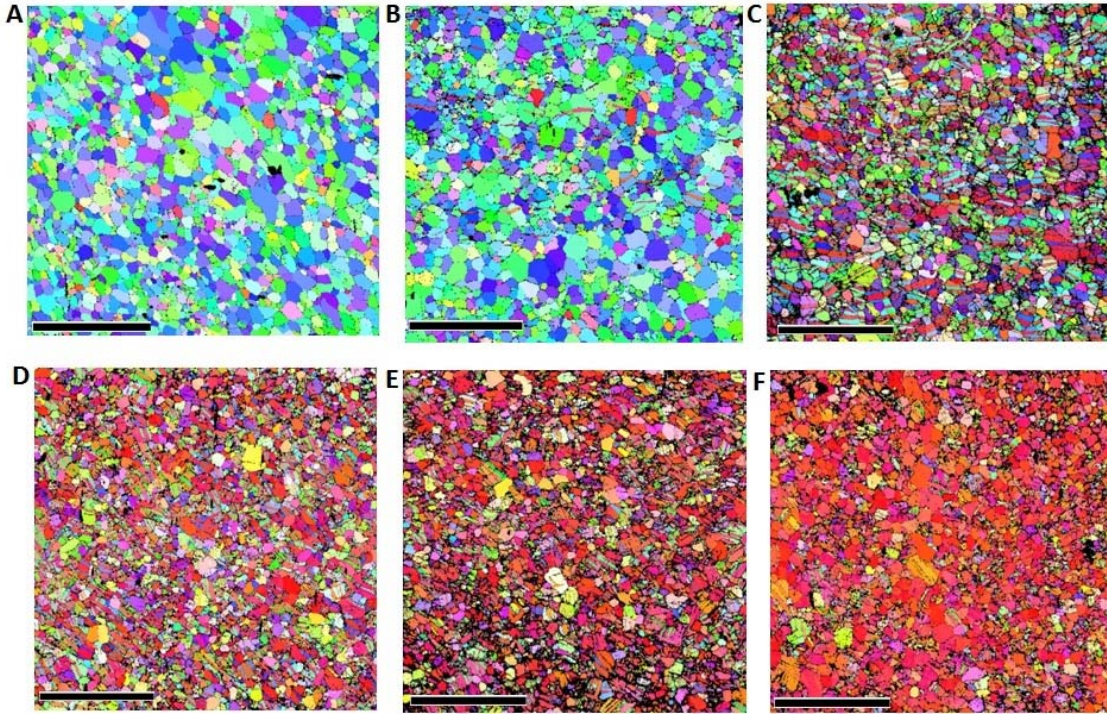


Figure 34 Inverse pole figure (IPF) maps showing microstructure evolution of the TD-RD compressed AZ31 samples to true strain levels of (A) 0.01, (B) 0.025, (C) 0.04, (D) 0.05, (E) 0.06, and (F) 0.08. These maps indicate the orientation of the compression axis with respect to the crystal reference frame. The marker shown in these maps corresponds to a length of 100 microns. The color-legend is the same as in Fig. 32(c).

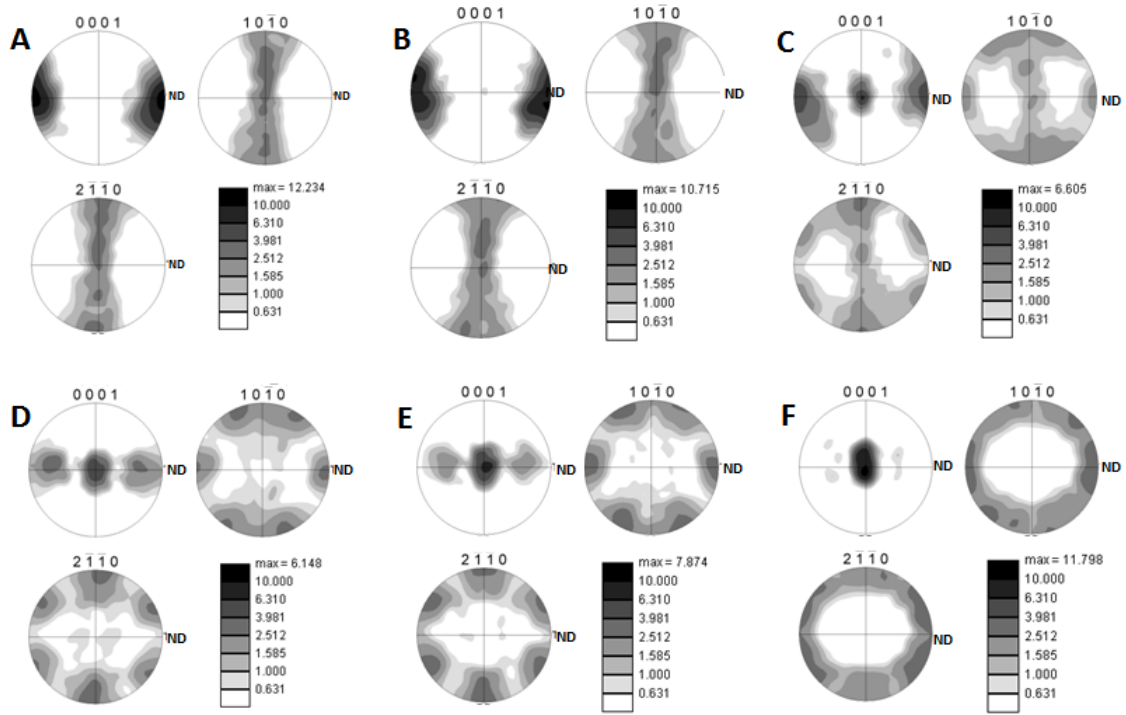


Figure 35 Pole figures showing texture evolution in the TD-RD compressed AZ31 samples to true strains of: (A) 0.01, (B) 0.025, (C) 0.04, (D) 0.05, (E) 0.06, and (F) 0.08. The compression axis lies at the center of all the pole figures shown here.

The microstructure at point A shown in Fig. 34, corresponding to a true strain of -0.01, is barely different from that shown in Fig. 32(c) for the initial microstructure. The inverse pole figure maps in Fig. 32(c) and Fig 34(a) show very different colors because the map in Fig. 32(c) shows the sample ND direction, while the map in Fig. 34 shows the compression direction in the TD-RD samples. However, when seen in the same projection there is no noticeable difference in these two microstructures. More importantly, at this strain level, there is no evidence of deformation twinning in the sample. At point B, corresponding to a true strain of -0.025, we observed the first evidence of deformation twins, which appeared as plate-like structures within individual grains as seen in Fig. 34. Since most of the grains were initially oriented with their *c*-axis

perpendicular to the LA, re-orientation by extension twinning brings the **c**-axis parallel to the LA. Consequently, the twinned regions appear red in the IPF maps shown in Fig. 34. The lattice inside these plate-like structures was re-oriented with respect to the parent matrix by the expected 86.3° about the $\langle 11\bar{2}0 \rangle$ directions, suggesting that these are extension twins. The extension twin boundaries are shown as thicker boundaries in Fig. 36 for the deformed sample at point C, where they are much more abundant than at point B. With increased strain levels, the extension twins appear to grow fast and quickly encompass the entire grain, consistent with previous observations [64,65].

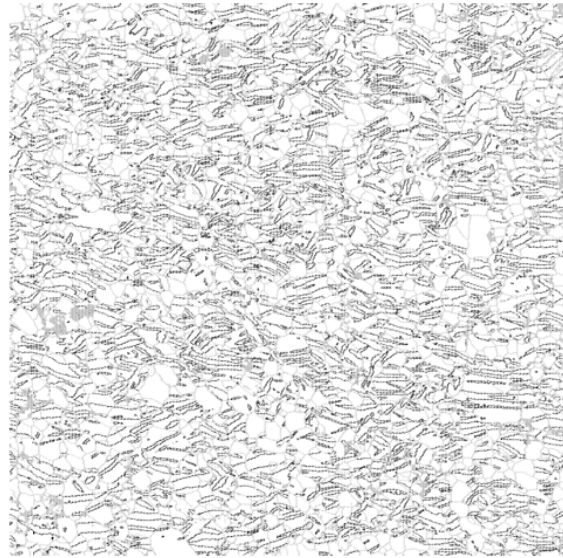


Figure 36 Extension twin boundaries identified in the OIM maps based on the expected mis-orientation in the TD-RD compressed sample interrupted at point (C) at a true strain of -0.04.

Extension twins are seen to play a dominant role in the texture evolution in the early stages of the simple compression of the TD-RD samples. As expected, the grains with their crystallographic **c**-axis normal to the loading axis are the ones that produce the first extension twins. This is clearly seen in the evolution of the pole figures shown in

Fig. 35, where the poles on the circumference are the ones that disappear first and re-appear at the center of the pole figure. It is important to note that the shear strain of 0.1289 associated with extension twinning corresponds to a maximum axial strain of about 0.065. It is therefore quite reasonable to expect the exhaustion of extension twinning mechanism in the TD-RD samples after a small amount of axial plastic strain. Indeed, the dramatic changes in texture occurred over this very small strain range as shown clearly in the pole figures presented in Fig. 35. In fact the texture after a true strain of about -0.06 in the TD-RD plane is essentially a $\{0001\}$ -fiber texture that is remarkably similar to the initial texture in the as-annealed ND sample (see Fig. 32(a)). Not surprisingly, the stress-strain curves for these two groups of samples shown in Fig. 33 look very similar after this small amount of strain in the TD-RD samples.

In order to quantify the extent of extension twinning, we have plotted in Fig. 37 the volume fraction of the material with crystallographic **c**-axis oriented within 20 degrees of the LA as a function of the imposed plastic strain on the TD-RD samples. The plot in Fig. 37 corresponds only to very small plastic strains. It should be noted that the small amounts of crystallographic slip that are expected to occur during these very small plastic strains are inadequate to re-orient grains in the TD-RD samples from their initial orientations (with **c**-axis about 90 degrees to LA) to the orientations counted in Fig. 37 (with **c**-axis within 20 degrees of LA). It should also be noted that the initial texture in the TD-RD samples shows a very low volume fraction of grains with the **c**-axis within 20 degrees of the LA (see Fig. 32(c)). It is therefore assumed here that much, if not all, of the material in these orientations is a consequence of re-orientation by extension twinning.

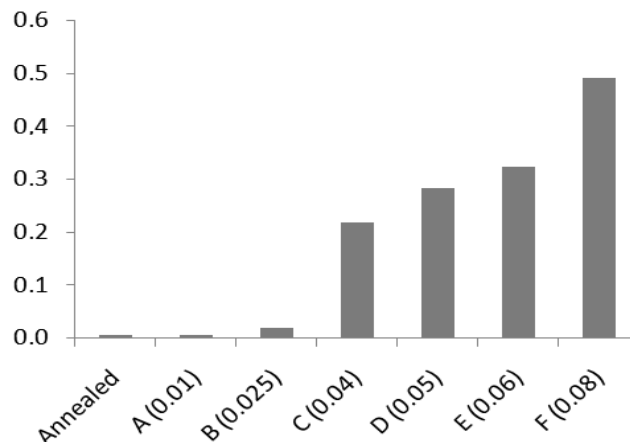


Figure 37 Volume fraction of material with crystallographic **c**-axis oriented within 20 degrees of the compression direction in the TD-RD samples. The compressed samples are labeled A to F with corresponding strain level indicated in the brackets.

Beyond a true strain of -0.08 there were no noticeable differences either in the pole figures or in the IPF maps of the TD-RD compressed samples. It is however seen that these additional plastic strains are associated with unusually high strain hardening rates, as high as 0.3G (G is the shear modulus of the material). It should be noted that the texture in these samples at this strain level is such that plastic strain can only be accommodated either by contraction twins or by the 2nd pyramidal $\langle c+a \rangle$ slip. The only hint of the activation of contraction twins was found in the image quality maps where a number of dark bands (signifying low image quality) were seen cutting across grains. However, the confidence index on the orientation measurements inside these thin bands was extremely low. This is to be expected, because it has been shown that contraction twins in Mg alloys often lead to “double-twins” with the formation of extension twins inside the contraction twins [62-64,66-72]. The dislocation structure inside these double twins is very complex and is very likely to preclude the formation of clearly indexable EBSD patterns.

Now we turn our attention on a set of samples deformed in the ND direction. The ND compressed samples provided OIM maps with slightly improved confidence index than the TD-RD samples compressed at strains larger than -0.08. The tests performed on a set of ND samples were stopped at the true strains indicated by I, II, III, and IV in the Fig. 33. Figure 38 shows the inverse pole figure maps and an image quality map collected on the longitudinal section and the corresponding pole figures of the ND samples deformed to a true strain of -0.012 and -0.065. The dominant operative deformation mechanisms in this set of samples could be the pyramidal $\langle c+a \rangle$ slip or the contraction twinning. Pyramidal $\langle c+a \rangle$ slip has substantially larger slip vector compared to $\langle a \rangle$ slip and thus, a markedly higher CRSS. It has also been argued that the pyramidal slip in magnesium requires thermal activation [55-57]. The dark bands seen in individual grains in the image quality map are believed to be contraction twins or double twins.

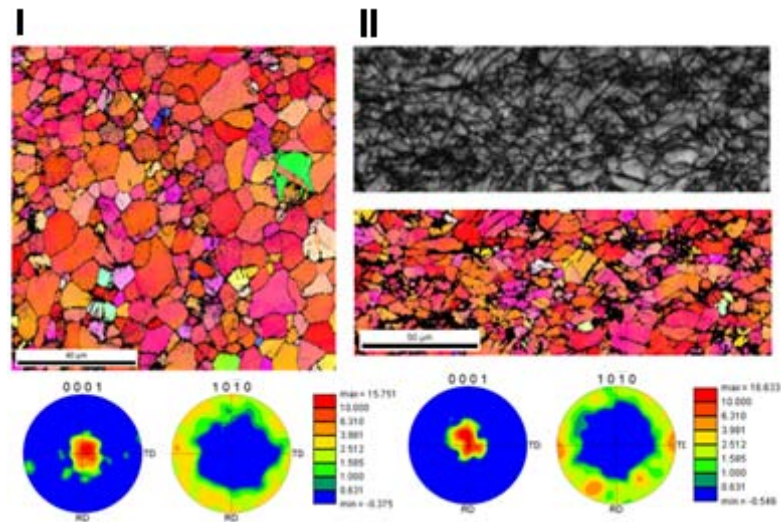


Figure 38 Inverse pole figure (IPF) maps showing microstructure evolution of the ND compressed AZ31 samples to true strain levels of (I) 0.012 and (II) 0.065. These maps indicate the orientation of the compression axis with respect to the crystal reference frame. The color-legend is the same as in Fig. 32(c). Image quality map at II shows high concentration of twin like bands; we believe that these bands represent the contraction twin bands.

Since the twinning shears associated with extension and contractions twins are such that they roughly correspond to a maximum axial strain of about 0.065 when the volume fraction of twinning is nearly 100%, it is clear that a significant portion of the plastic strain in this sample has been accommodated by other mechanisms. Given the texture in this sample, it is most likely that the 2nd pyramidal $\langle c+a \rangle$ slip is the other dominant deformation mechanism in this sample. It was seen that the texture did not alter noticeably from the initial texture in the sample. This once again indicates that the volume fraction of the material occupied by the deformation twins in the ND compressed samples is quite small.

Figure 39(a) shows a comparison of the measured true stress-true strain responses in simple compression and simple tension tests in the TD direction. A significant asymmetry is noted in the measured compressive and tensile yield strengths, which are estimated to be 115 MPa and 160 MPa from Fig. 39(a). The difference in the strain hardening behavior in these two deformation modes is clearly evident from Fig. 39(b). We have observed earlier that compression along TD produced extension twins in the sample (see Figures 34 and 35). In tensile loading along TD, we expect the formation of contraction twins in at least some of the crystals. It has been speculated in literature that the tension-compression asymmetry observed in Mg alloys is due to the activation of different slip/twin systems (i.e. extension and contraction twins) in the two different modes of deformation [64,118]. However, a closer look at the yield phenomenon in the two tests indicates that the apparent differences in the yield points are much more a consequence of the different hardening responses in these two tests. Figure 39(c) shows an expanded view of the comparison between the measured stress-strain curves shown in

Fig. 39(a) in the vicinity of yielding. It is clear from Fig. 39(c) that there is no asymmetry in the tension-compression yield points in Fig. 39(a) when the material begins to deform nonlinearly following the elastic deformation. The engineering yield strength difference is due to stark differences in the strain hardening rates, immediately following the onset of plastic deformation in the two deformation modes. Recall that the simple compression of the TD-RD samples produced extension twins at low strains and the corresponding strain hardening rates were relatively low. However, simple tension in the TD-RD samples should be expected to activate contraction twins and the 2nd pyramidal $\langle c+a \rangle$ slip that have been associated with high strain hardening rates (somewhat similar to the observations in simple compression of the ND samples).

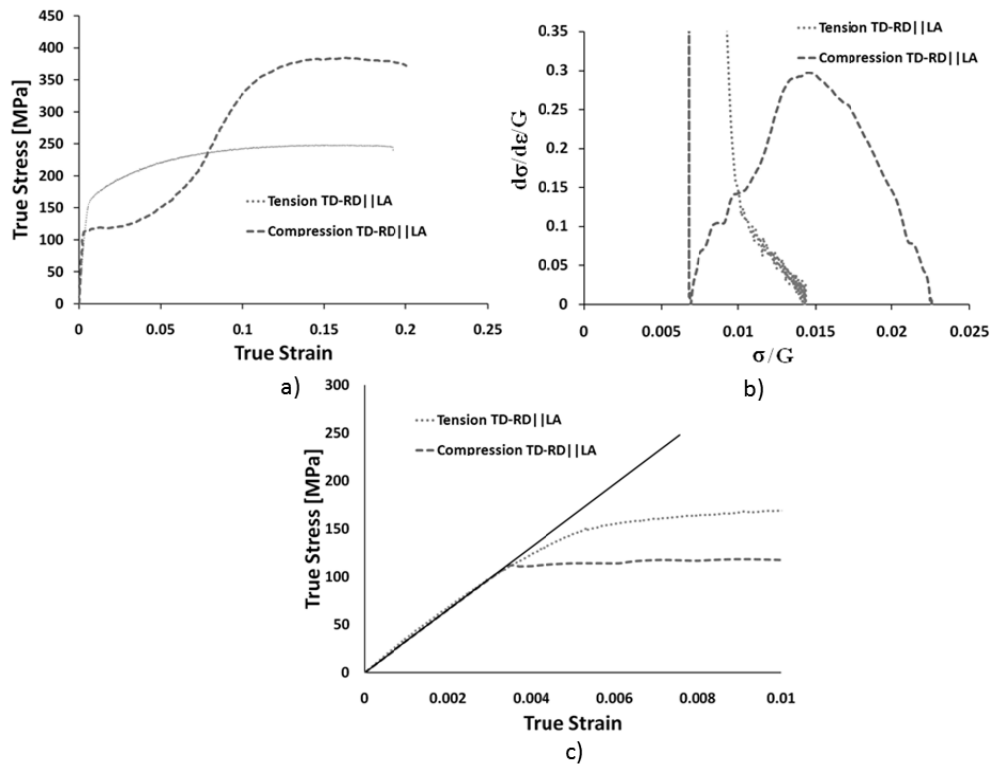


Figure 39 Mechanical response of annealed AZ31 tested in simple compression and simple tension at room temperature and a constant strain rate of 10^{-3} s^{-1} along TD direction: a) true stress-true strain responses, b) normalized strain hardening responses, c) expanded view of the yield response shown in (a).

4.3. Discussion

The microstructure evolution and stress-strain responses measured in TD-RD compressed and ND compressed AZ31 samples showed major differences only in the early stages of deformation (see Fig. 33). Although there was a major difference in the starting textures in these samples, the texture in TD-RD after a true strain of about -0.06 was essentially identical to the starting texture in the ND samples. This abrupt change in the underlying texture can only be explained by profuse extension twinning in the sample. After the low strains in the TD-RD samples where this texture transformation takes place, the flow stress, the strain hardening rates, and the underlying microstructures in both sets of samples tested were remarkably similar.

In previous studies on fcc and hcp metals, it was observed that deformation twinning produced significant strain hardening by two primary mechanisms: (i) a reduction of slip length due to grain refinement by production of twins, and (ii) a glissile to sessile transformation of the pre-existing dislocations in the twinned regions as a result of the twinning shear transformation. However, the extension twins observed in AZ31 studied here did not produce the expected high strain hardening rates. This can be explained by recognizing that the extension twins in AZ31 often grew rapidly to encompass the entire grain, and therefore did not alter significantly the available slip length. Furthermore, the extension twins appeared very early in the deformation process before the accumulation of any significant dislocation density in the sample. Consequently, we observe that extension twinning in AZ31 produced a modest amount of plastic strain (about 6.5% axial strain) without appreciable strain hardening in the sample.

On the other hand, other deformation regimes in the tests have been associated with unusually high strain hardening rates that appear to correlate with the possible activation of both contraction twins and 2nd pyramidal $\langle c+a \rangle$ slip. These high strain hardening rates not only impart significant anisotropy in the mechanical response of AZ31, but also induce an apparent asymmetry in the tension-compression yield values. The normalized stress-strain curves and strain-hardening rates in AZ31 measured here are compared to corresponding results reported previously for α -Ti [76,77,114] in Fig. 40. It is important to note that the α -Ti sample was also annealed and exhibited a strong c-axis fiber texture at the start of the compression. The normalization in Fig. 40 was performed using the respective shear moduli of both materials, after subtracting the respective initial yield values from the flow stresses to filter out the effects of solid solution, impurities, and grain-size.

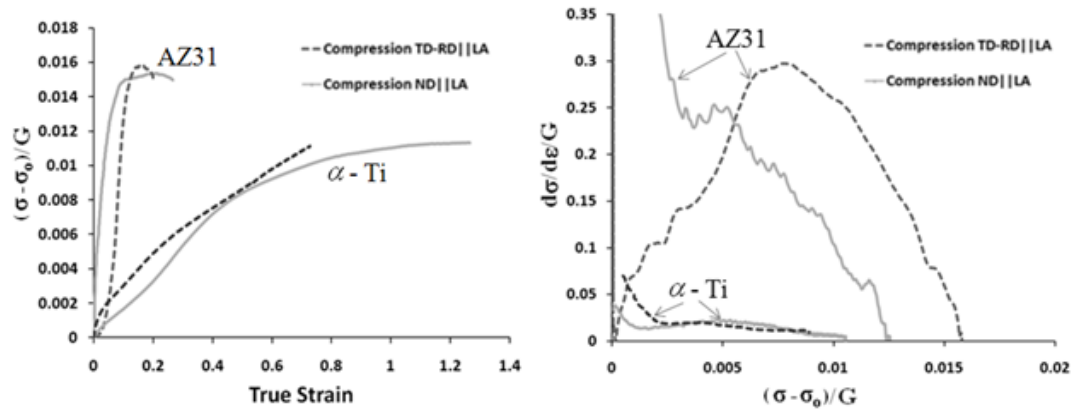


Figure 40 A comparisons of the normalized true stress-true strain responses and normalized strain hardening rates during simple compression of α -Ti and AZ31 with similar initial textures.

The comparison in Fig. 40 clearly demonstrates that the strain hardening rates in AZ31 for the most part (except for the deformation regimes involving extension twins) are significantly higher than in α -Ti. As a consequence of these high strain hardening

rates, the flow stresses increase sharply after only a small amount of plastic strain. The relatively high stress levels may be responsible for initiation of various damage mechanisms and the limited ductility exhibited by these samples. In this regard, it is also interesting to note that the peak stresses reached by both the ND and TD-RD compressed samples before final failures are quite similar.

It is well known that the increase in flow stress corresponds approximately to $Gb\sqrt{\rho}$, where b denotes the magnitude of the Burgers vector and ρ is the dislocation density. Based on this relationship, we estimate the dislocation density in our samples at the highest flow stress levels to reach $22 \times 10^{12} \text{ m}^{-2}$, which is consistent with measurements summarized in [119] for similar samples by more reliable techniques. Furthermore, the plastic strain increment is expected to be proportional to $\rho b L$ where L is the corresponding average slip distance in that plastic strain increment. For the samples tested in this study, it is estimated that the average slip distance at the highest strain hardening rates measured was of the order of $1.2 \text{ }\mu\text{m}$ (note that average grain size in our starting material was about $8 \text{ }\mu\text{m}$). This reduction in slip length could be a consequence of two factors: (i) formation of families of very thin contraction twins, and (ii) difficulties in activation of non-basal slip. Clearly, there is a critical need for high resolution OIM and TEM studies to establish precisely the physical origin of these unusually high hardening rates.

The discussion above leads us to conclude that an important factor controlling the ductility of AZ31 is the production of thin contraction twins. The very thin morphology of these contraction twins suggests that they are unable to grow significantly, whereas the extension twins are able to grow quickly and encompass the entire grain in many cases.

In order to obtain a better understanding of the process of deformation twin formation and growth, let us follow carefully the sequence of changes occurring in the sample. A deformation twin presumably appears in a grain when the stress conditions are such that the formation of the twin is preferable compared to the other possible alternatives (including slip and other twin systems). If we assume that the driving force for the activation of a slip or a twin system is the resolved shear stress (τ^α) on that specific system and that there is a critical value of the slip or twin resistance (τ_c^α), then it is reasonable to postulate that the ratio $\tau^\alpha/\tau_c^\alpha$ controls which slip or twin system gets activated in a given grain subjected to a given loading condition. Let us now focus on a grain that is favorably oriented and stressed for the formation of a selected twin system (i.e. $\tau^\alpha/\tau_c^\alpha$ is the highest in this grain for the selected twin system compared to all other possible deformation modes). However, as soon as a deformation twin is nucleated, it alters significantly the stress field inside the region now occupied by the twin as well as the neighboring matrix regions. As a consequence, the values of $\tau^\alpha/\tau_c^\alpha$ for the different possible deformation modes will change significantly both inside the twin as well as in the neighboring matrix regions. If the value of $\tau^\alpha/\tau_c^\alpha$ continues to be the highest for the activation of the same deformation twin system in the matrix regions (as it was before the formation of the deformation twin), then the existing twin can grow unimpeded or other deformation twins of the same family can nucleate in matrix and coalesce with the existing ones, leading to a thickening of the deformation twin. However, if the production of a deformation twin alters the stress field such that other deformation modes are favored either inside the twinned region or in the adjacent matrix regions, it will lead to a

significant heterogeneity in the deformation modes inside and outside the twin. Any such heterogeneity will lead to a loss of coherency at the twin-matrix boundary, which in turn should arrest the growth of the deformation twin.

The loss of coherency at the twin-matrix boundary was previously documented in transmission-electron microscopy studies in low stacking-fault energy fcc metals [73,115-117]. In fcc metals, where there is an abundance of potential slip and twin systems and the values of slip and twin resistances are relatively close to each other, the formation of a deformation twin is very likely to alter the local stresses adequately to initiate a substantial heterogeneity in the active deformation modes inside and outside the twin. It is therefore, quite reasonable that the deformation twins in fcc metals are very thin [73,115-117]. Conversely, it has been observed that the deformation twins in α -Ti are significantly thicker [76,77,114] and this can be reconciled with the concepts described above by acknowledging the availability of a limited number of slip and twin systems and the significant differences that exist in the values of the slip and twin resistances in this material. Extending these concepts to AZ31, we would have concluded that the deformation twins in AZ31 should be substantially thicker compared to α -Ti because (i) the available slip systems in AZ31 are more restricted, and (ii) the differences in slip and twin resistances are relatively larger. Indeed, the extension twins we observed in this study are very large and often encompass the entire grain in many cases, consistent with the hypotheses laid out above. However, the contraction twins do not seem to follow the same trend.

In an effort to understand the physical origin of the observed differences in the morphologies of the extension and contraction twins, we studied the ensuing changes in

the stress fields due to the formation of a deformation twin using crystal plasticity based finite element models implemented in ABAQUS [5]. A total of four loading conditions were explored. These corresponded to tension and compression along the crystallographic **c**-axis in the matrix, and to tension and compression along a direction normal to the **c**-axis in the matrix. Our studies on these four loading conditions indicated that the results essentially fell into two major groups. The compression along the **c**-axis and tension along a direction normal to the **c**-axis produced qualitatively the same insights, and therefore only the former are presented and discussed here. Likewise, tension along the **c**-axis and compression along a direction normal to the **c**-axis also provided qualitatively similar insights, and once again only the former are presented and discussed in this thesis.

Current implementations of crystal plasticity models in finite element models are not capable of accounting explicitly the crystal lattice re-orientation caused by deformation twinning. Therefore our strategy here is focused on simulating the elastic-plastic stress fields in a twin-matrix composite that would result after the production of the twin variant of interest. This required the development of two different finite element meshes (one for each set of loading conditions described above) containing roughly 12,000 3-D continuum solid elements. These meshes are shown in Fig. 41 and were designed to capture all of the geometric details of the selected twin variant-matrix system. For the compression along the **c**-axis the contraction twin variant produced by the $(0\bar{1}11)[0\bar{1}1\bar{2}]$ twin system was selected as it would be one of the twin systems predicted to be active by the simple Schmid analyses (assuming a uniaxial compressive stress). Similarly, for tension along the **c**-axis the extension twin variant produced by

$(0\bar{1}12)[\bar{1}101]$ twin system was selected here for the analyses. In both meshes, each element was associated with an appropriate initial crystal lattice orientation to reflect the expected lattice orientation dependence between the twin and the matrix. Likewise, we ensured that the twin-matrix boundary coincided with the expected crystallographic habit plane for both the twin and the matrix in each model.

For analyses of the results obtained from the finite element simulations, two specific groups of elements were identified in the finite element mesh to compute the average stresses in the twinned region and the matrix region close to the twin. Only the interior elements were selected in these regions as highlighted in one of the meshes in Fig. 41. The exterior elements were excluded to mitigate any influence of the boundary conditions imposed in the simulation, which corresponded to simple compression and simple tension, respectively.

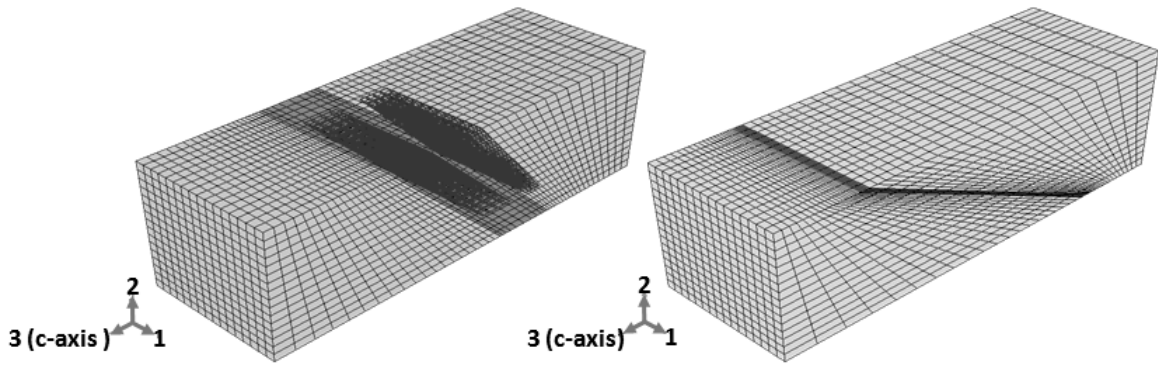


Figure 41 Finite element meshes used in simulating the stress fields in the matrix-twin composite: matrix-extension twin on the left and matrix-contraction twin on the right. The crystallographic **c**-axis in the matrix was selected to be coincident with the loading direction 3 in the FEM models. The elements used for computing average stresses in the twinned region and in the matrix region are highlighted in the mesh shown on the left.

The simulations were performed assuming that the critical resolved shear stresses for the basal, prismatic, pyramidal and twin modes were in the ratio 1:5:6:2 [67]. Note that the extension and contraction twins were assigned the same values of twin resistance and deformation twinning was considered as a pseudo-slip mode (i.e. the lattice re-orientation due to additional deformation twinning was not accounted). Work hardening was not considered and the simulations were only performed up to a strain of 0.004, which was enough to initiate a distinct regime of plastic strain in the composite. Other details of the elastic-viscoplastic crystal plasticity framework used in this study can be found in our previous publications [5,85,120].

The results from the finite element simulation for compression along the **c**-axis are tabulated in Table 3, along with the results from a simple Schmid analysis assuming an uniaxial compressive stress state in both the matrix and the twin. In this loading condition, the elastic-plastic finite element simulations indicate that $\tau^\alpha / \tau_c^\alpha$ is highest for the activation of extension twins inside the already existing contraction twin, higher than even the value of $\tau^\alpha / \tau_c^\alpha$ for continued production of new contraction twins in the matrix. It should be noted that there are numerous prior reports of the formation of extension twins inside contraction twins in deformation studies on Mg alloys. The finite element results presented here for this case are therefore in full accord with these experimental observations. In fact, the extension variant predicted by the finite element simulation is $(01\bar{1}2)[0\bar{1}11]$, which is also the one reported experimentally [67]. As soon as the extension twins are produced inside the contraction twin, the original boundary between the contraction twin and the matrix will lose coherency and should become immobile. This explains why the contraction twins remained thin in our samples

when compressed along the **c**-axis, which in turn leads to production of new contraction twins in the same grain. In the process, the contraction twins dramatically reduce the effective slip length in the sample, and are highly potent in strain hardening Mg alloys.

Note that the finite element models described above satisfy equilibrium and compatibility conditions (in the weak numerical sense) and thereby aim to capture more accurately the stress fields in the matrix-twin composite. As shown in Table 3, a simple Schmid analyses assuming an uniaxial stress state in both the matrix and the twin indicates that $\tau^\alpha / \tau_c^\alpha$ is highest for basal slip inside the newly formed contraction twin. Although the activation of basal slip inside the twin would also lead to heterogeneity in the active deformation modes (there is not enough driving force for basal slip in the matrix), the reported experimental observations do not support this prediction [72].

Table 3 Comparison of predicted driving forces for various deformation mechanisms in a contraction twin-matrix composite based on the crystal plasticity finite element models and the highly simplified (uniform stress) Schmid model.

	$\tau^{CTW} / \tau_c^{CTW}$ contraction twins		$\tau^{TTW} / \tau_c^{TTW}$ extension twins		$\tau^{BAS} / \tau_c^{BAS}$ a - slip		$\tau^{PRI} / \tau_c^{PRI}$ a – slip		$\tau^{PYR} / \tau_c^{PYR}$ a – slip		$\tau^{PYR} / \tau_c^{PYR}$ (c + a) - slip	
	Twin	matrix	twin	matrix	twin	matrix	twin	matrix	twin	Matrix	twin	matrix
FEM Analysis	0.0	2.69	2.85	0.0	0.9	0.15	0.74	0.02	0.67	0.03	0.73	0.95
Schmid Analysis	0.45	1.0	0.53	0.0	1.93	0.0	0.26	0.0	0.36	0.0	0.22	0.36

The finite element model predictions for the extension along the **c**-axis along with the corresponding predictions from the simple Schmid analysis are summarized in Table 4. These results indicate that $\tau^\alpha / \tau_c^\alpha$ continues to be highest for the activation of

extension twins in the matrix. More importantly, the driving force for the formation of compression twins inside the extension twins is significantly lower, especially when it is recognized that the amount of twinning scales with $(\tau^\alpha / \tau_c^\alpha)^{1/m}$, where m (the rate-sensitivity parameter) takes very small values (typically of the order of 0.01). Consequently, we should expect extension twins to propagate unimpeded (either by growth of existing deformation twins and/or their coalescence).

Table 4 Comparison of predicted driving force for the various deformation mechanisms in an extension twin-matrix composite based on the crystal plasticity finite element models and the highly simplified (uniform stress) Schmid model.

	$\tau^{CTW} / \tau_c^{CTW}$ contraction twins		$\tau^{TTW} / \tau_c^{TTW}$ extension twins		$\tau^{BAS} / \tau_c^{BAS}$ a – slip		$\tau^{PRI} / \tau_c^{PRI}$ a – slip		$\tau^{PYR} / \tau_c^{PYR}$ a - slip		$\tau^{PYR} / \tau_c^{PYR}$ (c + a) - slip	
	twin	matrix	twin	matrix	twin	matrix	twin	matrix	twin	matrix	twin	matrix
FEM Analysis	2.84	0.0	0.0	3.18	0.79	0.07	0.96	0.02	0.84	0.01	0.76	0.95
Schmid Analysis	0.9	0.0	0.00	1.0	0.22	0.0	0.31	0.0	0.27	0.0	0.24	0.3

CHAPTER 5: CONCLUSIONS AND FUTURE WORK

5.1. Conclusions

1. It has been demonstrated that it is possible to speed up the crystal plasticity calculations by two orders of magnitude for both FCC and HCP metals using a compact database of Discrete Fourier Transforms (DFTs). It was seen that a limited set of dominant transforms adequately captured the dependence of the stresses, the lattice spins, and the strain hardening in individual crystals as a function of their lattice orientation and the applied deformation mode. A computationally efficient spectral interpolation scheme was devised and implemented to recover values of these functions for any selected combination of crystal orientation and deformation mode using only the dominant DFTs. The case studies revealed tremendous savings in the computational time, and provide a significant incentive for incorporation into the finite element simulations of bulk deformation processing operations. The significantly improved computational speed of the DFT method provided an engine for the fast computation of the yield surfaces, for the delineation of the uniform ductility-ultimate tensile strength closures, and for the process design.

The orientation distribution function (ODF) is an important tool to quantify the crystallographic texture in polycrystalline materials. Traditionally the ODF has been represented in terms of generalized spherical harmonics, which are computationally expensive. In this thesis, a new representation of the ODF in terms of discrete Fourier transforms (DFT) was presented. By exploiting the well know efficiency of FFT algorithms a spectral representation of texture readily

implemented in any programming language without the need for specialized GSH libraries was developed. In developing the DFT framework, a rectangular region, FZ3, was identified for cubic crystals that is 3 times the standard cubic-triclinic fundamental zone whereas a rectangular region, FZ, for hexagonal crystals in the Bunge-Euler space, which can easily be discretized into a regular grid. A mapping from both FZ3 for cubic and FZ for hexagonal, into the periodic Bunge-Euler space preserves a regular grid where the DFT calculations can be performed. These observations have been exploited in all computations presented in this work.

2. It has been observed that the Fourier coefficients for cubic materials corresponding to the boundary points on first-order elastic-plastic closures that do not require consideration of texture evolution are independent of the single crystal properties. This key observation enabled development of a new strategy for computing quickly the elastic-plastic closures of interest for a broad range of cubic materials. The new strategy involves computing and storing the set of Fourier coefficients corresponding to the boundary points on the closures of interest, and using this set of coefficients repeatedly with different material systems to quickly produce an atlas of property closures. This strategy has been successfully demonstrated with a few different combinations of pairs of effective elastic and plastic properties.
3. The delineation of property closures based on both the DFT and the GSH representation of the dependence of elastic and plastic properties on the local lattice orientation have been demonstrated. Both of these spectral approaches

provided identical answers. The maximum number of Fourier coefficients needed for the same variables in GSH representations was less than in the DFT representation, which means that the GSH representations are indeed more efficient in capturing the function with a smaller number of terms in the Fourier expansions. However, the DFT computations are significantly faster by at least two orders of magnitude because of the FFT algorithms.

4. Examples of closures with both orthorhombic and triclinic assumptions of the sample symmetry were presented. The delineation of the property closures for the triclinic textures required construction of the yield surfaces. The yield surfaces provided solutions for the tensile yield stress. From the presented examples, it was evident that there are indeed more property combinations available if triclinic sample symmetry in the material is assumed.
5. It was demonstrated that the underlying spectral framework of the MSD methodology facilitates an efficient consideration of the complete set of crystallographic textures in the design optimization. The benefits of the approach were successfully demonstrated with a specific design case study. It was seen that the overall performance is strongly influenced by the crystallographic texture in the sample.
6. Extensions to the MSD framework that facilitate delineation of a new class of property closures were presented. This new class of closures deals with properties associated with finite plastic strains (e.g. ultimate tensile strength and uniform ductility) and requires an explicit consideration of strain hardening and the concomitant evolution of the crystallographic texture. A new mathematical

procedure for successful delineation of these closures has been described and demonstrated.

7. Several examples of closures for selected combinations of plastic properties were obtained for two specific metal alloys. It was seen that the closures obtained were sensitive to the slip hardening characteristics exhibited by the alloys. Furthermore, it was also observed that the best textures that correspond to the optimized combinations of macroscale plastic properties were somewhat different for the two metals studied. This implies that different processing routes would be needed in the different metals to achieve the best possible performance. All of the examples presented in this study highlight the clear need and potential for the development of novel processing routes resulting in superior combinations of plastic properties in metallic alloys.
8. The MSD methodology has also been extended to address process design solutions where the goal is to identify a processing recipe to transform a given initial texture into an element of a desired set of textures, using an arbitrary combination of available manufacturing options. The advantages of this new approach were demonstrated using two case studies. In both cases, the texture network approach described here produced solutions that could not be arrived at by pure intuition or by brute-force methods (constant performance maximization or repeated trials).
9. It was observed that deformation twinning played a dominant role in the anisotropic stress-strain response and the concomitant microstructure evolution in the room temperature plastic deformation of AZ31 alloy. In particular, it was

observed that the extension twins in AZ31 appear to thicken relatively fast and encompass the entire grain in many instances, whereas the contraction twins remained fairly thin. Finite element simulations of twin-matrix composites revealed that there exists a relatively large driving force for the immediate formation of an extension twin inside the contraction twin, which in turn impedes the growth of the parent contraction twin. As a consequence, the contraction twins remain thin. Consequently, they are much more effective than extension twins in reducing the available slip length and enhancing strain hardening rates. Furthermore, the inability of the propagation of contraction twins indirectly promotes the alternative mechanisms of plastic deformation in the sample. In the samples tested in this study, this alternative mechanism is expected to be the 2nd pyramidal $\langle c+a \rangle$ slip. The forced activation of this non-basal slip mechanism may be responsible for the high strain hardening rates observed in our tests. In summary, the striking differences in the morphologies of the extension and the contraction deformation twins play a critical role in the strong anisotropy, the unusually high strain hardening rates, the apparent tension-compression asymmetry, and the damage initiation and the final failures exhibited by AZ31.

5.2. Suggestions for Future Work

1. Implementation of spectral crystal plasticity material subroutine into the FEM environment allowing for fully coupled simulations of the anisotropic stress-strain behavior and the texture evolution. An important consequence of this accomplishment would be avoiding the Taylor iso-strain simplification.

2. Development of second-order crystal plasticity theories to account for grain interactions and strain localization.
3. Development of the physics-based crystal plasticity models for Mg alloys.
4. Delineation of the elastic-plastic property closures using higher order statistics to improve the prediction.
5. Continuation of the building of process networks by exploring alternative algorithms, different initial textures, different prioritizing factors in building the network such as restrictions to subset of readily available deformation processing operations and a consideration of the cost associated with each specific deformation operation.

List of References

1. Kalidindi SR, Donohue BR, Li S. Modeling texture evolution in equal channel angular extrusion using crystal plasticity finite element models. *International Journal of Plasticity*;In Press, Corrected Proof.
2. Asaro RJ, Needleman A. Texture development and strain hardening in rate dependent polycrystals. *Acta Metallurgica et Materialia* 1985;33(6):923-953.
3. Mathur, K. K, Dawson PR. On modelling the development of crystallographic texture in bulk forming processes. *International Journal of Plasticity* 1989;5:67-94.
4. Bronkhorst CA, Kalidindi SR, Anand L. Polycrystalline plasticity and the evolution of crystallographic texture in FCC metals. *Philosophical Transactions of the Royal Society of London Series A-Mathematical Physical and Engineering Sciences* 1992;341(1662):443-477.
5. Kalidindi SR, Bronkhorst CA, Anand L. Crystallographic Texture Evolution in Bulk Deformation Processing of Fcc Metals. *Journal of the Mechanics and Physics of Solids* 1992;40(3):537-569.
6. Beaudoin AJ, Dawson PR, Mathur KK, Kocks UF. A hybrid finite element formulation for polycrystal plasticity with consideration of macrostructural and microstructural linking. *International Journal of Plasticity* 1995;11(5):501-521.
7. Beaudoin AJ, Mathur KK, Dawson PR, Johnson GC. Three-Dimensional Deformation Process Simulation With Explicit Use of Polycrystal Plasticity Models. *International Journal of Plasticity* 1993;9(7):833-860.
8. Delannay L, Kalidindi SR, Van Houtte P. Quantitative prediction of textures in aluminium cold rolled to moderate strains. *Materials Science and Engineering A* 2002;336(1-2):233-244.
9. Van Houtte P, Delannay L, Kalidindi SR. Comparison of two grain interaction models for polycrystal plasticity and deformation texture prediction. *International Journal of Plasticity* 2002;18(3):359-377.
10. S. R. Kalidindi AB, and R. Doherty. Detailed Analysis of Plastic Deformation in Columnar Polycrystalline Aluminum Using Orientation Image Mapping and Crystal Plasticity Models. *Proceedings of the Royal Society of London: Mathematical, Physical and Engineering Sciences* 2004.

11. Taylor GI. Plastic strain in metals. *Journal of the Institute of Metals* 1938;62:307-324.
12. Raabe D, Zhao Z, Roters F. A finite element method on the basis of texture components for fast predictions of anisotropic forming operations. *Steel Research* 2001;72(10):421-426.
13. Raabe D, Wang Y, Roters F. Crystal plasticity simulation study on the influence of texture on earing in steel. *Computational Materials Science* 2005;34(3):221-234.
14. Hosford WF, Caddell RM. *Metal forming mechanics and metallurgy*: Prentice-Hall, Inc; 1993.
15. Li DS, Garmestani H, Schoenfeld S. Evolution of crystal orientation distribution coefficients during plastic deformation. *Scripta Materialia* 2003;49(9):867-872.
16. Kalidindi SR, Duvvuru HK. Spectral methods for capturing crystallographic texture evolution during large plastic strains in metals. *Acta Materialia* 2005;53(13):3613-3623.
17. Bunge H, Esling C. Texture Development by Plastic Deformation. *Scripta Metall* 1984;18:191-195.
18. Clément A, Coulomb P. Eulerian simulation of deformation textures. *Scripta Metallurgica* 1979;13(9):899-901.
19. Frank FC. Orientation Mapping. *Metallurgical Transactions A* 1987;19A:403-408.
20. Sundararaghavan V, Zabaras N. Linear analysis of texture-property relationships using process-based representations of Rodrigues space. *Acta Materialia* 2007;55(5):1573-1587.
21. Ashby MF. *Materials Selection in Mechanical Design*: Butterworth-Heinemann; 1992. 502 p.
22. Olson GB. Computational Design of Hierarchically Structured Materials. *Science* 1997;277(29):1237-1242.
23. Olson GB. Pathways of Discovery Designing a new material world. *Science* 2000;228(12):933-998.
24. Olson GB. Systems design of hierarchically structured materials: Advanced steels. *Journal of Computer-Aided Materials Design* 1997;4 143–156.

25. Hao S, Moran B, Liu WK, Olson GB. A hierarchical multi-physics model for design of high toughness steels. *Journal of Computer-Aided Materials Design* 2003;10:99-142.
26. Campbell CE, Olson GB. Systems design of high performance stainless steels I. Conceptual and computational design. *Journal of Computer-Aided Materials Design* 2001;7:145–170.
27. Campbell CE, Olson GB. Systems design of high performance stainless steels II. Prototype characterization. *Journal of Computer-Aided Materials Design* 2001;7:171–194.
28. Sigmund O. Materials with prescribed constitutive parameters: An inverse homogenization problem. *International Journal of Solids and Structures* 1994;31(17):2313-2329.
29. Sigmund O. Tailoring materials with prescribed elastic properties. *Mechanics of Materials* 1995;20(4):351-368.
30. Sigmund O. A new class of extremal composites. *Journal of the Mechanics and Physics of Solids* 2000;48(2):397-428.
31. Sigmund O, Torquato S. Composites with extremal thermal expansion coefficients. *Applied Physics Letters* 1996;69(21):3203.
32. Sigmund O, Torquato S. Design of materials with extreme thermal expansion using a three-phase topology optimization method. *Journal of the Mechanics and Physics of Solids* 1997;45(6):1037-1067.
33. Sigmund O, Torquato S. Design of smart composite materials using topology optimization. *Smart Mater Struct* 1999;8:365-379.
34. Sigmund O, Torquato S, Aksay IA. On the design of 1-3 piezocomposites using topology optimization. *Journal of Materials Research* 1998;13(4):1038-1048.
35. Nelli Silva EC, Ono Fonseca JS, Kikuchi N. Optimal design of piezoelectric microstructures *Computational Mechanics* 1997;19(5):397-410.
36. Adams BL, Henrie A, Henrie B, Lyon M, Kalidindi SR, Garmestani H. Microstructure-sensitive design of a compliant beam. *Journal of the Mechanics and Physics of Solids* 2001;49(8):1639-1663.

37. Kalidindi SR, Houskamp JR, Lyon M, Adams BL. Microstructure sensitive design of an orthotropic plate subjected to tensile load. *International Journal of Plasticity* 2004;20(8-9):1561-1575.
38. Adams BL, Gao X, Kalidindi SR. Finite approximations to the second-order properties closure in single phase polycrystals. *Acta Materialia* 2005;53(13):3563-3577.
39. Lyon M, Adams BL. Gradient-based non-linear microstructure design. *Journal of the Mechanics and Physics of Solids* 2004;52:2569-2586.
40. Torquato S. *Random Heterogeneous Materials*. New York: Springer-Verlag; 2002.
41. Murat F, Tartar L. Optimality conditions and homogenization. In: *Non-linear variational problems*, A. Marino, L. Modica, S. Spagnolo, M. Deqiovannieds. London: Pitman; 1985.
42. Cherkaev AV. *Variational Methods for Structural Optimization*. New York: Springer; 2000.
43. Cherkaev AV, Gibiansky LV. Extremal structures of multiphase heat conducting composites. *International Journal of Solids and Structures* 1996;33(18):2609-2623.
44. Lurie KA. A stable spatio-temporal G-closure and Gm-closure of a set of isotropic dielectrics with respect to one-dimensional wave propagation. *Wave Motion* 2004;40(2):95-110.
45. Lyon M, Adams BL. Gradient-based non-linear microstructure design. *Journal of the Mechanics and Physics of Solids* 2004;52(11):2569-2586.
46. Adams BL, Lyon M, Henrie B. Microstructures by design: linear problems in elastic-plastic design. *International Journal of Plasticity* 2004;20(8-9):1577-1602.
47. Proust G, Kalidindi SR. Procedures for construction of anisotropic elastic-plastic property closures for face-centered cubic polycrystals using first-order bounding relations. *Journal of the Mechanics and Physics of Solids* 2006;54(8):1744-1762.
48. Knezevic M, Kalidindi SR. Fast computation of first-order elastic-plastic closures for polycrystalline cubic-orthorhombic microstructures. *Computational Materials Science* 2007;39(3):643-648.

49. Wu X, Proust G, Knezevic M, Kalidindi SR. Elastic-plastic property closures for hexagonal close-packed polycrystalline metals using first-order bounding theories. *Acta Materialia* 2007;55(8):2729-2737.
50. Adams BL, Garmestani H, Saheli G. Microstructure design of a two phase composite using two-point correlation functions. *Journal of Computer-Aided Materials Design* 2004;11:103–115.
51. Kalidindi SR, Houskamp JR. Application of the Spectral Methods of Microstructure Design to Continuous Fiber Reinforced Composites. *Journal of Composite Materials* 2007;41(8):909-930.
52. B.L. Mordike TE. Magnesium: Properties - applications - potential. *Materials Science and Engineering A* 2001;302:37-45.
53. Yoo MH. Slip, twinning, and fracture in hexagonal close-packed metals. *Metall Mater Trans A* 1981;12:409–418.
54. Roberts CS. *Magnesium and Its Alloys*: Wiley, New York/London.; 1960.
55. Obara T, Yoshinga H, Morozumi S. $\{112\}\langle -1-123 \rangle$ Slip system in magnesium. *Acta Metallurgica* 1973;21(7):845-853.
56. Kelly EW, Hosford WF. Plane-strain compression of magnesium and magnesium alloy crystals. *Trans Metall Soc AIME* 1968;242:5–13.
57. Lou XY, Li M, Boger RK, Agnew SR, Wagoner RH. Hardening evolution of AZ31B Mg sheet. *International Journal of Plasticity* 2007;23(1):44-86.
58. Yoshinaga H, Obara T, Morozumi S. Twinning deformation in magnesium compressed along the C-axis. *Materials Science and Engineering* 1973;12(5-6):255-264.
59. Agnew SR, Duygulu O. TEM Investigation of Dislocation Mechanisms in Mg Alloy AZ31B Sheet. *Mechanisms Technology* 2004 Edited by Alan A Lou TMS 2004:61-66.
60. Stohr JF, Poirier JP. Etude en microscopie electronique du glissement pyramidal $\{112\}\langle 1123 \rangle$ dans le magnesium *Philosophical Magazine* 1972;25:1313 - 1329
61. Agnew SR, Tomé CN, Brown DW, Holden TM, Vogel SC. Study of slip mechanisms in a magnesium alloy by neutron diffraction and modeling. *Scripta Materialia* 2003;48(8):1003-1008.

62. Muránsky O, Carr DG, Barnett MR, Oliver EC, Sittner P. Investigation of deformation mechanisms involved in the plasticity of AZ31 Mg alloy: In situ neutron diffraction and EPSC modelling. *Materials Science and Engineering: A* 2008;496(1-2):14-24.
63. Keshavarz Z, Barnett MR. EBSD analysis of deformation modes in Mg-3Al-1Zn. *Scripta Materialia* 2006;55(10):915-918.
64. Barnett MR. Twinning and the ductility of magnesium alloys: Part I: "Tension" twins. *Materials Science and Engineering: A* 2007;464(1-2):1-7.
65. Al-Samman T, Gottstein G. Room temperature formability of a magnesium AZ31 alloy: Examining the role of texture on the deformation mechanisms. *Materials Science and Engineering: A* 2008;488(1-2):406-414.
66. Barnett MR. Twinning and the ductility of magnesium alloys: Part II. "Contraction" twins. *Materials Science and Engineering: A* 2007;464(1-2):8-16.
67. Cizek P, Barnett MR. Characteristics of the contraction twins formed close to the fracture surface in Mg-3Al-1Zn alloy deformed in tension. *Scripta Materialia* 2008;59(9):959-962.
68. Barnett MR, Keshavarz Z, Beer AG, Ma X. Non-Schmid behaviour during secondary twinning in a polycrystalline magnesium alloy. *Acta Materialia* 2008;56(1):5-15.
69. Barnett MR, Davies CHJ, Ma X. An analytical constitutive law for twinning dominated flow in magnesium. *Scripta Materialia* 2005;52(7):627-632.
70. Barnett MR. A rationale for the strong dependence of mechanical twinning on grain size. *Scripta Materialia* 2008;59(7):696-698.
71. Wonsiewicz BC, Backofen WA. Plasticity of Magnesium Crystals. *Trans Metall Soc AIME* 1967;239(1422-1431).
72. Hartt WH, Reed-Hill RE. Internal Deformation Fracture of Second-Order {10-11}-{10-12} Twins in Magnesium. *Trans Metall Soc AIME* 1967;242:1127-1133.
73. Asgari S, El-Danaf E, Kalidindi SR, Doherty RD. Strain hardening regimes and microstructural evolution during large strain compression of low stacking fault energy fcc alloys that form deformation twins. *Metallurgical and Materials Transactions A: Physical Metallurgy and Materials Science* 1997;28A(9):1781-1795.

74. Asgari S, El-Danaf E, Shaji E, Kalidindi SR, Doherty RD. The secondary hardening phenomenon in strain-hardened MP35N alloy. *Acta Materialia* 1998;46(16):5795-5806.
75. Salem AA, Kalidindi SR, Doherty R, Semiatin SL. Strain hardening due to deformation twinning in alpha-titanium: Mechanisms. *Metall Trans A* 2006;37A:259.
76. Salem AA, Kalidindi SR, Doherty RD. Strain hardening regimes and microstructure evolution during large strain compression of high purity titanium. *Scripta Materialia* 2002;46(6):419-423.
77. Salem AA, Kalidindi SR, Doherty RD. Strain hardening of titanium: role of deformation twinning. *Acta Materialia* 2003;51(14):4225-4237.
78. Z. Zhao FR, W. Mao, D. Raabe,. Introduction of a Texture Component Crystal Plasticity Finite Element Method for Anisotropy Simulations. *Advanced Engineering Materials* 2001;3(12):984-990.
79. Bohlke T, Bertram A. Crystallographic texture induced anisotropy in copper: An approach based on a tensorial Fourier expansion of the CODF. *Journal De Physique. IV : JP*; 2003; Liege, Belgium. EDP Sciences. p 167-174. (*Journal De Physique. IV : JP*).
80. Adams BL, Olson T. The mesostructure--properties linkage in polycrystals. *Progress in Materials Science* 1998;43(1):1-87.
81. Rollett AD, Storch ML, Hilinski EJ, Goodman SR. Approach to Saturation in Textured Soft Magnetic Materials. *Metall Mater Trans A* 2001;32(10):2595.
82. Stojakovic D. Microstructure Evolution in Deformed and Recrystallized Electrical Steel: Drexel University; 2008.
83. Randle V, Engler O. Introduction to Texture Analysis. Macrotexture, Microstructure & Orientation Mapping: Gordon and Breach Science Publishers; 2000.
84. Bunge H-J. Texture analysis in materials science. Mathematical Methods. Morris PR, translator. Göttingen: Cuvillier Verlag; 1993.

85. Wu X, Kalidindi SR, Necker C, Salem AA. Prediction of crystallographic texture evolution and anisotropic stress-strain curves during large plastic strains in high purity [alpha]-titanium using a Taylor-type crystal plasticity model. *Acta Materialia* 2007;55(2):423-432.
86. Hill R. The elastic behavior of a crystalline aggregate. *Proceedings of the Royal Society of London Series A, Mathematical and Physical Sciences* 1952;65:349-354.
87. Paul B. Prediction of elastic constants of multiphase materials. *Trans Metall Soc AIME* 1960(218):36-41.
88. Hill R. Elastic properties of reinforced solids: some theoretical principles. *Journal of the Mechanics and Physics of Solids* 1963;11:357-372.
89. Sachs G. Zur Ableitung einer Fließbedingung. *Z Ver Deu Ing* 1928;72(22):734.
90. Winther G, Jensen DJ, Hansen N. Modelling Flow Stress Anisotropy Caused by Deformation Induced Dislocation Boundaries. *Acta Materialia* 1997;45(6):2455-2465.
91. Clausen B, Lorentzen T, Leffers T. Self-Consistent Modelling of the Plastic Deformation of fcc Polycrystals and its Implications for Diffraction Measurements of Internal Stresses. *Acta Materialia* 1998;46(9):3087-3098.
92. ISO/IEC IS 10918-1 | ITU-T Recommendation T.81.
93. <http://en.wikipedia.org/wiki/MP3>.
94. Bunge H. *Texture Analysis in Materials Science*. Butterworths 1982.
95. Knezevic M, Kalidindi SR, Mishra RK. Delineation of first-order closures for plastic properties requiring explicit consideration of strain hardening and crystallographic texture evolution. *International Journal of Plasticity* 2008;24(2):327-342.
96. Kalidindi SR, Houskamp JR, Lyons M, Adams BL. Microstructure sensitive design of an orthotropic plate subjected to tensile load. *International Journal of Plasticity* 2004;20(8-9):1561-1575.
97. Lyon M, Adams BL. Gradient-based non-linear microstructure design. *Journal of the Mechanics and Physics of Solids* 2004;52(11):2569-2586.
98. Beran MJ. *Statistical continuum theories*. New York: Interscience Publishers; 1968.

99. Kröner E. Bounds for effective elastic moduli of disordered materials. *J Mech Phys Solids* 1977;25:137-155.
100. Press WH, Teukolsky, S. A., Vetterling, W. T., and Flannery. B. P. *Numerical Recipes in C++*. 2002.
101. Briggs WL, Henson VE. *The DFT : an owner's manual for the discrete Fourier transform*. Philadelphia: Society for Industrial and Applied Mathematics; 1995.
102. Brigham EO. *The Fast Fourier Transform and Applications*. Englewood Cliffs: Prentice Hall; 1988.
103. Cooley JW, Tukey JW. Algorithm for the machine computation of complex Fourier series. *Mathematics of Computation* 1965;19:297-301.
104. Duhamel P, Vetterli M. Fast Fourier Transforms: A Tutorial Review and a State of the Art. *Signal Processing* 1990;19:259-299.
105. Kalidindi SR, Duvvuru HK, Knezevic M. Spectral calibration of crystal plasticity models. *Acta Materialia* 2006;54(7):1795-1804.
106. Knezevic M, Kalidindi SR, Fullwood D. Computationally efficient database and spectral interpolation for fully plastic Taylor-type crystal plasticity calculations of face-centered cubic polycrystals. *International Journal of Plasticity* 2008;24(7):1264-1276.
107. Van Houtte P. Application of plastic potentials to strain rate sensitive and insensitive anisotropic materials. *International Journal of Plasticity* 1994;10(7):719-748.
108. FORGE3. V6.3® 3D forging simulation software. TRANSVALOR S.A.
109. Li S, Kalidindi SR, Beyerlein IJ. A crystal plasticity finite element analysis of texture evolution in equal channel angular extrusion. *Materials Science and Engineering: A* 2005;410-411:207-212.
110. Midha A, Norton TW, Howell LL. On the Nomenclature, Classification, and Abstractions of Compliant Mechanisms. *Journal of Mechanical Design, Trans ASME* 1994(116):270-279.
111. Lekhnitskii SG. *Anisotropic Plates*: Gordon and Breach; 1968. 534 p.

112. Kalidindi SR. Accurate characterization of machine compliance for simple compression testing. *Experimental Mechanics* 1997;210-215.
113. EDAX, TSL. Manual for Orientation Imaging Microscopy (OIM™), Version 5.1.
114. Wu X, Kalidindi SR, Necker C, Salem AA. Modeling anisotropic stress-strain response and crystallographic texture evolution in α -titanium during large plastic deformation using Taylor-type models: Influence of initial texture and purity. *Metallurgical and Materials Transactions A* 2008;39A:3046-3054.
115. El-Danaf E, Kalidindi SR, Doherty RD, Necker C. Deformation texture transition in brass: critical role of micro-scale shear bands. *Acta Materialia* 2000;48(10):2665-2673.
116. Kalidindi SR. Modeling anisotropic strain hardening and deformation textures in low stacking fault energy fcc metals. *International Journal of Plasticity* 2001;17(6):837-860.
117. El-Danaf E, Kalidindi SR, Doherty RD. Influence of deformation path on the strain hardening behavior and microstructure evolution in low SFE FCC metals. *International Journal of Plasticity* 2001;17(9):1245-1265.
118. Reed-Hill RE. *Inhomogeneity of Plastic Deformation*. AMS, Metals Park, OH 1973.
119. T. Fabian, Z. Trojanova, Kuzel R. The Evolution of Dislocation Structure as a Function of Deformation Temperature in UFG Magnesium Determined by X-Ray Diffraction. *Proceedings of the 7th International Conference on Magnesium Alloys and their Applications* 2006.
120. Kalidindi SR. Incorporation of deformation twinning in crystal plasticity models. *Journal of the Mechanics and Physics of Solids* 1998;46(2):267-271.
121. Hill R. A Theory of the Yielding and Plastic Flow of Anisotropic Metals. *Proceedings of the Royal Society of London Series A, Mathematical and Physical Sciences* 1948;193(1033):281-297.
122. Considère M. Mémoire sur l'emploi du fer et de l'acier dans les constructions. *Annales des Ponts et Chaussées* 1885;9:574.

APPENDIX A: DEFINITIONS OF SELECTED MACROSCALE MATERIAL PROPERTIES USED IN THIS WORK

The effective elastic behavior of polycrystalline metals of interest in this study can be expressed through a generalization of the Hooke's law. The components of the local elastic stiffness tensor for both FCC and HCP metals can be written as a function of the local crystal orientation and the fundamental elastic crystal constants [86-88]. As an example, the components of the local elastic stiffness tensor for cubic metals can be written as a function of the local crystal orientation as

$$C_{abcd}(g) = C_{12}\delta_{ab}\delta_{cd} + C_{44}(\delta_{ac}\delta_{bd} + \delta_{ad}\delta_{bc}) + (C_{11} - C_{12} - 2C_{44}) \sum_{r=1}^3 g_{ar}g_{br}g_{cr}g_{dr} \quad (\text{A.1})$$

where g_{ij} are the components of an orthogonal coordinate transformation matrix relating the crystal reference frame to the sample reference frame, and C_{11} , C_{12} , C_{44} , are the fundamental elastic constants of a cubic crystal.

A common formalism for describing anisotropic yield surfaces is the orthorhombic Hill's yield surface description [121]. The anisotropic material yield parameters can be estimated for a polycrystalline material using an extended version of the Taylor's model and the Sachs model [89]. These models constitute upper bound and lower bound predictions for the macroscopic yield strengths, respectively.

In evaluating tensile yield strength σ_{y1} for orthorhombic textures using the Taylor-type model, the macroscopic velocity gradient imposed on each crystal (see Eq. 3.7) can take any value in the range $\theta \in \left[\frac{\pi}{6}, \frac{\pi}{2}\right)$. The local stresses computed by the rigid-

body Taylor model are deviatoric. The hydrostatic component can be computed by establishing the value of θ (denoted as θ^*) for which the averaged lateral stresses over the polycrystal are equal to each other, i.e. $\bar{\sigma}'_{33}(\theta) = \bar{\sigma}'_{22}(\theta)$. The tensile yield strength of the polycrystal in the \mathbf{e}_1 -direction is then computed as

$$\sigma_{y1} = \bar{\sigma}'_{11}(\theta^*) - \bar{\sigma}'_{22}(\theta^*). \quad (\text{A.2})$$

Note the tensile yield stress for textures not possessing the orthorhombic sample symmetry cannot be computed using the above methodology. In the samples with no orthorhombic sample symmetry the shear stress components do not cancel each other. One way to compute the tensile yield stress for the triclinic textures is using the yield surface, which was the method adopted in this work.

The R -ratio (also called the Lankford parameter) represents the ratio of the true width strain to the true thickness strain in a tensile test. The R -ratio is a prime example of a macroscale plastic property of the metal that is of significant interest in sheet metal forming operations. It is generally acknowledged that higher values of R enhance the workability of sheet metal products. It always applies to the samples with orthorhombic sample symmetry, so the value of R_1 (value of R when loaded in tension in the \mathbf{e}_1 -direction) is then defined as

$$R_1 = -\frac{\cos\left(\theta^* + \frac{\pi}{3}\right)}{\cos(\theta^*)}. \quad (\text{A.3})$$

The method described above can be similarly extended to computation of R_2 and R_3 .

Uniform ductility (e_u) and the ultimate tensile strength (σ_{UTS}) are defined using the Considere's criterion [122]. To facilitate the computation of these variables from Taylor-type models, the evolution of the true stress-true strain curve in tension is analyzed to establish the point of necking as

$$\left. \frac{d\sigma}{d\varepsilon} \right|_{\varepsilon=\varepsilon_n} = \sigma_n, \quad (\text{A.4})$$

where σ_n and ε_n denote the true stress and true strain at the point of necking. The uniform ductility, e_u , and the ultimate tensile strength, σ_{UTS} , are then easily computed as

$$e_u = \exp(\varepsilon_n) - 1, \quad \sigma_{UTS} = \frac{\sigma_n}{1 + e_n}. \quad (\text{A.5})$$

APPENDIX B: PROCEDURES FOR DELINEATION OF CLOSURES FOR PROPERTIES THAT DO NOT REQUIRE CONSIDERATION OF STRAIN HARDENING AND CRYSTALLOGRAPHIC TEXTURE EVOLUTION

Delineation of a first-order closure requires evaluation of volume averaged quantities. As an example, consider the expression for \bar{C}_{1111} using both GSH representation [47] and DFT representation developed here:

$$\bar{C}_{1111} = C_{12} + 2C_{44} + (C_{11} - C_{12} - 2C_{44}) \left[{}_{1111}A_0^{11} + \frac{1}{9} \sum_{v=1}^3 {}_{1111}A_4^{1v} F_4^{1v} \right] \quad (\text{B.1})$$

$$\bar{C}_{1111} = C_{12} + 2C_{44} + (C_{11} - C_{12} - 2C_{44}) \left[\frac{1}{B} \sum_{k=0}^{B/2} {}_{1111}\tilde{P}_k F_k \right]. \quad (\text{B.2})$$

In Eqs. (B.1 and B.2), C_{11} , C_{12} , and C_{44} denote the three independent elastic stiffness parameters for cubic crystals (these represent the elastic stiffness of the single crystal in Voigt notation and define the elastic anisotropy for cubic crystals as $A = 2C_{44}/(C_{11} - C_{12})$) and ${}_{1111}A_i^{\mu\nu}$ and ${}_{1111}\tilde{P}_k$ denote the property coefficients (see Eq. 2.19 for the GSH or 3.5 for the DFT representation) for the selected stiffness component. Equations (B.1 and B.2) indicate that the complete set of textures corresponding to a prescribed value of \bar{C}_{1111} would lie on a plane in the Fourier space described earlier. If this plane intersects the hull shown in Fig. 6, it implies that the prescribed value of \bar{C}_{1111} is actually feasible in the material system being studied. More importantly, we recognized the geometry (i.e. orientation) of these iso-property planes in the Fourier space is completely independent of the values of C_{11} , C_{12} , and C_{44} . A similar conclusion holds

when volume averaged plastic stresses are considered in the evaluation of the bounds for effective yield properties or the effective R -values. In the case of plastic properties, the geometry of the iso-property planes can be shown to be independent of the value of the slip resistance, s (which has been assumed here to be the same for all crystals in the case of cubic polycrystalline metals).

Only some of the bounds for the effective elastic-plastic properties of interest are given directly by the volume averaged values. Clearly, several of the bounds are complex nonlinear functions of the volume averaged values (see Eqs. 2.13 – 2.15). In such cases, the complete set of textures corresponding to a prescribed value of the bound corresponds to an iso-property surface in the Fourier space [46]. It is discovered in this work that the geometry of the iso-property surfaces for all of the elastic-plastic bounds associated with cubic-orthorhombic textures is completely independent of the values of the fundamental single crystal elastic and plastic properties (i.e. independent of C_{11} , C_{12} , and C_{44} and s). In other words, a given iso-property surface for one cubic material system would also be an iso-property surface for another cubic material system, except that the given surface would correspond to different values of the effective property in the two different material systems.

Consider two iso-property surfaces corresponding to the bounds of two different effective elastic-plastic properties of interest. In identifying the first-order closures, we are now only interested in the intersections of these iso-property surfaces on the surface of the texture hull, as these would correspond to the points on the boundary of the first-order property closure we seek. Because the geometry of the iso-property surfaces for elastic-plastic properties of interest are independent of the single crystal properties, we

can conclude that the Fourier coefficients corresponding to the boundary points on the first-order property closures should also be independent of the single crystal properties for the class of cubic-orthorhombic materials being considered here.

An important consequence of the above observation is that it provides a new strategy for quick computation of first-order property closures for a broad range of cubic materials. This is because one needs to do the complicated searches described in the previous section for the boundary points on the desired closure only once, and document all of the corresponding Fourier coefficients. Once these Fourier coefficients are stored appropriately, computation of the same property closure for a different material can be accomplished with minimal computational effort because it only involves evaluation of the effective properties for the catalogued list of Fourier coefficients. We have verified this observation extensively, and found it to hold true in all of the case studies we conducted on the properties that do not require consideration of the texture evolution. It should be noted that this procedure holds true for both GSH and FFT descriptions.

APPENDIX C: PROCEDURE FOR DELINEATION OF CLOSURES FOR PLASTIC PROPERTIES REQUIRING EXPLICIT CONSIDERATION OF STRAIN HARDENING AND CRYSTALLOGRAPHIC TEXTURE EVOLUTION

Procedure for the delineation of property closures addressed in the prior section was only for the properties associated with a static microstructure (i.e. the evolution of texture with imposed deformation and concomitant strain hardening were not considered). This approach could not be extended in simple ways for properties that need to explicitly account for microstructure evolution. A novel scheme to delineate the property closures of the properties associated with finite strains is described here.

The methodology explored here for building first-order closures starts with a consideration of a set of points in the texture hull that correspond to “eigen textures” [38]. Because of the orthorhombic sample symmetry used in this study, each eigen texture corresponds to the texture produced by a set of four equi-volume single crystals that are selected to satisfy the orthorhombic symmetry at the sample scale. The set of eigen textures is selected while ensuring an adequate coverage of the fundamental zone (FZ). The property combinations for these eigen textures are first evaluated using the spectral linkages described in the previous sections. A finite number of textures corresponding to the boundary of this closure were then selected. The macroscale property combinations for the weighted combinations of these textures, taking one pair of textures at a time, were evaluated systematically (considering all possible combinations of pairs of the selected textures). As expected, these computations revealed that some of the property combinations outside the eigen-texture closure were indeed possible, i.e. the results expanded the closure. Once again a new set of textures corresponding to the new

boundary of the expanded closure were selected (this time these were a mixture of eigen textures and non-eigen textures) and the property combinations corresponding to the weighted combinations of these (for all possible pairs of selected textures) were evaluated to see if they further expanded the closure. This process was repeated until the closure did not expand in any discernable way. The method described above to produce a closure essentially follows the main ideas underlying genetic algorithms, where good solutions are pre-selected (as we have done here by selecting the textures producing property combinations on the boundary of the closure) and “mutations” or “cross-overs” (weighted combinations of textures in our approach) are explored.

APPENDIX D: SPECTRAL CRYSTAL PLASTICITY CODE FOR FCC METALS

The following code computes the texture evolution and the anisotropic stress-strain response in any deformation process defined by the velocity gradient tensor.

```

load Fo_ns_11.mat
load Fo_ns_22.mat
load Fo_ss_12.mat
load Fo_ss_13.mat
load Fo_ss_23.mat
load Fo_ws_12.mat
load Fo_ws_13.mat
load Fo_ws_23.mat
load Fo_GD.mat
load Super_set.mat
% return

load Initial_1000_random.txt

Total_Time = 1000; % User enters
L = [ 0 0.001 0; 0 0 0; 0 0 0];
So = 16.0;
ho = 180.0;
Ss = 148.0;
exp_a = 2.25;

Strain_Increment = .05;
mo = 0.01; % The rate sensitivity parameter
DGo = 0.001; % Reff. slip rate
s_ref = 100.0; % Reff. slip resistance

D_app_sa = 1/2.*(L+L');
W_app_sa = 1/2.*(L-L');

[V_eig,D_eig] = eigs(D_app_sa, 3, 'lm');

V_eig(:,3) = cross(V_eig(:,1),V_eig(:,2));

eps_dot = norm(D_eig, 'fro');

if D_eig(1,1) < 0
    eps_dot = -eps_dot;
end

Total_Strain = eps_dot*Total_Time;
DT = Strain_Increment/eps_dot;
n_steps = round(Total_Time/DT);

D_unit = D_eig./eps_dot;

```

```

DT = Total_Time/n_steps;

theta = atan2((-2*D_unit(1,1)-D_unit(3,3)), sqrt(3)*D_unit(3,3));
% keyboard
if theta<0
    theta = theta+pi;
end

Q_p_sam = reshape(V_eig, 1, 9);

W_app_pr = V_eig'*W_app_sa*V_eig;

[eul] = RotateIntoFZ(Initial_1000_random, 0, 0, 0, Q_p_sam, 0,
n_steps);

sizeF = [120, 120, 120, 120];
m_fine = 3;

sizeF = sizeF.*m_fine;

termsdim4 = m_fine.*ones(1,size(eul,1)).*round(rad2deg(theta))/3;
% termsdim4 = 15.*ones(1,size(eul,1));
No = numel(Initial_1000_random(:,1));
s_dot = So*ones(No,1);
tic

strain = ([0:Strain_Increment:Total_Strain])';
STRESS_VEC = zeros(1,6); EQ_STRESS = 0;
for jj = 1:n_steps
    jj
    Super_mat = 2*exp(2*pi*i/sizeF(1).*((Super_set(:,1)-1)*(eul(:,3))'
+ (Super_set(:,2)-1)* ...
    (eul(:,2))' + (Super_set(:,3)-1)*(eul(:,1))' + (Super_set(:,4)-
1)*(termsdim4)));

    sum_gamma_dot = real(Fo_GD.'*Super_mat./prod(sizeF./m_fine));

    stress_11 = real(Fo_ns_11(:,1).'*Super_mat./prod(sizeF./m_fine));
    stress_22 = real(Fo_ns_22(:,1).'*Super_mat./prod(sizeF./m_fine));
    stress_12 = real(Fo_ss_12(:,1).'*Super_mat./prod(sizeF./m_fine));
    stress_13 = real(Fo_ss_13(:,1).'*Super_mat./prod(sizeF./m_fine));
    stress_23 = real(Fo_ss_23(:,1).'*Super_mat./prod(sizeF./m_fine));

    w_12 = real(Fo_ws_12(:,1).'*Super_mat./prod(sizeF./m_fine));
    w_13 = real(Fo_ws_13(:,1).'*Super_mat./prod(sizeF./m_fine));
    w_23 = real(Fo_ws_23(:,1).'*Super_mat./prod(sizeF./m_fine));

    s_dot = s_dot + ho.*(1-
(s_dot./Ss)).^exp_a.*(eps_dot/DGo).*sum_gamma_dot'.*DT;

[eul]=RotateIntoFZ(deg2rad(eul),(eps_dot/DGo).*w_12'.*DT+W_app_pr(2,1).

```



```

*DT, (eps_dot/DGo).*w_13'.*DT+W_app_pr(3,1).*DT,
(eps_dot/DGo).*w_23'.*DT+W_app_pr(3,2).*DT, Q_p_sam, jj, n_steps);

S11(jj) = mean(s_dot.*stress_11'./100);
S22(jj) = mean(s_dot.*stress_22'./100);
S12(jj) = mean(s_dot.*stress_12'./100);
S13(jj) = mean(s_dot.*stress_13'./100);
S23(jj) = mean(s_dot.*stress_23'./100);

STRESS_Mat = ((eps_dot/DGo).^mo).*sign(eps_dot/DGo).*[S11(jj),
S12(jj), S13(jj); S12(jj), S22(jj), S23(jj); S13(jj), S23(jj), -
(S11(jj)+S22(jj))];
STRESS_TENSOR = [V_eig*STRESS_Mat*V_eig'];

EQ_STRESS = [EQ_STRESS; sqrt(1/2.*((STRESS_TENSOR(1,1)-
STRESS_TENSOR(2,2)).^2+(STRESS_TENSOR(1,1)...
-STRESS_TENSOR(3,3)).^2+(STRESS_TENSOR(2,2)-
STRESS_TENSOR(3,3)).^2)+...
3*STRESS_TENSOR(1,2).^2+3*STRESS_TENSOR(1,3).^2+3*STRESS_TENSOR(2,3).^2
)];

EQ_STRESS_1 = [ sqrt(1/2)*sqrt((STRESS_TENSOR(1,1)-
STRESS_TENSOR(2,2)).^2+(STRESS_TENSOR(1,1)...
-STRESS_TENSOR(3,3)).^2+(STRESS_TENSOR(2,2)-
STRESS_TENSOR(3,3)).^2)+...
6*STRESS_TENSOR(1,2).^2+6*STRESS_TENSOR(1,3).^2+6*STRESS_TENSOR(2,3).^2
)];

STRESS_VEC = [STRESS_VEC; [STRESS_TENSOR(1,1), STRESS_TENSOR(2,2),
STRESS_TENSOR(3,3), STRESS_TENSOR(1,2), STRESS_TENSOR(1,3),
STRESS_TENSOR(2,3)]];
toc
end

function [angles_temp ] = RotateIntoFZ(euler, w21_rec, w31_rec,
w32_rec, Q_p_sam, flag, n_steps)

GRmatmult = @GRmatmult;

gmat = @(phil,Phi,phi2) [cos(phil).*cos(phi2)-
sin(phil).*cos(Phi).*sin(phi2), -cos(phil).*sin(phi2)-
sin(phil).*cos(Phi).*cos(phi2), sin(phil).*sin(Phi), ...
sin(phil).*cos(phi2)+cos(phil).*cos(Phi).*sin(phi2), -
sin(phil).*sin(phi2)+cos(phil).*cos(Phi).*cos(phi2), -
cos(phil).*sin(Phi) , ...
sin(Phi).*sin(phi2), sin(Phi).*cos(phi2), cos(Phi)];

R = @(axis,ang)[(1-axis(:,1).^2).*cos(ang)+axis(:,1).^2, ...
axis(:,1).*axis(:,2).*(1-cos(ang))+axis(:,3).*sin(ang),
...

```

```

        axis(:,1).*axis(:,3).*(1-cos(ang))-
axis(:,2).*sin(ang), ...
        axis(:,1).*axis(:,2).*(1-cos(ang))-axis(:,3).*sin(ang),
...
        (1-axis(:,2).^2).*cos(ang)+axis(:,2).^2, ...
        axis(:,2).*axis(:,3).*(1-
cos(ang))+axis(:,1).*sin(ang), ...
        axis(:,1).*axis(:,3).*(1-
cos(ang))+axis(:,2).*sin(ang), ...
        axis(:,2).*axis(:,3).*(1-cos(ang))-axis(:,1).*sin(ang),
...
        (1-axis(:,3).^2).*cos(ang)+axis(:,3).^2];

ang = sqrt(w21_rec.^2 + w31_rec.^2 + w32_rec.^2);
cond = find(ang == 0);
axis_1(cond) = 1.0; axis_2(cond) = 0.0; axis_3(cond) = 0.0;
cond = setdiff(1:numel(ang),cond);
axis_1(cond) = w32_rec(cond)./ang(cond);
axis_2(cond) = -w31_rec(cond)./ang(cond);
axis_3(cond) = w21_rec(cond)./ang(cond);

Vect_Rot = R([axis_1(:),axis_2(:),axis_3(:)],ang);

angles = gmat(euler(:,1),euler(:,2),euler(:,3));
ind = reshape(1:9,3,3);
Q_p_sam = repmat(Q_p_sam,size(euler,1),1);

% Texture in principle frame
%%%%%%%%%%%%%%%%%%%%%%%%%%%%%%%%%%%%%%%%%%%%%%%%%%%%%%%%%%%%%%%%%%%%%%%%%%%%%%
%%%%%%%%%%%%%%%%%%%%%%%%%%%%%%%%%%%%%%%%%%%%%%%%%%%%%%%%%%%%%%%%%%%%%%%%%%%%%%
if (flag == 0)
    % Q_p_sam needs to be transposed in order to move texture in
principle frame " Q_p_sam'*angles ";
    % Moreover Q_pr has to be in a suitable order to extract the euler
angles
    Q_pr(:,1) = sum(Q_p_sam(:,ind(:,1)).*angles(:,ind(1,:)),2);
    Q_pr(:,2) = sum(Q_p_sam(:,ind(:,2)).*angles(:,ind(1,:)),2);
    Q_pr(:,3) = sum(Q_p_sam(:,ind(:,3)).*angles(:,ind(1,:)),2);
    Q_pr(:,4) = sum(Q_p_sam(:,ind(:,1)).*angles(:,ind(2,:)),2);
    Q_pr(:,5) = sum(Q_p_sam(:,ind(:,2)).*angles(:,ind(2,:)),2);
    Q_pr(:,6) = sum(Q_p_sam(:,ind(:,3)).*angles(:,ind(2,:)),2);
    Q_pr(:,7) = sum(Q_p_sam(:,ind(:,1)).*angles(:,ind(3,:)),2);
    Q_pr(:,8) = sum(Q_p_sam(:,ind(:,2)).*angles(:,ind(3,:)),2);
    Q_pr(:,9) = sum(Q_p_sam(:,ind(:,3)).*angles(:,ind(3,:)),2);

    angles_temp = GRmatmult(Q_pr);
    angles_temp = round(rad2deg(angles_temp));

    return
end
%%%%%%%%%%%%%%%%%%%%%%%%%%%%%%%%%%%%%%%%%%%%%%%%%%%%%%%%%%%%%%%%%%%%%%%%%%%%%%
%%%%%%%%%%%%%%%%%%%%%%%%%%%%%%%%%%%%%%%%%%%%%%%%%%%%%%%%%%%%%%%%%%%%%%%%%%%%%%
G(:,1) = sum(Vect_Rot(:,ind(1,:)).*angles(:,ind(1,:)),2); % ind(1,:) is
the first column of "g"; Vect_Rot is transpose so that is why they have
the same indices. This is really rotation
G(:,2) = sum(Vect_Rot(:,ind(2,:)).*angles(:,ind(1,:)),2);

```

```

G(:,3) = sum(Vect_Rot(:,ind(3,:)).*angles(:,ind(1,:)),2);
G(:,4) = sum(Vect_Rot(:,ind(1,:)).*angles(:,ind(2,:)),2);
G(:,5) = sum(Vect_Rot(:,ind(2,:)).*angles(:,ind(2,:)),2);
G(:,6) = sum(Vect_Rot(:,ind(3,:)).*angles(:,ind(2,:)),2);
G(:,7) = sum(Vect_Rot(:,ind(1,:)).*angles(:,ind(3,:)),2);
G(:,8) = sum(Vect_Rot(:,ind(2,:)).*angles(:,ind(3,:)),2);
G(:,9) = sum(Vect_Rot(:,ind(3,:)).*angles(:,ind(3,:)),2);

% In the last time increment transform the texture in the sample frame
%%%%%%%%%%%%%%%%%%%%%%%%%%%%%%%%%%%%%%%%%%%%%%%%%%%%%%%%%%%%%%%%%%%%%%%%
%%%%%%%%%%%%%%%%%%%%%%%%%%%%%%%%%%%%%%%%%%%%%%%%%%%%%%%%%%%%%%%%%%%%%%%%

if (flag == n_steps)

    GG(:,1) = sum(Q_p_sam(:,ind(1,:)).*G(:,ind(:,1))),2);
    GG(:,2) = sum(Q_p_sam(:,ind(2,:)).*G(:,ind(:,1))),2);
    GG(:,3) = sum(Q_p_sam(:,ind(3,:)).*G(:,ind(:,1))),2);
    GG(:,4) = sum(Q_p_sam(:,ind(1,:)).*G(:,ind(:,2))),2);
    GG(:,5) = sum(Q_p_sam(:,ind(2,:)).*G(:,ind(:,2))),2);
    GG(:,6) = sum(Q_p_sam(:,ind(3,:)).*G(:,ind(:,2))),2);
    GG(:,7) = sum(Q_p_sam(:,ind(1,:)).*G(:,ind(:,3))),2);
    GG(:,8) = sum(Q_p_sam(:,ind(2,:)).*G(:,ind(:,3))),2);
    GG(:,9) = sum(Q_p_sam(:,ind(3,:)).*G(:,ind(:,3))),2);
    G = GG;

end
%%%%%%%%%%%%%%%%%%%%%%%%%%%%%%%%%%%%%%%%%%%%%%%%%%%%%%%%%%%%%%%%%%%%%%%%
%%%%%%%%%%%%%%%%%%%%%%%%%%%%%%%%%%%%%%%%%%%%%%%%%%%%%%%%%%%%%%%%%%%%%%%%
    angles_temp = GRmatmult(G);
    angles_temp = round(rad2deg(angles_temp));

function angf = GRmatmult(newpos)

angf = zeros(size(newpos,1),3);
angf(:,1:3) = [atan2(newpos(:,7),-
1*newpos(:,8)),acos(newpos(:,9)),atan2(newpos(:,3),newpos(:,6))];
cond = find(abs(newpos(:,9)) == 1);

if not isempty(cond) angf(cond,[1,3]) =
[acos(newpos(cond,1)),zeros(size(cond))];
    cond2 = find(newpos(cond,2) < 0 ); angf(cond(cond2),1) = 2*pi -
angf(cond(cond2),1);
end;

% Make sure angles are positive
cond = find(angf(:,1) < 0 );
if not isempty(cond) angf(cond,1) = angf(cond,1)+ 2*pi; end;
cond = find(angf(:,2) < 0 );
if not isempty(cond) angf(cond,2) = angf(cond,2)+ 2*pi; end;
cond = find(angf(:,3) < 0 );
if not isempty(cond) angf(cond,3) = angf(cond,3)+ 2*pi; end;

```

APPENDIX E: ELASTIC PROPERTY CLOSURE CALCULATOR FOR FCC CRYSTALS WITH TRICLINIC SAMPLE SYMMETRY USING FFT METHODS

```

inputC11 = 168.4;
inputC12 = 121.4;
inputC44 = 75.4;
inputS11 = 0.0149950327014;
inputS12 = -0.0062815630433;
inputS44 = 0.0132625994695;

load Super_set;

load euler.txt

function [Upper_bound_11, Lower_bound_11, Upper_bound_13,
Lower_bound_13] = ...
    genBounds(inputEulerAngles, inputC11, inputC12, inputC44,
inputS11, inputS12, inputS44, Super_set)

if nargin ~= 8
    error('Check Arguments');
end

[outputAngles,cTensors,sTensors] = FFTElasticityCalc(inputEulerAngles,
inputC11, inputC12, inputC44, inputS11, inputS12, inputS44, Super_set);

s_inv = inv(sTensors);
DELTA_one = abs(cTensors(1,1) - s_inv(1,1));
DELTA_two = abs(cTensors(6,6) - s_inv(6,6));

% Upper bounds
Upper_bound_11 = cTensors(1,1);
Upper_bound_13 = min(cTensors(1,6), s_inv(1,6)) +
sqrt(DELTA_one*DELTA_two);
% Upper_bound_13 = cTensors(1,2);

% Lower bounds
Lower_bound_11 = s_inv(1,1);
Lower_bound_13 = max(cTensors(1,6), s_inv(1,6)) -
sqrt(DELTA_one*DELTA_two);

function [outputCountedAngles outputCTensor outputSTensor] = ...
    FFTElasticityCalc(inputEulerAngles, inputC11, inputC12, inputC44,
inputS11, inputS12, inputS44, Super_set)
global g_gPropertyCoefficients

```

```

global g_cFiles
global g_propertyTensorIndices

% Get Frequency Count...
countedAngles = genFrequencyCount(inputEulerAngles);
cUniqueAngles = size(countedAngles,1);
cTotalAngles = size(inputEulerAngles,1);

% Load Files...
prefix = 'Fo_C';
lenPrefix = size(prefix,2); % =4
if(isempty(g_gPropertyCoefficients))
    fFiles = ls([prefix,'*']); % ls - list
    cFiles = size(fFiles,1);
    g_cFiles = cFiles;

    szNames = zeros(cFiles,8);
    propertyTensorIndices = zeros(cFiles,4);
    for idxFile=1:cFiles
        curName = fFiles(idxFile,:);
        idxMat = strfind(curName, '.mat');
        if(isempty(idxMat))
            error('Illegal File: %s', curName);
        end
        curName = curName(1:(idxMat-1));

        % Load file and Dereference Data...
        tmpValues = load(curName);
        fieldNames = fieldnames(tmpValues);
        if(numel(fieldNames) ~= 1)
            error('Only one variable per mat file. (%s)', curName);
        end
        tmpValues = getfield(tmpValues, fieldNames{1});

        if(isempty(g_gPropertyCoefficients))
            g_gPropertyCoefficients = zeros(cFiles, numel(tmpValues));
        end
        g_gPropertyCoefficients(idxFile,:) = tmpValues;

        % Break into indicies F_abcd
        szComponent = char(curName(lenPrefix+1:end));
        if(numel(szComponent) ~= 4)
            error('Illegal Tensor Component. Check Filename');
        end
        idxA = round(str2num(szComponent(1)));
        idxB = round(str2num(szComponent(2)));
        idxC = round(str2num(szComponent(3)));
        idxD = round(str2num(szComponent(4)));
        if idxA > 3 || idxB > 3 || idxC > 3 || idxD > 3 || idxA < 1 ||
        idxB < 1 || idxC < 1
            error('Illegal Tensor Component. Check Filename');
        end
        propertyTensorIndices(idxFile, :) = [idxA,idxB,idxC,idxD];
    end
end

```

```

    end

    g_propertyTensorIndices = propertyTensorIndices;
end

% For each Unique Crystal...
retProperties = zeros(3,3,3,3);
outputCTensor = zeros(6,6);
outputSTensor = zeros(6,6);
cSuperSet = size(Super_set,1);
FTerm = zeros(cSuperSet,1);
for idxCrystal=1:cUniqueAngles

    % Twiddle-Factor...
    tempSuper = ( (Super_set(:,3)-
1.0).*(double(countedAngles(idxCrystal,1))) + ...
                (Super_set(:,2)-
1.0).*(double(countedAngles(idxCrystal,2))) + ...
                (Super_set(:,1)-
1.0).*(double(countedAngles(idxCrystal,3)))));

    % Frequency Count...
    FTerm = FTerm + double(countedAngles(idxCrystal,4)).*exp(-
(2.0*pi*i/360).*tempSuper);
end
FTerm = (1.0/cTotalAngles)*FTerm;

% For each property...
for idxProperty = 1:g_cFiles

    % From paper: (1/G)*sum(A_k*F_k)
    retProperties(g_propertyTensorIndices(idxProperty,1), ...
                g_propertyTensorIndices(idxProperty,2), ...
                g_propertyTensorIndices(idxProperty,3), ...
                g_propertyTensorIndices(idxProperty,4)) ...
    = ...

    ((1.0/(360^3.0))^1.0)*real(g_gPropertyCoefficients(idxProperty,:)*FTerm)
;

end

outputSTensor(:, :) =
flattenTensor(genComplianceTensor(inputS11,inputS12, inputS44,
retProperties));
outputCTensor(:, :) =
flattenTensor(genStiffnessTensor(inputC11,inputC12, inputC44,
retProperties));

% Actual angles processed...

```

```
outputCountedAngles = deg2rad(double(countedAngles(:,1:end-1)));
```

```
function retCompliance = genComplianceTensor(inputS11, inputS12,
inputS44, inputGTensor)
```

```
retCompliance = zeros(3,3,3,3);
for idxA=1:3
    for idxB=idxA:3
        for idxC=1:3
            for idxD=idxC:3
                % From Page 138 of MSD Book.
                if(idxA == 1 && idxB == 2 && idxC == 1 && idxD == 2)
                    % keyboard;
                end
                retCompliance(idxA,idxB,idxC,idxD) =
inputS12*(idxA==idxB)*(idxC==idxD) + ...

(inputS44/4.0)*((idxA==idxC)*(idxB==idxD)+(idxA==idxD)*(idxB==idxC))+
...
                    (inputS11-inputS12-
(inputS44/2.0))*(inputGTensor(idxA,idxB,idxC,idxD));
                end
            end
        end
    end
end
```

```
function retStiffness = genStiffnessTensor(inputC11, inputC12,
inputC44, inputGTensor)
```

```
% This check takes more time than the actual calculation.
%if(~isequal(size(inputGTensor),[3,3,3,3]))
%    error('inputGTensor is of incorrect rank');
%end

% Compute tensor from definition...
retStiffness = zeros(3,3,3,3);
for idxA=1:3
    for idxB=idxA:3
        for idxC=1:3
            for idxD=idxC:3
                % From Page 138 of MSD Book.
                retStiffness(idxA,idxB,idxC,idxD) =
inputC12*(idxA==idxB)*(idxC==idxD) + ...

(inputC44)*((idxA==idxC)*(idxB==idxD)+(idxA==idxD)*(idxB==idxC))+ ...
                    (inputC11-inputC12-
(2.0*inputC44))*(inputGTensor(idxA,idxB,idxC,idxD));
                end
            end
        end
    end
end
```

```

function retOutputAngleFreq = genFrequencyCount(inputEulerAngles)

cAngles = size(inputEulerAngles,1);
inputEulerAngles =
sortrows(uint16(mod(round(rad2deg(inputEulerAngles)),359)));
retOutputAngleFreq = unique(inputEulerAngles,'rows');

% Add Frequency Count to the end...
retOutputAngleFreq(:,4) = uint16(zeros(size(retOutputAngleFreq,1),1));

% Count Frequencies.
idxBin = 1;
for idxAngle=1:cAngles

    % Increment until we get the correct bin. Valid since both
    sequences are sorted.

    while(~isequal(inputEulerAngles(idxAngle,:),retOutputAngleFreq(idxBin,1
:3)))
        idxBin = idxBin + 1;
    end

    % Increment bin count...
    retOutputAngleFreq(idxBin,4) = retOutputAngleFreq(idxBin,4) + 1;
end

if idxBin ~= size(retOutputAngleFreq,1)
    error('Loop Invariant Violated, idxBin=%d and expected %d.',
idxBin, retOutputAngleFreq);
end

function retFilteredFTerms =
genFilteredFTerms(inputEulerAngles,inputSuperSet)
global g_mfpFilteredFTerms;

if(size(inputSuperSet,2) ~= 3)
    error('inputSuperSet must have three columns');
end

% Bin Euler Angles into degree frequency bins...
frequencies = zeros(360,360,360);
inputEulerAngles =1+mod(round(rad2deg(inputEulerAngles)),359);
for idxAngle=1:size(inputEulerAngles, 1)
    frequencies(inputEulerAngles(idxAngle,1), ...
        inputEulerAngles(idxAngle,2), ...
        inputEulerAngles(idxAngle,3)) = ...
        frequencies(inputEulerAngles(idxAngle,1), ...
            inputEulerAngles(idxAngle,2), ...
            inputEulerAngles(idxAngle,3)) + 1;
end

```



```

% Transform...
tempTransform = fftn(frequencys);

% Construct ATerms that corrispond to Filtered Angle Set.
retFilteredFTerms = zeros(size(inputSuperSet,1),1);
for idxAterm=1:size(inputSuperSet,1)
    retFilteredFTerms(idxAterm) =
tempTransform(inputSuperSet(idxAterm,1), ...
                inputSuperSet(idxAterm,2), ...
                inputSuperSet(idxAterm,3));
end

function retMat = flattenTensor(inputTensor)

% This check takes more time than the actual calculation.
%if(~isequal(size(inputTensor),[3,3,3,3]))
%    error('inputGTensor is of incorrect rank');
%end

% Page 79 of MSD Book.
indexMapping = [1 1; 2 2; 3 3; 2 3; 1 3; 1 2];
indexMapping = round(indexMapping);

%
retMat = zeros(6,6);
cMaps = size(indexMapping,1);
for idxRow=1:6
    for idxCol=idxRow:6
        % Page 78 of MSD Book.
        retMat(idxRow,idxCol) =
inputTensor(indexMapping(idxRow,1),indexMapping(idxRow,2),indexMapping(
idxCol,1),indexMapping(idxCol,2));
        retMat(idxCol,idxRow) =
inputTensor(indexMapping(idxRow,1),indexMapping(idxRow,2),indexMapping(
idxCol,1),indexMapping(idxCol,2));
    end
end
end

```

Vita

Name: Marko Knezevic

Birth: Drvar, Bosnia and Herzegovina, November, 12th, 1980.

Education:

- Ph.D in Materials Science and Engineering, Drexel University, Philadelphia, PA
- BS/MS in Mechanical Engineering, University of Novi Sad, Serbia

Honors:

- Graduate Student Excellence in Research Award (May, 2008)
- Graduate Student Excellence in Teaching Award (May, 2008)
- Dragomir Nicolitch Charitable Trust Scholarship (October, 2007)
- George Hill, Jr. Fellowship (December, 2007)

Refereed Journal Publications:

1. M. Knezevic, J. Shaffer, and S.R. Kalidindi, "Building texture evolution networks for deformation processing of polycrystalline FCC metals using spectral approaches: Applications to process design for targeted performance", (submitted).
2. M. Knezevic, A. Levinson, R. Harris, R.K. Mishra, R. D. Doherty, and S.R. Kalidindi, "Anisotropic stress-strain response and microstructure evolution in AZ31", (submitted).
3. S.R. Kalidindi, M. Knezevic, S. Niezgoda, and J. Shaffer, "Representation of orientation distribution function and computation of first-order elastic bounds using fast Fourier transforms", *Acta Materialia*, (in press).
4. B.S. Fromm, B.L. Adams, S. Ahmadi, and M. Knezevic, "Grain size and orientation distributions: Application to yielding of alpha-titanium", *Acta Materialia*, 57, 8, May 2009, 2339-2348.
5. M. Knezevic, S.R. Kalidindi, and H.F. Al-Harbi, "Crystal plasticity simulations using discrete Fourier transforms", *Acta Materialia*, 57, 6, April 2009, 1777-1784.
6. M. Knezevic, S.R. Kalidindi, and D. Fullwood, "Computationally efficient database and spectral interpolation for fully plastic Taylor-type crystal plasticity calculations of face-centered cubic polycrystals", *International Journal of Plasticity*, 24, 7, 2008, 1264-1276.
7. M. Knezevic, S. R. Kalidindi and R.K. Mishra, "Delineation of first-order closures for plastic properties requiring explicit consideration of strain hardening and crystallographic texture evolution", *International Journal of Plasticity*, 24, 2, February 2008, 327-342.
8. T. Fast, M. Knezevic and S.R. Kalidindi, "Application of Microstructure Sensitive Design to Structural Components Produced from Hexagonal Polycrystalline Metals", *Computational Materials Science*, 43, 2, August 2008, 374-38.
9. H. K. Duvvuru, M. Knezevic, R.K. Mishra and S.R. Kalidindi, "Application of Microstructure Sensitive Design to FCC Polycrystals", *Materials Science Forum*, Vols. 546-549 (2007) pp. 675-680.
10. M. Knezevic and S.R. Kalidindi, "Fast Computation of First-Order Elastic-Plastic Closures For polycrystalline Cubic-Orthorhombic Microstructures," *Computational Materials Science*, 39, 3, May 2007, 643-648.
11. X. Wu, G. Proust, M. Knezevic and S.R. Kalidindi, "Elastic-plastic property closures for hexagonal close-packed polycrystalline metals using first-order bounding theories", *Acta Materialia*, 55, 8, May 2007, 2729-2737.
12. S.R. Kalidindi, H.K. Duvvuru and M. Knezevic, "Spectral Calibration of Crystal Plasticity Models", *Acta Materialia*, 54, 7, April 2006, 1795-1804.

